Influence of moisture on the resistivity of selected South African fly ashes

JA Ribberink

orcid.org/0000-0002-6695-235X

Dissertation submitted in fulfilment of the requirements for the degree *Master of Engineering in Chemical Engineering* at the North-West University

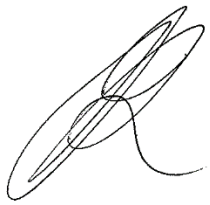
Supervisor:	Prof HWJP Neomagus
Co-Supervisor:	Dr DJ Branken
Co-Supervisor:	Prof RC Everson

Graduation ceremony: May 2019

Student number: 22798854

Declaration

I, JA Ribberink, declare herewith that the dissertation entitled: *Influence of moisture on the resistivity of selected South African fly ashes*, which I herewith submit to the North-West University is in compliance with the requirements set for the degree: Magister in Engineering (M. Eng) is my own work, has been text-edited in accordance with the requirements and has not already been submitted to any other university.



JA Ribberink

22798854

Signed on the 19th day of November of 2018

Abstract

The coals fired in the pulverised fuel boilers of South African power stations are generally of poor quality, producing numerous emissions, of which particulate matter has the largest impact in South Africa. Recently, the government of South Africa introduced a new Air Quality Management Act, in order to regulate the amount of emissions from pulverised fuel operations. Amongst other, the emission level of particulate matter is addressed.

The majority of coal power station in South Africa utilise electrostatic precipitators for the control of fly ash, with fly ash resistivity being an important factor strongly influencing ESP performance. The resistivity of fly ash is influenced by a number of factors; including the chemical composition of the ash and adsorption of physical or chemical species on the surface of the ash particle. The resistivity can be subdivided into two distinct areas, which are the surface resistivity and volume resistivity region. Generally, where ambient moisture is present, electron transfer occurs via the surface of the ash particle at lower temperatures, while at higher temperatures the electron transfer occurs more predominantly via the bulk of the ash particle. In this study, the resistivity of three typical South African coal ashes, collected from operational power stations, is determined at various ambient moisture levels. For this purpose, a resistivity oven, equipped with local climate control, was used. The observed results were compared to a general predictive model that was developed by Roy Bickelhaupt in the 1970s specifically for Northern American coal ashes.

The three South African fly ash samples were sourced and the resistivity determined at 0, 4.6, 6.0 and 9.0 vol% moisture, to assess the influence of ambient moisture on the resistivity. Dry ash resistivity showed a linear relation between the log of resistivity and temperature in the volume resistivity region which agreed with literature. When moisture was introduced, the samples showed a reduction in resistivity below temperatures of 200°C. The reduction in resistivity, in the surface resistivity region, is due to the moisture forming a thin conducting layer along the surface of the particle, accelerating electron transfer. An increase in the moisture content resulted in a further reduction in resistivity in the surface resistivity region. At 150°C and 9.0 vol% ambient moisture the resistivity of the ash samples showed a reduction of 89 to 95% when compared to dry resistivities.

The elemental composition of the sampled ashes was also used, along with the standard Bickelhaupt predictive model to determine the theoretical resistivity values. The standard Bickelhaupt model showed deviations of several orders between the experimental values and theoretical values, with the model overestimating the resistivity. The overestimation was

attributed to the different nature of the American coal ashes when compared to South African ashes. The deviation is most significantly related to the sodium content, which is substantially higher in American coal ashes. For this reason, modifications were proposed to the volume and surface resistivity term of the Bickelhaupt model to better account for the unique chemistry of South African ashes. These modifications improved the predictive accuracy of the model significantly and deviations smaller than a factor of 2.5, a ratio commonly considered acceptable for between-laboratory repeatability by the Institute of Electrical and Electronics Engineering, were obtained. These modified relations can in future be used for more effective ESP design and operation, in the case where South African coals are used for power generation.

Keywords: Resistivity, Fly Ash, Moisture, Ash Composition, Resistivity Oven, Bickelhaupt Correlation

ACKNOWLEDGEMENTS

Firstly, I would like to thank EPPEI for the opportunity to complete this study. Without their financial support this dissertation would not have been possible.

I would like to thank Prof Hein Neomagus for his continued support and guidance during this dissertation. Thank you for the patience shown and the many hours spent teaching me. I would also like to thank Prof Ray Everson and Dr Dawie Braken for their continued technical guidance during this study.

I would also like to thank Ted Paarlberg, Adrian Brock and Jan Kroeze for their continued support and technical expertise, modifying and maintaining the equipment used in this study.

Lastly, I would like to thank my parents, friends and loved ones who supported and inspired me. Without their insight and encouragement this study would not have been possible.

Table of Contents

Declaration ii

Abstract iii

ACKNOWLEDGEMENTS v

Abbreviations xvi

Symbols xviii

1. Introduction 1

1.1. Particulate Matter Control 2
1.2. Electrostatic Precipitators 3
1.3. Aim and Objectives 5
1.4. Scope 5

2. Literature Survey 6

2.1. Particulate Emission Control 6
2.2. Electrical Resistivity 8
2.3. Resistivity of Various Materials 9
2.3.1. Resistivity of Conductors 9
2.3.2. Resistivity of Semiconductors 11
2.3.3. Resistivity of Insulators 11
2.4. Temperature Dependency of Resistivity 12
2.5. Size Dependency of Resistivity 12
2.6. Fly Ash Resistivity 13
2.6.1. Volume Resistivity 15
2.6.2. Surface Resistivity 16
2.7. Experimental Determination of Resistivity 16
2.7.1. Two-Point Technique 16
2.7.2. Four-Point Technique 17
2.7.3. High Voltage Conductivity Cell 18
2.7.4. Parallel Plate and Radial Flow Cells 19
2.7.5. Resistivity Measurement Considerations 22
2.8. Coal Ash Resistivity Modelling 23
2.9. Fly Ash Composition 25
2.10. Resistivity of South African Fly Ashes 28

2.11. Flue Gas Conditioning 30
3. Sample Preparation and Analysis 32
3.1. Fly Ash Sampling 32
3.2. Sample Preparation 33
3.3. Ash Analysis & Characterization 34
3.3.1. Particle Size distribution 34
3.3.2. Proximate Analysis and Calorific Value 34
3.3.3. Elemental analysis 35
3.3.4. Mineralogical analysis 35
3.4. Results and Discussion 36
3.4.1. Particle Size distribution 36
3.4.2. Proximate Analysis and Calorific Value 37
3.4.3. Elemental analysis 38
3.4.4. Mineralogical analysis 42
3.5. Summary 44
4. Experimental Methodology 45
4.1. Experimental Rig 45
4.1.1. Oven & Environmental Chamber 46
4.1.2. Control Panel 49
4.1.3. Humidifiers 51
4.2. Experimental Procedure 53
4.2.1. Loading of Ash Bowls 53
4.2.2. Humidifier Start-up and Testing 55
4.2.3. Resistivity Measurement 55
4.3. Experimental 57
4.3.1. IEEE Round Trip Protocol - Ascending versus Descending Resistivity Results 58
4.3.2. Oven Commissioning and Calibration 59
4.3.2.1. Cross-bowl Repeatability 60
4.3.2.2. Within-laboratory Repeatability 61
4.3.2.3. Between-laboratory Repeatability 62
4.3.2.4. Critical evaluation of Commissioning 63
5. Results and Discussion 65
5.1. Resistivity Measurement 65
5.1.1. Resistivity Results for Dry Ambient Conditions 65

5.1.2. Resistivity Results for Humidified Ambient Conditions 66
5.2. Comparison with the Bickelhaupt Model 69
5.3. Bickelhaupt Correction 72
5.3.1. Modelling Approach 72
5.3.2. Volume Corrected Bickelhaupt Correlation 73
5.3.3. Surface Corrected Bickelhaupt Correlation 76
5.3.4. Corrected Bickelhaupt Model at Various Moisture Levels 78
6. Conclusion and Recommendations 81
7. References 83
A. Appendix A: Particle Size Distribution for PS A, PS B and PS C 89
B. Appendix B: Instrument Details and Settings 92
C. Appendix C: Proximate Analysis and Calorific Values 94
D. Appendix D: XRF Results 95
E. Appendix E: XRD Results 97
F. Appendix F: QEMSCAN Results 98
G. Appendix G: Comparison of Elemental and Mineralogical Results 103
H. Appendix H: Bickelhaupt Correlation 104
a. Adapting Input Data 104
b. Calculate Volume Resistivity, ρ_v 105
c. Calculate Surface Resistivity, ρ_s 106
d. Calculate Combined Resistivity, ρ_{vs} 108
I. Appendix I: Modified Bickelhaupt Model 109
J. Appendix J: Resistivity Curves and Error Ratios 112
a. Experimental Resistivity Data 112
i. Resistivity Data at Dry Ambient Conditions 112
ii. Resistivity Data at 4.6 vol% Ambient Moisture 113
iii. Resistivity Data at 6.0 vol% Ambient Moisture 114
iv. Resistivity Data at 9.0 vol% Ambient Moisture 115
b. Standard Bickelhaupt Model 118
i. Resistivity Data at Dry Ambient Conditions 118
ii. Resistivity Data at 4.6 vol% Ambient Moisture 119
iii. Resistivity Data at 6.0 vol% Ambient Moisture 120

iv. **Resistivity Data at 9.0 vol % Ambient Moisture** 121
c. **Volume Corrected Bickelhaupt Model** 122
i. **Resistivity Data at Dry Ambient Conditions** 123
ii. **Resistivity Data at 4.6 vol % Ambient Moisture** 124
iii. **Resistivity Data at 6.0 vol % Ambient Moisture** 125
iv. **Resistivity Data at 9.0 vol % Ambient Moisture** 126
d. **Surface and Volume Corrected Bickelhaupt Model** 127
i. **Resistivity Data at 4.6 vol % Ambient Moisture** 128
ii. **Resistivity Data at 6.0 vol % Ambient Moisture** 129
iii. **Resistivity Data at 9.0 vol % Ambient Moisture** 131

List of Figures

Figure 1-1: 2016 OECD global energy supply by fuel (Taken from: IEA, 2016) 1
Figure 1-2: Typical coal ash resistivity as a function of temperature and ambient moisture content (Taken from: IEEE Standard 548, 1984) 4
Figure 2-1: General arrangement of an electrostatic precipitator (Taken from: Soud & Mitchell, 1997) 7
Figure 2-2: Free electrons moving throughout the lattice (Taken from: Heaney, 1999). 9
Figure 2-3: Band-gap pattern of a conductor (a), semiconductor (b) and insulator (c) (Adapted from: Haliday et al., 1970) 10
Figure 2-4: Typical graph of the log of resistivity as a function of temperature (Taken from Bickelhaupt, 1979) 15
Figure 2-5: Configuration of two-point method (Taken from: Heaney, 1999) 17
Figure 2-6: Configuration of four-point method (Taken from: Heaney, 1999) 18
Figure 2-7: High voltage conductivity cell (Taken from: White, 1953) 19
Figure 2-8: General apparatus arrangement for IEEE compliant resistivity oven (Taken from: IEEE std. 548, 1984) 20
Figure 2-9: ANSI/ASME PTC 28-1965 guarded, parallel plate test cell (Taken from: IEEE std. 548, 1984) 21
Figure 2-10: Combination parallel plate- radial flow resistivity test cell (Taken from: Bickelhaupt, 1978) 22
Figure 2-11: Effect of chemical composition (Na, Ca, Fe, K, Mg and SO_3) on fly ash resistivity (Taken from: Chandra et al., 2006) 24
Figure 2-12: Corrected fly ash correlation curve as a function of temperature (Adapted from: Van Wyk, 2015) 25
Figure 2-13: Comparison between ascending, descending and washed resistivity as a function of temperature (Taken from: White, 1953) 26
Figure 2-14: Ash Resistivity as a function of temperature for various ambient moisture contents (Taken from: Chauke, 2013) 28
Figure 2-15: Resistivity as a function of temperature with 10 ppm SO_3 (Adapted from: Van Wyk, 2015) 29
Figure 3-1: Fly ash sampling sites 32
Figure 3-2: Sample preparation and sample size for various analyses 34
Figure 3-3: Fly ash particle size distribution 36
Figure 3-4: Comparison with previously sampled ash for PS A (a), PS B (b) and PS C (c) (Adapted from: Bosch, 1993, Bosch, 1995) 37
Figure 4-1: Oven and environmental chamber 46
Figure 4-2: Environmental chamber inlet, outlet and connectors 47

Figure 4-3: Ash bowls and electrode configuration **48**
Figure 4-4: Resistivity oven wiring diagram **49**
Figure 4-5: Resistivity oven control panel **50**
Figure 4-6: Flow sampling valve and nitrogen shut-off valve **51**
Figure 4-7: Humidifier system **52**
Figure 4-8: Humidifier sampling port **53**
Figure 4-9: Fly Ash temperature as a function of oven temperature **54**
Figure 4-10: PS A ascending and descending resistivity as a function of temperature at dry ambient conditions **59**
Figure 4-11: Commissioning - Phase 1 – cross-bowl repeatability at dry ambient conditions ... **60**
Figure 4-12: Commissioning Phase 2 – within-laboratory repeatability at 5.9 vol% ambient moisture for PS X (a), PS Y (b) and PS Z (c) **61**
Figure 4-13: Commissioning Phase 3 – Between-laboratory repeatability for PS X (a), PS Y (b) and PS Z (c) **63**
Figure 4-14: PS Z resistivity comparison with SRI resistivity for the ascending and descending stages **64**
Figure 5-1: Resistivity as a function of temperature for dry ambient conditions **66**
Figure 5-2: Resistivity as a function of temperature and ambient moisture for PS A (a), PS B (b) and PS C (c) **67**
Figure 5-3: Resistivity as a function of temperature at an ambient moisture content of 9.0 vol% **68**
Figure 5-4: Experimental and Bickelhaupt resistivity as a function of temperature and ambient moisture for PS A (a), PS B (b) and PS C (c) **70**
Figure 5-5: Experimental, Bickelhaupt and volume corrected Bickelhaupt resistivity as a function of temperature at dry ambient conditions for PS A (a), PS B (b) and PS C (c) **73**
Figure 5-6: Experimental, Bickelhaupt and volume corrected Bickelhaupt resistivity at 9.0 vol% moisture for PS A (a), PS B (b) and PS C (c) **75**
Figure 5-7: Experimental, Bickelhaupt, surface and volume corrected Bickelhaupt resistivity as a function of temperature at 9.0 vol% ambient moisture for PS A (a), PS B (b) and PS C (c) **77**
Figure 5-8: Experimental and corrected Bickelhaupt model resistivity as a function of temperature at 4.6, 6.0 and 9.0 vol% ambient moisture for PS A (a), PS B (b) and PS C (c) **79**
Figure F-1: Mineralogical QEMSCAN results of ash sample PS A **98**
Figure F-2: Mineralogical QEMSCAN results of ash sample PS B **98**
Figure F-3: Mineralogical QEMSCAN results of ash sample PS C **99**
Figure H-1: Resistivity as a function of Li + Na concentration at 84°C (Taken from: Bickelhaupt, 1979) **106**
Figure H-2: Resistivity as a function of Li + Na concentration at 112°C (Taken from: Bickelhaupt, 1979) **106**

Figure J-1: Ascending resistivity as a function of temperature for PS A, B & C at dry ambient conditions 112
Figure J-2: Descending resistivity as a function of temperature for PS A, B & C at dry ambient conditions 112
Figure J-3: Ascending resistivity as a function of temperature for PS A, B & C at 4.6 vol% ambient moisture. 113
Figure J-4: Descending resistivity as a function of temperature for PS A, B & C at 4.6 vol% ambient moisture. 113
Figure J-5: Ascending resistivity as a function of temperature for PS A, B & C at 6.0 vol% ambient moisture. 114
Figure J-6: Descending resistivity as a function of temperature for PS A, B & C at 6.0 vol% ambient moisture. 114
Figure J-7: Ascending resistivity as a function of temperature for PS A, B & C at 9.0 vol% ambient moisture. 115
Figure J-8: Descending resistivity as a function of temperature for PS A, B & C at 9.0 vol% ambient moisture. 115
Figure J-9: Standard Bickelhaupt model resistivity as a function of temperature for PS A, B & C at dry ambient conditions 118
Figure J-10: Standard Bickelhaupt model resistivity as a function of temperature for PS A, B & C at 4.6 vol% ambient moisture 119
Figure J-11: Standard Bickelhaupt model resistivity as a function of temperature for PS A, B & C at 6.0 vol% ambient moisture 120
Figure J-12: Standard Bickelhaupt model resistivity as a function of temperature for PS A, B & C at 9.0 vol% ambient moisture 121
Figure J-13: Volume corrected Bickelhaupt model resistivity as a function of temperature for PS A, B & C at dry ambient conditions 123
Figure J-14: Volume corrected Bickelhaupt model resistivity as a function of temperature for PS A, B & C at 4.6 vol% ambient moisture 124
Figure J-15: Volume corrected Bickelhaupt model resistivity as a function of temperature for PS A, B & C at 6.0 vol% ambient moisture 125
Figure J-16: Volume corrected Bickelhaupt model resistivity as a function of temperature for PS A, B & C at 9.0 vol% ambient moisture 126
Figure J-17: Surface and volume corrected Bickelhaupt model resistivity as a function of temperature for PS A, B & C at 4.6 vol% ambient moisture 128
Figure J-18: Surface and volume corrected Bickelhaupt model resistivity as a function of temperature for PS A, B & C at 6.0 vol% ambient moisture 129
Figure J-19: Surface and volume corrected Bickelhaupt model resistivity as a function of temperature for PS A, B & C at 9.0 vol% ambient moisture 131

List of Tables

Table 2-1: Industrial ESP performance as a function of fly ash classification and resistivity (Taken from: Chandra, 2013) **14**
Table 2-2: Effect of coal ash composition on resistivity (Taken from: Chandra, 2013) **27**
Table 3-1: Fly ash sampling sites **33**
Table 3-2: Standard methods for proximate and calorific analysis **35**
Table 3-3: 10%, 50% and 90% intercepts for the cumulative mass of ash samples PS A, B and C **36**
Table 3-4: Proximate analysis and calorific values of fly ash samples PS A, PS B and PS C (wt%) **38**
Table 3-5: Normalized XRF results of coal ash samples on a LOI-free Basis (wt%) **38**
Table 3-6: Major elements comparison of coal ash samples (wt%) **39**
Table 3-7: Minor elements comparison of coal ash samples (wt%) **40**
Table 3-8: Comparison of averaged XRF result based on ash origin (wt%) **41**
Table 3-9: Normalised XRD results of coal ash samples with amorphous content **42**
Table 3-10: QEMSCAN analysis (vol%) **43**
Table 4-1: Moisture content of flue gas by volume for April 2013 to March 2014 at 6% O_2 ..... **57**
Table 4-2: Cross-bowl error ratio (Relative to Bowl #1) **61**
Table 4-3: Within-laboratory error ratio **62**
Table 5-1: Percentage resistivity reduction relative to dry ambient conditions at 150°C (vol%) **68**
Table 5-2: Error ratios of standard Bickelhaupt model at 120°C, 270°C and averaged for dry, 4.6, 6.0 and 9.0 vol% ambient moisture **71**
Table 5-3: Volume corrected Bickelhaupt constants **74**
Table 5-4: Error ratio of volume corrected Bickelhaupt model at 120, 270°C and averaged for dry ambient conditions **74**
Table 5-5: Error Ratio of volume corrected Bickelhaupt model at 120, 270°C and averaged for 4.6, 6.0 and 9.0 vol% ambient moisture **76**
Table 5-6: Surface corrected Bickelhaupt constants **77**
Table 5-7: Error ratio of corrected Bickelhaupt model at 120, 270°C and averaged at 9.0 vol% ambient moisture **78**
Table 5-8: Error ratio of corrected Bickelhaupt model at 120, 270°C and averaged for 4.6, 6.0 vol% ambient moisture **80**
Table B-1: Malvern Mastersizer instrument settings **92**
Table B-2: XRD instrument settings **92**
Table B-3: QEMSCAN instrument settings **93**
Table D-1: Elemental ash composition (wt%) **96**

Table D-2: Historical Eskom XRF results (wt%) (Taken from: Bosch, 1993, Bosch, 1995) 96
Table E-1: X-Ray Diffraction analysis (wt%) 97
Table F-1: Mineralogical QEMSCAN volume proportions (vol%) 100
Table F-2: Mineral densities (kg/m^3) 101
Table F-3: Mineralogical QEMSCAN weight proportions (wt%) 102
Table G-1: Comparison between XRF, XRD & QEMSCAN (wt%) 103
Table H-1: Atomic concentration of cations (wt%) 105
Table I-1: Modified values to improve volume resistivity term of the Bickelhaupt model 109
Table I-2: Modified values to improve surface resistivity term of the Bickelhaupt model 110
Table J-1: Experimental resistivity data at dry ambient conditions 113
Table J-2: Experimental resistivity data at 4.6 vol% ambient moisture 114
Table J-3: Experimental resistivity data at 6.0 vol% ambient moisture 115
Table J-4: Experimental resistivity data at 9.0 vol% ambient moisture 116
Table J-5: Percentage reduction relative to dry ambient conditions 117
Table J-6: Standard Bickelhaupt resistivity data at dry ambient conditions 118
Table J-7: Resistivity error ratio for standard Bickelhaupt model at dry ambient conditions 119
Table J-8: Standard Bickelhaupt resistivity data at 4.6 vol% ambient moisture 120
Table J-9: Resistivity error ratio for standard Bickelhaupt model at 4.6 vol% ambient moisture 120
Table J-10: Standard Bickelhaupt resistivity data at 6.0 vol% ambient moisture 121
Table J-11: Resistivity error ratio for standard Bickelhaupt model at 6.0 vol% ambient moisture 121
Table J-12: Standard Bickelhaupt resistivity data at 9.0 vol% ambient moisture 122
Table J-13: Resistivity error ratio for standard Bickelhaupt model at 9.0 vol% ambient moisture 122
Table J-14: Volume corrected Bickelhaupt resistivity data at dry ambient conditions 123
Table J-15: Resistivity error ratio for volume corrected Bickelhaupt model at dry ambient conditions 124
Table J-16: Volume corrected Bickelhaupt resistivity data at 4.6 vol% ambient moisture 125
Table J-17: Resistivity error ratio for volume corrected Bickelhaupt model at 4.6 vol% ambient moisture 125
Table J-18: Volume corrected Bickelhaupt resistivity data at 6.0 vol% ambient moisture 126
Table J-19: Resistivity error ratio for volume corrected Bickelhaupt model at 6.0 vol% ambient moisture 126
Table J-20: Volume corrected Bickelhaupt resistivity data at 9.0 vol% ambient moisture 127
Table J-21: Resistivity error ratio for volume corrected Bickelhaupt model at 9.0 vol% ambient moisture 127

Table J-22: Surface and volume corrected Bickelhaupt resistivity data at 4.6 vol% ambient moisture 128
Table J-23: Resistivity error ratio for surface and volume corrected Bickelhaupt model at 4.6 vol% ambient moisture 129
Table J-24: Surface and volume corrected Bickelhaupt resistivity data at 6.0 vol% ambient moisture 130
Table J-25: Resistivity error ratio for surface and volume corrected Bickelhaupt model at 6.0 vol% ambient moisture 130
Table J-26: Surface and volume corrected Bickelhaupt resistivity data at 9.0 vol% ambient moisture 131
Table J-27: Resistivity error ratio for surface and volume corrected Bickelhaupt model at 9.0 vol% ambient moisture 132

Abbreviations

ANSI	American National Standards Institute
ASME	American Society of Mechanical Engineers
CC	Closed Corporation
EPPEI	Eskom Power Plant Engineering Institute
ESP	Electrostatic Precipitator
FFP	Fabric Filter Plant
FGC	Flue gas conditioning
HGV	Heavy Goods Vehicle
IEEE	Institute of Electrical and Electronics Engineering
ISO	International Organization for Standardization
LNB	Low NOx Burners
LOI	Loss of Ignition
LTA	Low Temperature Ashing
NOx	Nitrogen Oxides
OECD	Organization for Economic Cooperation and Development
PF	Pulverised Fuel
PJFFP	Pulse Jet Fabric Filter Plant
PM	Particulate Matter
PS	Power Station
PSD	Particle Size Distribution
PVC	Polyvinyl Chloride
QEMSCAN	Quantitative Evaluation of Materials by Scanning Electron Microscopy
RT&D	Research, Testing and Development

SI	Système Internationale
SRI	Southern Research Institute
STP	Standard Temperature and Pressure
XRD	X-Ray Diffraction
XRF	X-Ray Florescence

Symbols

A	Cross-sectional area (m^2)
A_s	Surface corrected Bickelhaupt constant A
A_v	Volume corrected Bickelhaupt constant A
B_s	Surface corrected Bickelhaupt constant A
B_v	Volume corrected Bickelhaupt constant B
C_B	Baseline moisture content (9 vol%)
C_v	Volume corrected Bickelhaupt constant C
C_W	Percentage moisture by volume to which ρ_s is adjusted
D_v	Volume corrected Bickelhaupt constant D
e	Electric charge of the electron
E	Field strength to which ρ_E is to be adjusted
E_B	Baseline field strength (kV/cm)
E_g	Energy difference (eV)
E_v	Volume corrected Bickelhaupt constant E
I	Current (A)
k	Boltzmann Constant (eV/K)
K_0	Physical and chemical parameters related to moisture content (1/vol%)
K_1	Physical and chemical parameters related to moisture content (K)
L	Length (m)
l'	Distance between the two voltage measuring wires (m)
m	Mass of an electron (g)
n	Number of electrons carrying current in a conductor
R	Resistance (Ω)

S_e	$\Delta \log \rho / \Delta E$ (-0.030)
S_W	$\Delta \log \rho_s / \Delta H_2O\%$ (-0.0808)
T	Absolute Temperature (K)
V	Potential Difference (V)
W	Moisture Concentration (vol%)
x	Atomic Concentration of Li + Na
y	Atomic Concentration of Fe
z	Atomic Concentration of Mg + Ca
α	Temperature coefficient of resistivity
θ	Experimental Activation Energy, (eV)
ρ	Resistivity (Ω cm)
ρ_B	Resistivity at baseline field strength (Ω cm)
ρ_E	resistivity adjusted to field strength E (Ω cm)
ρ_s	Resistivity adjusted to moisture concentration C_W (Ω cm)
ρ_{s0}	Maximum Surface Resistivity (Ω cm)
ρ_{sB}	Resistivity at baseline moisture concentration (Ω cm)
τ	Mean free time between collisions (s)

1. Introduction

With the advent of the industrial revolution in the late 1700s and early 1800s, the demand for energy has increased, leading to ever more efficient and innovative ideas on how to generate this valuable commodity. The vast majority of the global energy demand is still being supplied by fossil fuels, as illustrated in Figure 1-1.

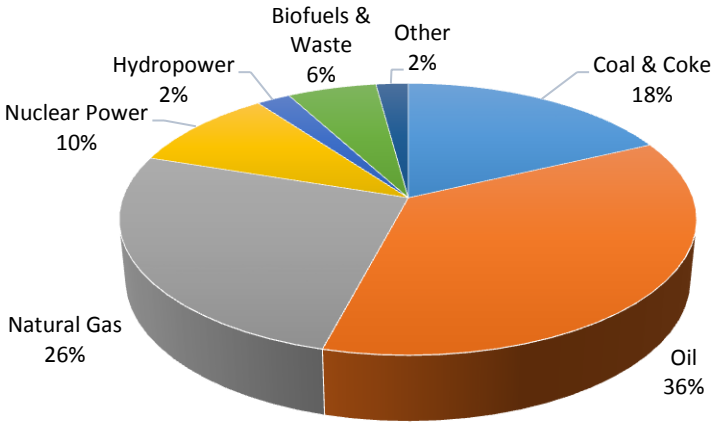


Figure 1-1: 2016 OECD global energy supply by fuel (Taken from: IEA, 2016)

In South Africa, coal is currently still considered the primary fuel source, with up to 76% of the country's primary energy being supplied by coal. With South Africa's coal reserves estimated at 53 billion tones and suitable alternatives lacking, the main energy source in South Africa will not significantly change in the near future (Eskom Holdings, 2015).

Eskom is a state owned utility supplier generating approximately 93% of the country's electricity, also supplying electricity to large parts of the African continent (Eskom Holdings, 2017). With the demand for electricity growing in South Africa, Eskom approved the construction of two of the world's largest coal fired power stations, Medupi and Kusile. These two new power stations, along with other initiatives, will raise the total installed capacity of the utility by 17 GW by 2020 (Eskom Holdings, 2014b). While the commissioning of these two new power stations will lead to a more stable power grid, it will also increase emission levels in South Africa. Both Medupi and Kusile are of super-critical design and equipped with fabric filter plants (FFP) and low NOx burners (LNB). Kusile will be equipped

with a wet flue gas desulphurisation plant while Medupi will be retrofitted with desulphurisation capabilities at a later stage (Eskom Holdings, 2014b).

These two new power stations will feature new and innovative emission reduction technologies to ensure compliance with the National Environmental Management: Air Quality Act 39 of 2004. However, the remainder of the power stations in the Eskom fleet were constructed prior to the Air Quality Management Act and designed according to the emission legislation of that time. Some of these older power stations currently do not comply with the new Air Quality Act and modifying these power stations to adhere to the new legislation is expected to be a multi-billion Rand undertaking (Eskom Holdings, 2014a).

When coal is fired in a pulverised fuel (PF) boiler, initially, volatile matter and char is formed. When these components combust, energy is released and several other components are generated, including gaseous and solid pollutants. The remaining solid matter after combustion is called ash (Williams *et al*, 2000), which is an inert material that cannot be combusted and consists of a number of minerals. For the most part, South African coal is considered of a poor quality, with the ash mineral content of coal ranging from 18 to 42 wt% in extreme cases (Bosch, 1993, Chauke & Gouws, 2013, Hancox & Götz, 2014).

The Air Quality Management Act states that the particulate matter emissions had to be reduced to 100 mg/Nm^3 by 2015, calling for a further reduction to 50 mg/Nm^3 by 2020. Eskom has since applied for postponement in complying with the emission limits and has set an emission reduction plan in place to implement innovative emission reduction technologies on the power stations which currently do not comply. The new legislation calls for particulate matter reductions of up to 200 mg/Nm^3 by 2020 on some of the power stations currently using electrostatic precipitators (Patel & Swart, 2014).

1.1. Particulate Matter Control

There are numerous technologies available for the control of particulate emissions, however, the two most widely used technologies are electrostatic precipitators (ESPs) and fabric filter plants (FFPs) (Speight, 2013, Soud & Mitchell, 1997). An electrostatic precipitator consists of a discharge electrode, collection electrode or plate and a precipitator shell. The particulate matter entering the precipitator shell is charged by a corona field, which is generated by discharge electrodes. The charged particles migrate to the collection electrode due to the interaction between the electric field and the charged particles. The particles accumulate on the collection electrode and are dislodged via rapping or vibration (Speight,

2013). ESPs have the ability to achieve collection efficiency in excess of 99.5%; while fabric filter plants can achieve collection efficiencies as high as 99.9% (Klinkspor & Vernon, 1988). FFPs work by passing the particle-laden gas through a fabric filter. Particles are retained in the filter bag while the gas is allowed to pass through. The particles accumulated in the filter bag are periodically dislodged by use of a shaker, backwash air, or a pulse jet (Speight, 2013).

When comparing the collection efficiencies of both electrostatic precipitators and fabric filter plants, FFPs have proven to be more efficient at collecting fly ash (Speight, 2013). Electrostatic precipitators are considered a more cost effective technology when firing medium- to high-sulphur coal whereas fabric filter plants become more cost effective when firing low-sulphur coal and coal generating high resistivity ash (Soud & Mitchell, 1997). The operational cost of both these technologies are similar, with ESPs requiring regular replacement of damaged discharge electrodes, whereas FFPs require fabric filter bag replacement on a regular basis (Bosch, 1993; Nalbandian, 2006).

1.2. Electrostatic Precipitators

South African coals are not well suited to ESP operation due to the low sulphur content and high resistivity of the fly ash (Van Wyk, 2016; White, 1953). In an effort to comply with the new legislation, Eskom will either attempt to retrofit the remaining ESP units with FFPs or upgrade the existing ESP units to improve their collection efficiency (Eskom Holdings, 2013). Retrofitting an ESP internals with a Pulse Jet Fabric Filter Plant (PJFFP) is a notoriously expensive endeavour, ranging from R750 - 1200/kWe, and requires long unit outages (Nalbandian, 2006). An alternative and more viable option might be to improve the efficiency of the existing PM control equipment.

ESP performance is generally affected by a number of factors such as the electrical conditions in the ESP, the particle size distribution of the fly ash, the flow distribution throughout the ESP unit, the effectiveness of the rapping operation, and the electrical resistivity of the fly ash (Soud & Mitchell, 1997; Bickelhaupt, 1975). Resistivity, normally expressed in Ω cm, is an intrinsic, physical material property denoting the ability of a material to oppose the flow of electrons, unlike resistance, which is dependent on the geometry of the conductor or insulator (Lowrie, 2010).

The resistivity of fly ash is influenced by a number of factors, such as the chemical and physical properties of the coal fed to the boiler, the method and parameters to which the coal

was pulverized before combustion and flue gas conditions (Xu *et al*. 2014; Jędrusik & Świerczok, 2009). Like most physical properties, resistivity also varies largely, with temperature as illustrated in Figure 1-2, where the resistivity of a single ash sample is given as a function of temperature and moisture content of the flue gas. From this figure, it can also be seen that the resistivity decreases with an increase in moisture content, at lower temperatures. The presence of moisture allows for the formation of a very thin moisture layer on the surface of the fly ash particles. This thin layer increases the surface conductivity, facilitating the transfer of electrons along the surface of the particles (Ray, 2004).

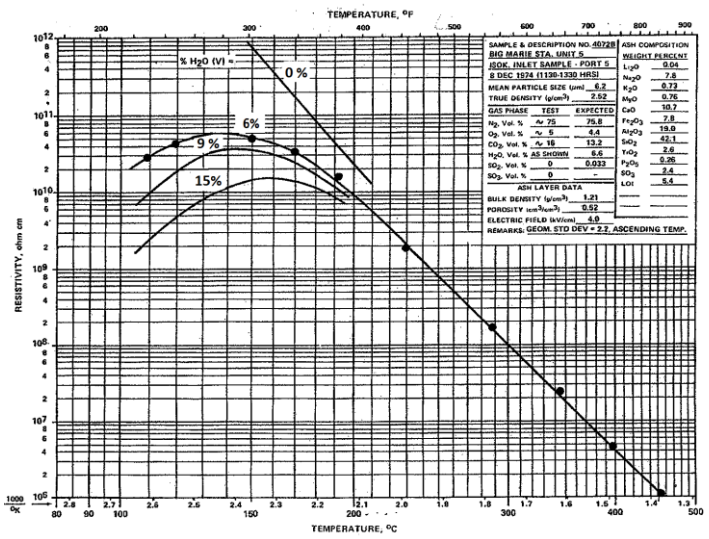


Figure 1-2: Typical coal ash resistivity as a function of temperature and ambient moisture content (Taken from: IEEE Standard 548, 1984)

In general, high resistivity ash causes poor ESP performance, since the ash particles are difficult to charge. The ash particles also do not easily lose their negative charge once they reach the collection plates, resulting in a tight barrier of fly ash on the plates. This, in turn, severely limits the collection efficiency of the ESP unit (Jaworek *et al*., 2004). With fly ash resistivity being such an important design and operational parameter, the effective prediction of this parameter is of importance for the design and retrofitment of ESP units. Fly ash resistivity can be acquired either by experimental procedure, as given in the IEEE standard 548 of 1984, or by predictive models such as those suggested by Bickelhaupt (1974, 1975 & 1979), McLean (1979) and others.

1.3. Aim and Objectives

Aim

This study will be conducted to assess the influence of the ambient moisture content on the resistivity of typical South African coal ashes and to evaluate and amend predictive ash resistivity models to describe this property.

Objectives

The following objectives are defined:

1. Source three representative fly ash samples from different power stations in South Africa, with historically varying ash collection efficiencies.
2. Characterise the elemental and mineralogical composition of the coal ashes.
3. Experimentally determine the coal ash resistivity as a function of temperature and ambient moisture levels.
4. Compare the experimental obtained values with models from published literature.
5. Amend these models to account for the unique nature of South African coal ashes.

1.4. Scope

The previously decommissioned resistivity oven, received from Eskom RT&D is recommissioned and fitted with humidification capabilities. In order to determine the accuracy of the recommissioned resistivity oven, coal ash samples previously analysed by the Southern Research Institute (SRI) in Birmingham, Alabama (USA) are also analysed in the new rig and the results compared. Once the resistivity oven is satisfactorily commissioned, testing can commence on the sampled ashes. The ashes are analysed dry and at various ambient moisture levels. Using the elemental composition of the fly ash as input, the determined resistivity will be compared to existing predictive models and the accuracy of the models discussed. The possibility of adding mineralogical data to the predictive model will be assessed and model modifications will be proposed to further improve the model for South African coal ashes.

2. Literature Survey

In this section relevant literature is presented and discussed. Firstly, a brief background of ESP operation and the importance of coal ash resistivity is given. For a better understanding of resistivity as a physical property, the quantum mechanical explanation of electron transfer in materials is considered. This understanding of electron transfer is then further analysed to divide material into subclasses depending on their respective electrons transfer mechanisms and resistance to electron flow. Additionally, the temperature and size dependency of resistivity is discussed. After this general assessment, specifics around resistivity phenomena in fly ash are presented. Also, electrical resistivity as an operating and design parameter of electrostatic precipitators is considered along with various methods of measuring fly ash resistivity. Specific emphasis was placed on the IEEE standard (Std. 548 of 1984) and relevant equipment used for laboratory fly ash resistivity quantification. The unique nature of South African fly ash is further discussed along with the influence of ash composition on resistivity. Lastly, the effect of flue gas conditioning, using chemicals such as sulphur trioxide, in relation to coal ash resistivity is reviewed.

2.1. Particulate Emission Control

The combustion of coal leads to numerous air pollutants including carbon dioxide, sulphur dioxide, nitrogen oxides, particulate matter and various other species (Speight, 2013). The specific emissions can be controlled by different technologies, where ESPs and FFPs are the most commonly used for particulate matter (PM). Historically, in South Africa, coal fired power stations were only equipped with PM control, with 67% of Eskom fleet being fitted with ESPs, and the remainder with FFPs (Patel & Swart, 2014). Electrostatic precipitators comprise of several basic components, of which the discharge electrodes, collection electrodes and precipitator shell are the most important. The working of an ESP occurs in two distinct operations.

The first operation entails the capturing of fly ash from the flue gas stream while the second deals with dislodging the collected ash particles from the collection plates (Soud & Mitchell, 1997). In the first operation, the particle laden flue gas, entering the ESP, encounters a strong electric field generated by a high-voltage direct-current rectifier. The electric field is strong enough to create a corona discharge around the discharge electrodes. The flue gas is ionized by the corona discharge, creating a large number of negative ions. These

negative ions migrate towards the positively charged collecting plates. While migrating, the ions come in contact, and adhere to, suspended ash particles in the gas stream and are attracted by the collection plates. The now negatively charged ash particles adhere to the collection plates and subsequently pass their charge to earth (Soud & Mitchell, 1997). For the negative charge to be passed to earth, the collected particles should possess at least a small degree of conductivity otherwise ESP performance declines (White, 1953).

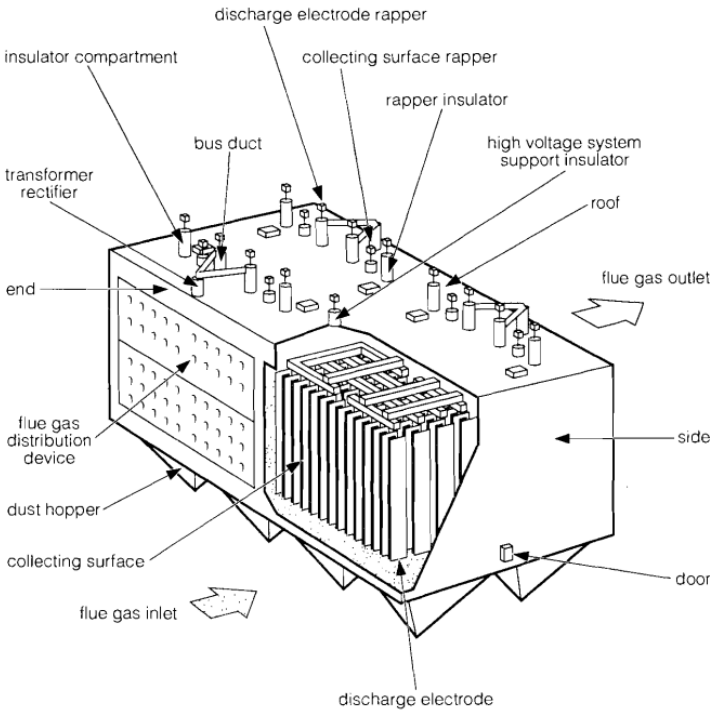


Figure 2-1: General arrangement of an electrostatic precipitator (Taken from: Soud & Mitchell, 1997)

The second operation considers the removal of ash from the collection plates. Ash particles are dislodged via a process known as rapping and travel down vertically, towards the hoppers for disposal (Soud & Mitchell, 1997). The process of rapping can be carried out by numerous methods including mechanical techniques like hammer and anvil arrangements or pneumatic/electromagnetic impulse (Soud & Mitchell, 1997). According to Speight (2013) electrostatic precipitators can prove very capable at collecting fine particulate matter, delivering collection efficiencies of 90 to 97% when operating with high resistivity, low sulphur fly ash. For numerous years it has been known that the mineral properties of the ash particles in the flue gas, and specifically the related resistivity properties play an important role when considering ESP collection efficiency (McLean, 1976).

2.2. Electrical Resistivity

As far back as 1827, German scientist Georg Simon Ohm noted that an electrical current passing through a conducting wire is proportional to the voltage drop across the wire (Lowrie, 2010). This linear relation would later become known as Ohm's law and can be represented by Eq. 2-1:

$$V = I\,R \tag{2-1}$$

Where *R* is the resistance of the given conductor with a unit of ohm. Later experiments showed that differences in conductor cross-sectional area and length yielded varying resistances. These experiments lead to Eq. 2-2:

$$R = \rho\left(\frac{L}{A}\right) \tag{2-2}$$

Where ρ is the resistivity of the conductor with SI units of Ω m. Resistivity is predominantly used to determine important parameters like dielectric breakdown, dissipation factor, moisture content, mechanical continuity and several other material properties (Keithley, 2001). The reciprocal of resistivity is conductivity with units of Ω^{-1} m^{-1}. The resistivity of a material is considered an important material property in the determination of the resistance of a material (Heaney, 1999).

The basics principles of conductivity and resistivity can be explained by considering the free electron model. This model postulates that the electrons are detached from their respective atoms and are free to move throughout the volume of the sample (Haliday *et al*., 1970). The free electron model, with electrons moving from a low to a high electrical potential in the lattice, is illustrated in Figure 2-2. This explanation is considered an oversimplified model with several shortcomings (Heaney, 1999), and can be more accurately described with quantum mechanical principles.

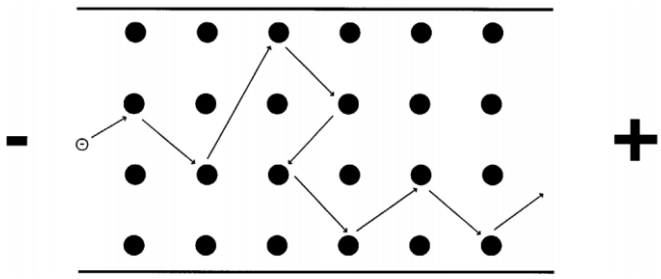


Figure 2-2: Free electrons moving throughout the lattice (Taken from: Heaney, 1999).

2.3. Resistivity of Various Materials

The behaviour of electrons vary depending on the type of material. In this section, the manner in which electrons behave in conductors, semi-conductors and insulators will be discussed. Section 2.3.1 will discuss the behaviour of electrons in conductors, Section 2.3.2 the behaviour in semi-conductors and Section 2.3.3 the behaviour in insulators.

2.3.1. Resistivity of Conductors

In solid-state physics the resistivity of materials is governed by their respective electronic band structure, which is derived from the quantum mechanical wave functions of electrons in solids. When considering a conducting metal such as copper, each copper atom has one valence electron in its 4s orbital (Here: $1s^2$ $2s^2$ $2p^6$ $3s^2$ $3p^6$ $3d^{10}$ $4s^1$). With the addition of another copper atom to the lattice, the electron of the second copper atom joins the electron of the first atom, leaving one 4s orbital with two electrons and one empty 4s orbital. As this trend continues “bands” start to appear as shown in Figure 2-3a, with the valence band containing the electrons and the conducting bands resembling the empty orbitals (Haliday *et al*., 1970).

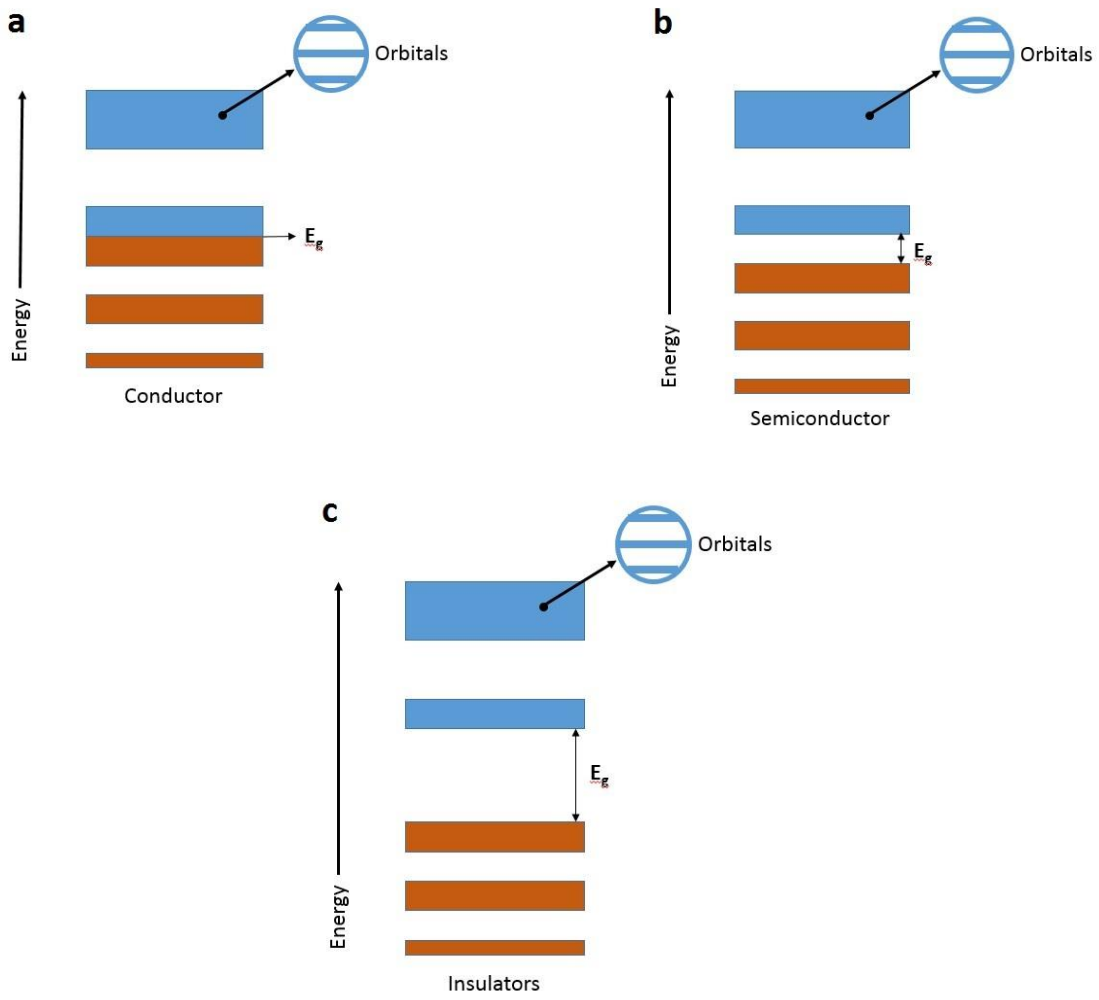


Figure 2-3: Band-gap pattern of a conductor (a), semiconductor (b) and insulator (c) (Adapted from: Haliday et al., 1970)

When considering a typical metal, the gap between the valence band and the conducting band is very small. This small gap makes it possible for electrons to jump from the valence band to the vacant levels in the conducting band with very little energy. Once electrons reach the conducting band they can freely move throughout the lattice of the material inducing electron flow.

Once the electrons have been excited to the conduction band and are able to freely move throughout the lattice they also start colliding with atoms in the lattice. The resistivity of a material is related to the mean free time between collisions of electrons with atoms (Lowrie, 2010). This relation can be represented by Eq. 2-3.

$$\rho = \frac{m}{n\, e^2\, \tau} \qquad (2\text{-}3)$$

From Eq. 2.3 it can be seen that an increase in the amount of electrons being exited from the valence band to the conduction band, allows more current to flow through the material, reducing the resistivity. An increase in the mean free time between collisions of electrons with atoms, allows the electrons to move through the material quicker, decreasing the resistivity. If the atoms are tightly packed in the lattice, the mean free time between collisions is reduced, leading to a higher resistivity (Heaney, 1999).

2.3.2. Resistivity of Semiconductors

The band structure of a semiconductor is much like that of an insulator. Unlike metals, a semiconductor has an energy gap between the valence band and the conduction band, however, the gap between the two bands is not as large as the gap of insulators (Haliday *et al*., 1970). Thus electrons can be excited to the conduction band but this requires more energy, as shown by Figure 2-3b. Semiconductors comprise mostly of the metalloid elements class.

2.3.3. Resistivity of Insulators

A material is said to be a non-conductor when little current exists when a voltage drop is applied. This occurs when the outer orbitals of the atom are completely occupied, and the molecule has no valence electrons. When two or more atoms are brought together in a lattice, the orbitals once again form valence bands and conduction bands but unlike metals, where these two bands are situated close to one another, the energy difference (E_g) between the two bands are very large, as shown by Figure 2-3c. For an electron to make the jump from the valence bands to the conduction band would require large amounts of energy (Smith & Hashemi, 2010).

2.4. Temperature Dependency of Resistivity

Like most physical properties resistivity also varies with temperature. The relation between resistivity and temperature can be considered linear for most metals with semiconductors and insulators having more complex relations (Haliday *et al*., 1970). The temperature coefficient of resistivity, α, represents the fractional change in the materials resistivity per unit change in temperature. The temperature coefficient of resistivity can be represented by Eq. 2-4.

$$\alpha = \frac{1}{\rho}\frac{d\rho}{dT} \tag{2-4}$$

The resistivity of metals generally increases with temperature, hence $d\rho/dT > 0$. This is due to the increased movement of the atoms which in turn leads to more collisions between the free electrons and the atoms, resulting in a positive α-value (Smith & Hashemi, 2010).

While the same principle hold for semiconductors, like silicone, these materials can sometimes have negative α-values which leads to a decrease in resistivity as the materials is heated. This is because the number of electrons entering the conduction band from the valence band also increases with temperature, resulting in an increased conductivity and reduced resistivity (Haliday *et al*., 1970).

The effect of temperature on resistivity can be shown by considering a superconductor. Experiments carried out by the Dutch scientist, Heike Kamerlingh Onnes, in 1911 showed that when the temperature of a mercury sample was reduced to 4 K, all traces of resistivity disappears giving raise to the phenomena of superconductivity. Superconductivity allows for transport of an electrical charge without any loss of energy to thermal energy (Haliday *et al*., 1970).

2.5. Size Dependency of Resistivity

While it has been stated previously that resistivity is a physical material property that does not change with geometry, extreme cases can lead to size dependent resistivity. As far back as 1938, pioneering researcher K. Fuchs observed varying resistivity values and derived the first expression for the resistivity of a thin film. Research interests have since shifted from thin films to small diameter conductors.

Recent studies have shown that when the diameter of a conductor is reduced to below the mean free path of the electron, the resistivity increased when compared to the bulk resistivity of the conductor. Steinhögl *et al*. (2002) proposed an explanation for this phenomenon and stated that non-specular electron scattering at the surface of the conductor and scattering of the electrons at the grain boundaries of the conductor can lead to an increased amount of collisions. This phenomenon is of relevance for cylindrical (Steinhögl *et al*., 2002) or rectangular (Marom *et al*., 2006) particles on a mesoscopic scale (10^{-6} – 10^{-8}m). However, size dependent resistivity can also be of relevance when considering fine powders.

The effect of size dependent resistivity on dust powders is most notably affected by the bulk density, porosity, surface area and size distribution of the powder (Xu *et al*., 2014). Fine powders have a larger specific surface area than coarse powders, increasing the contact area available for electron transfer, which in turn, lowers the surface resistivity. Alternatively, coarse powders have generally lower porosity values and increased solid to air ratios, resulting in a larger volume of solids available for electron transfer, effectively decreasing the volume resistivity (Qi & Yaun, 2013).

Recent studies have also revealed that particle size can affect the composition of ash, thereby also affecting the electron transfer mechanisms (Senior *et al*., 2000; Yu *et al*., 2005 and Nimomiya *et al*., 2004). In research conducted by Qi & Yaun (2013) the effect of particle size on resistivity, while also considering alkali-metal ion concentrations, was studied. It was shown that the alkali-metal concentration varied with particle size, which in turn lead to differences in resistivity values. They specifically revealed that particles below 75 µm showed a significant reduction in volume resistivity. The physical and chemical particle properties along with the temperature dependency of surface and volume resistivity makes resistivity predictions based on size distribution a complex exercise (Xu *et al*., 2014).

2.6. Fly Ash Resistivity

One of the key parameters significantly affecting the collection efficiency of electrostatic precipitators is the electrical resistivity of the fly ash (Bickelhaupt, 1975). The electrical resistivity of fly ash is influenced by a number of factors, where the chemical composition and physical properties of the original coal, the method and parameters to which the coal was pulverized before combustion, the method and conditions of the combustion process and flue gas conditions are the most important ones (Xu *et al*., 2014; Jędrusik & Świerczok, 2009).

While resistivity is a dominant parameter governing the ash collection efficiency, ESPs can still operate over a wide range of resistivity values. Electrostatic precipitators have been known to operate effectively at resistivities as high as 10^{11} Ω cm. Fly ash with a high resistivity value is difficult to charge and does not easily give up its negative charge once it reach the collection plates. This results in ash particles exiting the precipitator fields without being collected (inadequate charge imparted to the ash particle) or the build-up of a dense barrier of fly ash on the ESP collection plates (Jaworek *et al*., 2004). Both these occurrences severely limit ESP performance and can, in turn, lead to back corona, a phenomenon that occurs when the accumulated charge of the particles is unable to leak to the ground. Low resistivity values can also have a negative effect on ESP performance with ESPs being able to collect particles with resistivity values as low as 10^3 Ω cm. In the event of low resistivity fly ash, the highly conductive particles discharge easily upon reaching the collection plate, leading to re-entrainment of the ash particles (Jaworek *et al*., 2004). In Table 2-1 the performance of ESP units as a function of fly ash resistivity is given.

Table 2-1: Industrial ESP performance as a function of fly ash classification and resistivity (Taken from: Chandra, 2013)

Resistivity Ranges	**Classification**	**ESP Performance**
$(10^4 – 10^8)$ Ω cm	Conductive Ash	Low Collection Efficiency
$(10^8 – 10^{10})$ Ω cm	Normal Resistivity	Moderate Collection Efficiency
$(10^{10} – 10^{11})$ Ω cm	Moderate Resistivity	High Collection Efficiency
$(10^{11} – 10^{13})$ Ω cm	High Resistivity	Low Collection Efficiency

The resistivity of fly ash can be subdivided into two distinct areas known as surface resistivity and volume resistivity (Bickelhaupt, 1975, White, 1974). At temperatures between that of volume resistivity and surface resistivity a combination of the two electron transfer mechanisms occurs, with electrons travelling via the conducting layer on the surface and through the bulk of the material to a comparable extent. Volume resistivity is predominantly dependent on the properties of the material, while surface resistivity is dependent on the adsorption of physical or chemical species on the surface of the ash particle (Bickelhaupt, 1975). Bickelhaupt (1975) states that at temperatures between 250 and 450°C, volume resistivity is the dominant mechanism, while temperatures below 150°C will experience electron transfer due to surface resistivity, as depicted in Figure 2-4.

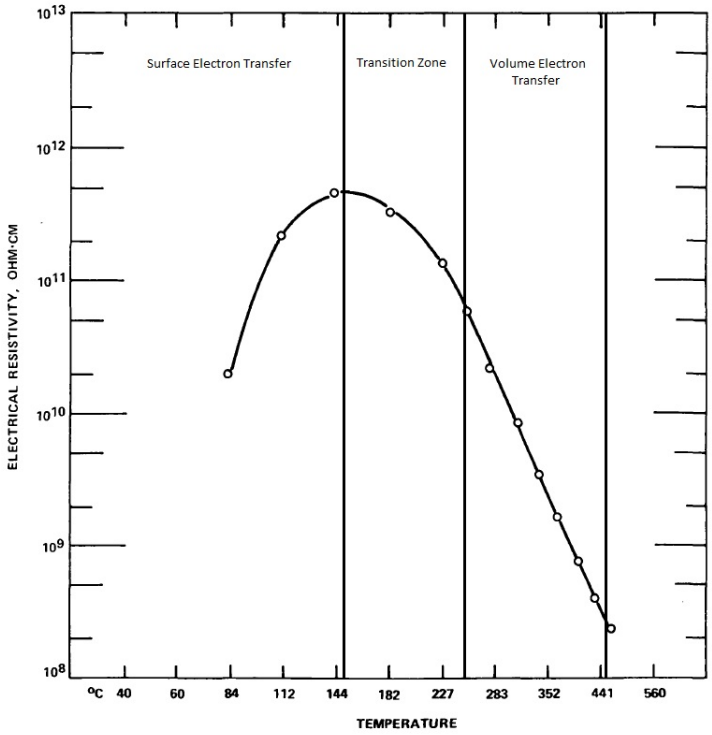


Figure 2-4: Typical graph of the log of resistivity as a function of temperature (Taken from Bickelhaupt, 1979)

2.6.1. Volume Resistivity

The electron transfer through the bulk of an ash particle is dependent on material composition and temperature, occurring either via ionic conduction or electronic conduction (White, 1974). The volume resistivity of insulators, such as glass or ceramics, decrease with an increase in temperature. This trend can be described by Eq. 2-5, an exponential law derived from principles of quantum mechanics (White, 1974).

$$\rho = A\, e^{\left(\frac{-E}{k\,T}\right)} \qquad (2\text{-}5)$$

Research has shown that the volume resistivity of a majority of industrial dusts or fumes may be approximated by Eq. 2-5 over a wide range of temperatures (Bickelhaupt, 1979, White, 1974)

2.6.2. Surface Resistivity

Electron transfers via the surface of an ash particle takes place in a film of physically- or chemically adsorbed species such as water and SO_3 (White, 1974). Moisture is normally present in flue gas due to the combustion process with concentrations varying between 5 to 10 vol% and is physically adsorbed on the ash particle surface (White, 1953, White, 1974). Species which act as resistivity reducing agents, commonly known as conditioning agents, are also present in flue gas and can be chemically adsorbed on the surface of an ash particle (White, 1974). The binding energy associated with a physically adsorbed specie, like water, on ash particles is considerably lower than the binding energy of a chemically adsorbed species, making chemical conditioning agent like SO_3 much more effective in reducing resistivity than physically adsorbed components like water.

2.7. Experimental Determination of Resistivity

Since resistivity is an important material property with various applications, accurate measuring techniques and equipment have been proposed over the years. Since the resistivity of materials, even at room temperature, can vary with as much as 20 orders of magnitude, a wide range of techniques have been designed. Some of those techniques are reviewed in the sections below.

2.7.1. Two-Point Technique

One of the most rudimentary methods is the two-point technique, which entails first measuring the resistance of the material. This is done by connecting copper wires to both ends of the material and applying voltage across the terminals. The current is then measured in series with an ammeter. By using Ohm's law, the resistance of the material can be determined (Heaney, 1999), whereby the dimensions of the material are used to compute the resistivity of the material as shown by Eq. 2-6:

$$\rho = \frac{R\,A}{L} \tag{2-6}$$

In Figure 2-5, the conventional configuration of the two-point technique is shown.

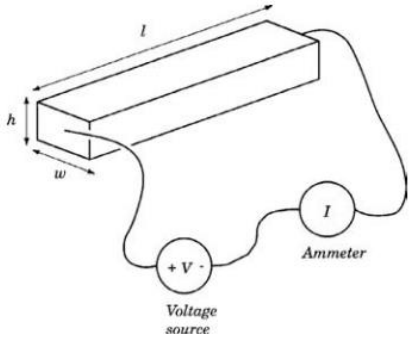


Figure 2-5: Configuration of two-point method (Taken from: Heaney, 1999)

In practice the two-point method is often considered to be unreliable, due to the presence of additional resistances between the material and connecting wires, in turn, leading to higher resistivity values than the actual values. Additionally, complications can arise from the connection of the metallic connecting wires to a semiconducting sample, yielding faulty estimates for the resistivity (Heaney, 1999).

2.7.2. Four-Point Technique

The four-point technique overcomes most of the issues faced by the two-point technique and is considered the most common method to measure the resistivity of a semiconductor (Keithley, 2005). Two of the four probes are used to source the current while the remaining two probes are used to measure the voltage drop. The use of four probes eliminates measurement errors due to probe resistances. When using the four-point method the resistivity can be calculated using Eq. 2-7.

$$\rho = \frac{V\,A}{I\,l'} \tag{2-7}$$

In Figure 2-6, the conventional configuration of the four-point technique is shown.

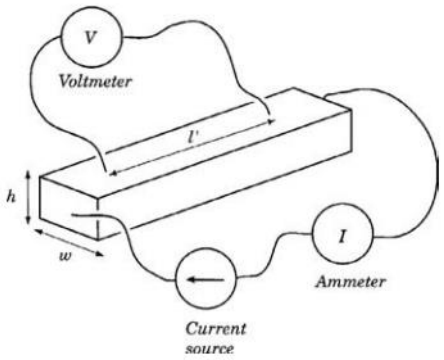


Figure 2-6: Configuration of four-point method (Taken from: Heaney, 1999)

2.7.3. High Voltage Conductivity Cell

When considering a semiconducting or insulating material, the resistivity values are considered high, sometimes even in the order of 10^{19} Ω cm. The two methods described in Section 2.7.1 and 2.7.2 cannot be used to accurately measure high resistivity values (Heaney, 1999). In order to measure these values, a large amount of energy is required to excite the electrons from the valence band to the conduction band, necessitating the need for high voltages to accurately measure resistivity.

In the early stages of fly ash resistivity research, the high voltage conductivity cell was developed and used to measure resistivity in a laboratory. The electrodes of the high voltage conductivity cell, depicted in Figure 2-7, were connected to an electrometer, an oscillograph and a high voltage source (White, 1953). The high voltage conductivity cell was housed inside a temperature controlled oven fitted arrangements to control humidity.

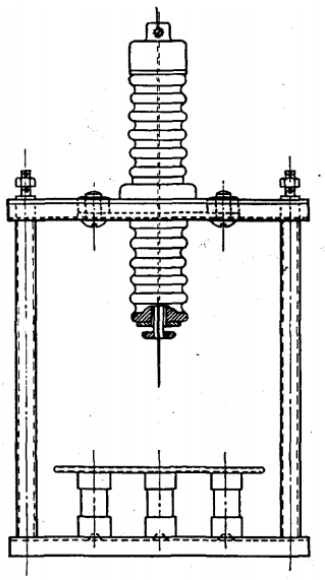


Figure 2-7: High voltage conductivity cell (Taken from: White, 1953)

Using this apparatus, the resistivity of the fly ash can be determined by using one of two independent methods. The first method entails placing a sample of dust on the grounded plate and lowering the high voltage electrode until light contact is made with the ash layer. The voltage is then gradually increased until spark-over occurs between the high voltage electrode and the grounded plate (White, 1953). The resistivity of the fly ash sample can then be determined from the dimensions of the ash sample, the current passing through the dust layer and the voltage applied just before spark-over occurred. The second method proceeds in the same manner as the first, exchanging the high voltage electrode for a corona-point electrode. The voltage is once again increased until a luminous back-discharge crater appears in the dust layer. The corona current value just before the current discontinuity is observed and corresponds with the breakdown current density, which can then be used to estimate ash resistivity (White, 1953).

2.7.4. Parallel Plate and Radial Flow Cells

In 1981 attempts were made by the IEEE to standardize the procedure for the testing a fly ash resistivity from an “as submitted” sample. The standard developed by the IEEE was developed to *i)* set in place resistivity testing protocols, *ii)* standardize laboratory equipment used for measurements and *iii)* propose acceptable uncertainty ratios for both within-laboratory and inter-laboratory testing (IEEE std. 548, 1984). The test rig, as standardized

by the IEEE, later became known as a resistivity oven. In Figure 2-8 the general apparatus and the arrangement of the various subsystems is depicted.

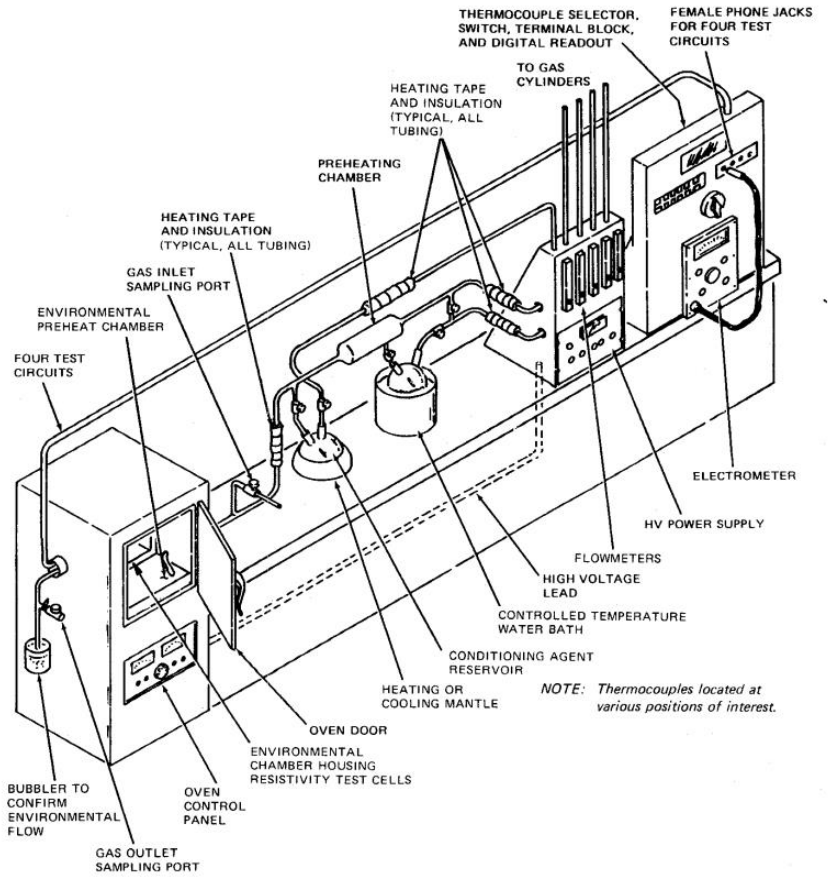


Figure 2-8: General apparatus arrangement for IEEE compliant resistivity oven (Taken from: IEEE std. 548, 1984)

The apparatus depicted in Figure 2-8 houses one or more resistivity test cells, enclosed in an environmental chamber. The apparatus is designed to maintain intimate contact between the gaseous environment and the test sample (IEEE std. 548, 1984). The thermally controlled environmental chamber can be set to maintain temperatures between 95 °C and 450 °C while a high voltage supply is used to impress a direct-current high voltage on the fly ash layer. The environmental chamber is supplied with either a water-air mixture or an oxygen-carbon dioxide-nitrogen-water mixture. The IEEE standards utilized an ANSI/ASME PTC 28-1965 guarded, parallel plate test cell, as depicted in Figure 2-9

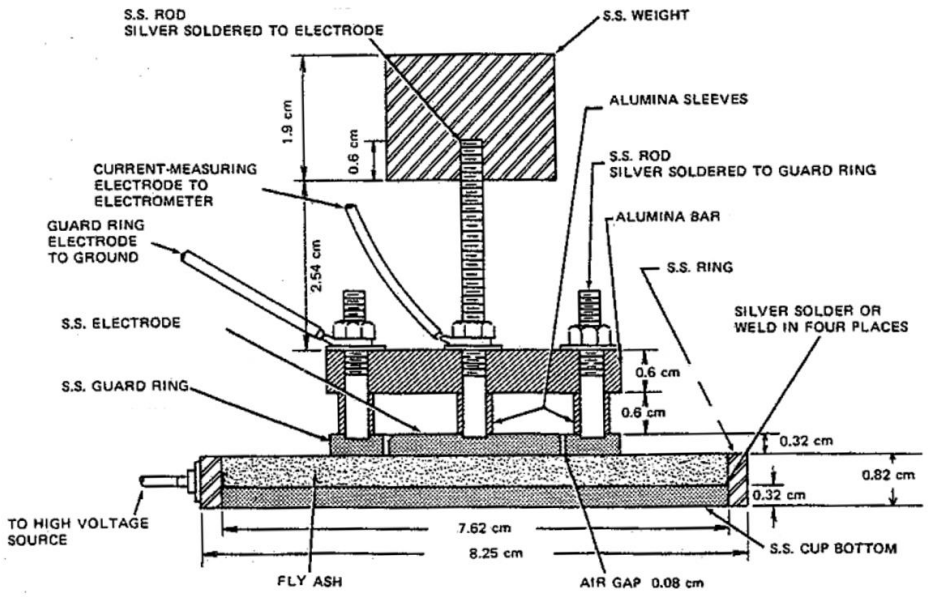


Figure 2-9: ANSI/ASME PTC 28-1965 guarded, parallel plate test cell (Taken from: IEEE std. 548, 1984)

The addition of conditioning agents such as sulphur trioxide was beyond the scope of the 1984 revision of the IEEE standards. Research conducted by Bickelhaupt (1978) was published to improve on the standard guarded, parallel plate resistivity cell. It was found that a parallel plate resistivity cell subjected to an environment at 145°C, 9 vol% moisture and 10 ppm SO_3 for 24 hours showed large concentration gradients of adsorbed acid through the ash layer (Bickelhaupt, 1978) and, therefore, the conventional configuration could not be used for SO_3 conditioning. A new resistivity cell was developed by Bickelhaupt (1978) to address the concentration gradient of adsorbed acid. The new resistivity cell was known as a radial flow resistivity cell and is depicted in Figure 2-10.

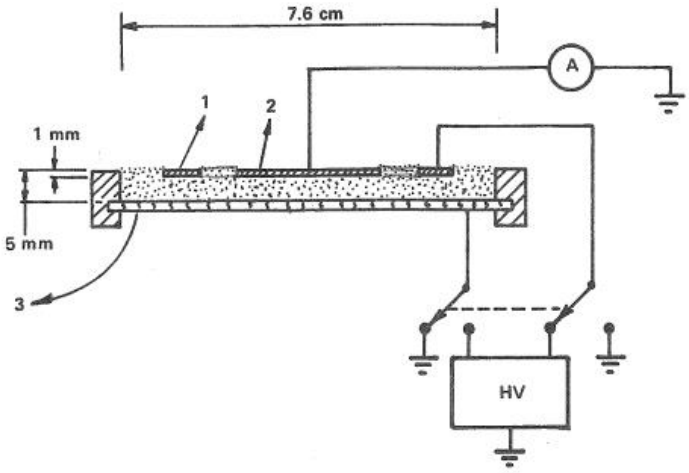


Figure 2-10: Combination parallel plate- radial flow resistivity test cell (Taken from: Bickelhaupt, 1978)

Unlike the guarded, parallel plate resistivity cell, the applied voltage of the radial flow resistivity cell is connected to the guard ring electrode (1), measuring current between the guard ring electrode (1) and the current measuring electrode (2). The resistivity cell, as suggested by Bickelhaupt, can also be used as a parallel plate resistivity cell. Should the voltage be applied to the bowl (3), the current can be measured between the guard ring electrode (1) and the current measuring electrode (2), the cell would function as a parallel plate resistivity cell. When used in the parallel plate configuration, the resistivity cell will function such as those described by IEEE std. 548 of 1984. Bickelhaupt (1978) also compared the different configurations of the resistivity cell and found that the two configurations gave similar resistivity results in a humidified environment but showed large differences in resistivity when adding a conditioning agent, such as SO_3, to the environment, with the radial flow configuration giving accurate resistivity data when introducing a conditioning agent (Bickelhaupt, 1978)

2.7.5. Resistivity Measurement Considerations

Measuring resistivity accurately is considered a difficult task especially when measuring high resistivity materials. Common measurement errors can occur ranging from environmental interference to equipment malfunctions (Keithley, 2005). Electrostatic interference can cause the material to become electrically charged. This occurrence is not of major concern when working with low resistivity materials as the charged material quickly dissipates the charge, however, this can cause errors and unstable readings when working with high

resistivity materials because the charge will not decay quickly. Electrical interference can be avoided by enclosing the testing equipment in an electrostatic shield made from a conductive material. Additionally, the cabling of the testing equipment can be shielded to further eliminated interference. Insulation resistance of the apparatus components (cables, probes and test fixtures) can lead to leakage current. Leakage current can be avoided by installing high quality insulators and reducing the humidity of the testing area. In extreme cases where accurate measurements are required the photoconductive effect caused by light can cause inconsistent measurements. This can be avoided by ensuring the measurements be taken in a dark chamber.

2.8. Coal Ash Resistivity Modelling

With fly ash resistivity being one of the key design factor of an ESP, accurate resistivity data is essential when designing a new precipitator or operating an existing ESP (Bickelhaupt, 1975; Bickelhaupt, 1979). Fly ash resistivity can be determined by either laboratory testing or by theoretical determination (Van Wyk, 2015).

Over the years several precipitator manufacturers have developed numerous proprietary methods for predicting fly ash resistivity. These techniques include various simplified lab setups, extensive experience or correlations based on the ash composition and physical properties (Bickelhaupt, 1975, McLean, 1976). These methods are generally not publicly available and may only yield acceptable results for certain ashes (Bickelhaupt, 1974). Resistivity predicative techniques can be subdivided into two different types. The first type seeks to determine the resistivity of an ash sample by considering the particulate nature of the sample, utilizing a mathematical model to predict the electrical properties of the sample (McLean, 1976). Predictive models such as these consider the geometry of individual particles, the compaction of the dust layer, contact resistances between particles and numerous other physical properties (McLean, 1976). Such models can also take into account the effect moisture on surface resistivity at various temperatures. The second type of predictive technique seeks to determine the components responsible for electron transfer and only considers the chemical composition of the ash sample (Bickelhaupt, 1979, McLean, 1976). The second type of model has become the favoured method, with this type of predictive technique being extensively developed by authors such as Bickelhaupt.

The Bickelhaupt predictive model was developed using a large selection of coals from North America and requires as only input the elemental composition of the fly ash sample. The

Bickelhaupt model can predict the surface resistivity, volume resistivity and the effect of conditioning agents, such as sulphur trioxide, of North American ashes with a considerable degree of accuracy (Harrison *et al.*, 1988.). Further research has, however, shown that the Bickelhaupt model is less accurate in the prediction of resistivity when ash samples of different origin, specifically ash samples which a significant difference in elemental composition compared to the North American ashes, are considered (Chandra *et al.*, 2006; Van Wyk, 2015)

Previous studies have sought to develop and improve on relations between ash composition and fly ash resistivity (Chandra *et al.*, 2006 & Van Wyk, 2015). Studies conducted by Chandra *et al.* (2006) employed empirical modelling to better describe the resistivity of Indian fly ash samples. The modelling included alterations to the coefficients used in the standard Bickelhaupt model to describe the elemental ash composition. The results of the empirical modelling are compared with the standard Bickelhaupt model in Figure 2-11. The modifications made to the Bickelhaupt model better predicted the resistivity of Indian ashes over the entire temperature range.

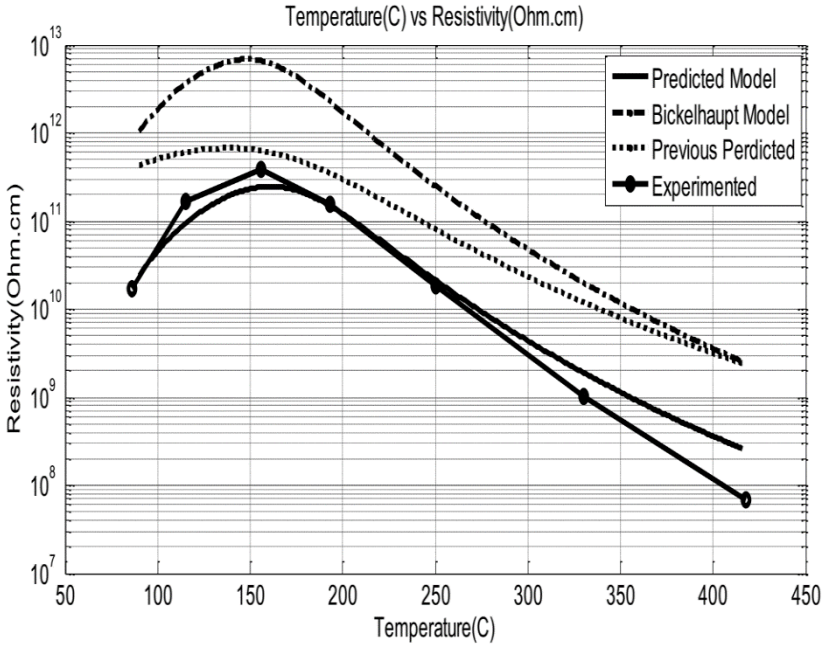


Figure 2-11: Effect of chemical composition (Na, Ca, Fe, K, Mg and SO_3) on fly ash resistivity (Taken from: Chandra et al., 2006)

Van Wyk (2015) had similar success at better describe the resistivity of South African fly ashes. Van Wyk (2015) employed statistical modelling and fly ash mineralogy to derive a

correction factor. When applied to the standard Bickelhaupt model, the correction factor better describes the fly ash resistivity of South African ashes. The correlation between the measured resistivity, the standard Bickelhaupt model and the modified Bickelhaupt model is depicted in Figure 2-12. The correction factor was only applied to the surface resistivity region as this is the standard operating window of electrostatic precipitators.

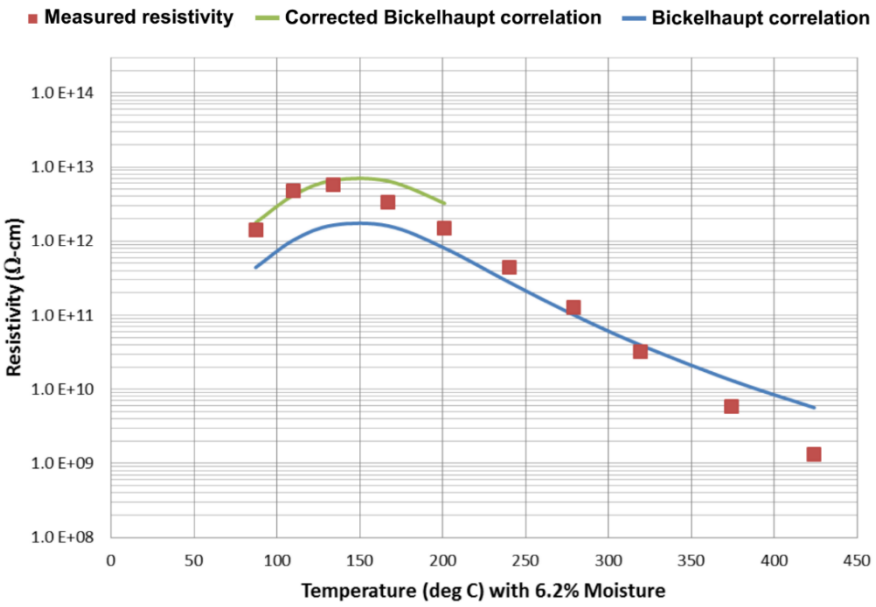


Figure 2-12: Corrected fly ash correlation curve as a function of temperature (Adapted from: Van Wyk, 2015)

2.9. Fly Ash Composition

In the early stages of fly ash resistivity research, it was found that the resistivity of a sample, specifically in the low temperature region, differed when comparing data acquired during the ascending stage to those acquired during the descending stage. It was hypothesised that this substantial difference could be related to volatile components, other than water, present in the fly ash (White, 1953). Since air is normally used in the determination of resistivity, mineral transformations can take place during the ascending phase with parts of the sample, *e.g.* unburnt carbon, reacting with oxygen.

Attempts were made to isolate the species responsible for the difference in resistivity. An ash sample of known resistivity was “washed” with distilled water and the resistivity of the washed and dried ash sample compared. In Figure 2-13, the effect of washing on the resistivity of an ash sample is presented.

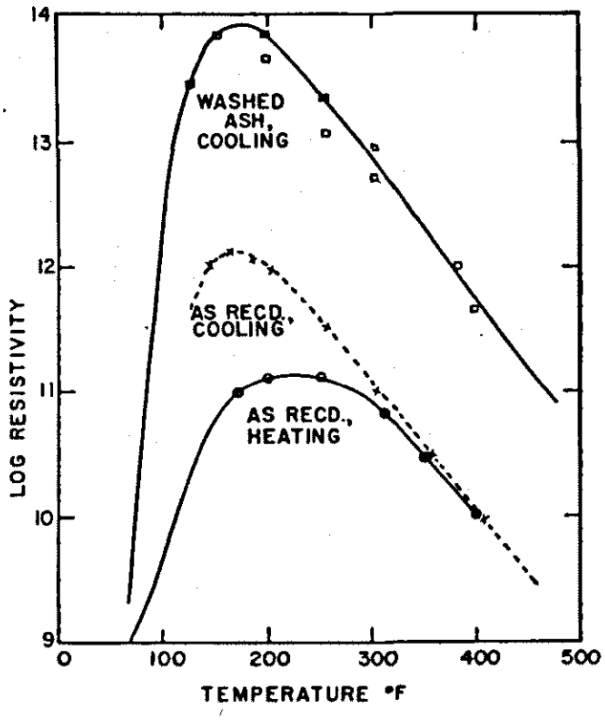


Figure 2-13: Comparison between ascending, descending and washed resistivity as a function of temperature (Taken from: White, 1953)

The washed ash sample showed a resistivity peak raised by a factor of approximately 100. The filtrates of the washing process was subsequently analysed to determine the water soluble component which acts as a natural conditioning agent. The filtrates were found to contain predominantly sulphates and lime (White, 1953). It was concluded that sulphates were the most probable soluble specie responsible for the difference between the ascending and descending test results. A small quantity of sulphur is always present in coal with the concentrations ranging from trace amount up to 5% (White, 1953). During the combustion process taking place in PF boiler, the sulphur is oxidized to SO_2 and small quantities of SO_3. Subsequent research confirmed that the bulk of sulphur was present on the surface of ash particles having been adsorbed from SO_3 or H_2SO_4 (White, 1953). The sulphur present on the ash particle acted as a natural conditioning agent and would reduce the resistivity in the ascending stage, being subsequently devolatilized at elevated temperatures leading to elevated resistivity values in the descending stage (White, 1953).

Both the surface and volume resistivity mechanisms rely on the composition of the given fly ash. Volume resistivity mostly depends on sodium ions as the principle charge carrier while surface resistivity depends on electrolytic or ionic mechanisms occurring on the surface of

the particle producing a conducting layer (Bickelhaupt, 1975). Bickelhaupt (1975) continued his research on the composition of fly ash and its effect on the resistivity, conducting transference experiments. These transference experiments entailed exposing fly ash to high field strengths for several hundred hours. It was found that alkali metal ions migrated towards the negative electrode during the transference experiment. This revealed the importance of alkali metal ions in the surface resistivity mechanism.

Following the transference experiments, further research was done to determine which alkali metal ions are most significant in the electron transfer mechanism. Experiments showed that sodium and lithium ions play an important part in the surface resistivity mechanism (Bickelhaupt, 1975). Additionally, it was observed that potassium could also play an important role in electron transfer, but only when the iron content in the ash is sufficient (Bickelhaupt, 1975). These findings were confirmed by Qi and Yaun (2013) who found that the sodium ions were the principal alkali metal ions responsible for electron transfer. Qi and Yaun (2013) hypothesized that the ability of the sodium, lithium and potassium ions to act as charge carriers is due to the fact that these metal ions have few valence electrons, facilitating electron migration at certain voltages. Table 2-2 shows the various fly ash components and the effect they might have on the resistivity.

Table 2-2: Effect of coal ash composition on resistivity (Taken from: Chandra, 2013)

Chemical Component	Property	Effect on Resistivity
SiO_2	Insulator	Increase
Al_2O_3	Insulator	Increase
CaO	SO_3 Absorber	Increase
Fe_2O_3	Increases alkali ion solubility and mobility	Decrease
Na_2O	Ion Contributor	Decrease
P_2O_5	Ion Contributor	Decrease
K_2O	Ion Contributor	Decrease
SO_3	Ion Contributor	Decrease
Li_2O	Ion Contributor	Decrease
TiO_2	-	-
MgO	-	-

More recently research has been conducted to gauge the effect ash mineralogy might have on resistivity. The research conducted by Van Wyk (2015) sought to improve on the

accuracy of the Bickelhaupt model when applied to South African ashes. A correction factor, taking into account the ash mineralogy, was developed that when applied to the Bickelhaupt model showed improved accuracy. The minerals found to have the most significant effect on resistivity was calcite, Mg(Si)-oxide and anhydrite.

2.10. Resistivity of South African Fly Ashes

Resistivity analysis on South African ashes have scarcely been published in the past with an ash sample being sent by Eskom to the Indian Institute of Technology in 2009 as one of the first in open literature. The ash sample was tested at 9 vol% moisture for both ascending and descending stages (Van Wyk, 2015). The sample showed a peak resistivity of 1×10^{12} Ω cm at 150°C which was considered high for effective ESP performance (Chandra, 2013). The sample also showed a difference between the ascending and descending stages which was attributed to unburnt char in the ash sample (Van Wyk, 2015). Resistivity testing has also been conducted on an undisclosed ash sample from the Eskom fleet at moisture levels of 0 - 13 vol% (Chauke, 2013), at temperatures of 95 - 215°C and it is not specified whether the data was acquired on the ascending or descending stage. In Figure 2-14, the resistivity of the undisclosed sample is given as a function of temperature at various ambient moisture levels.

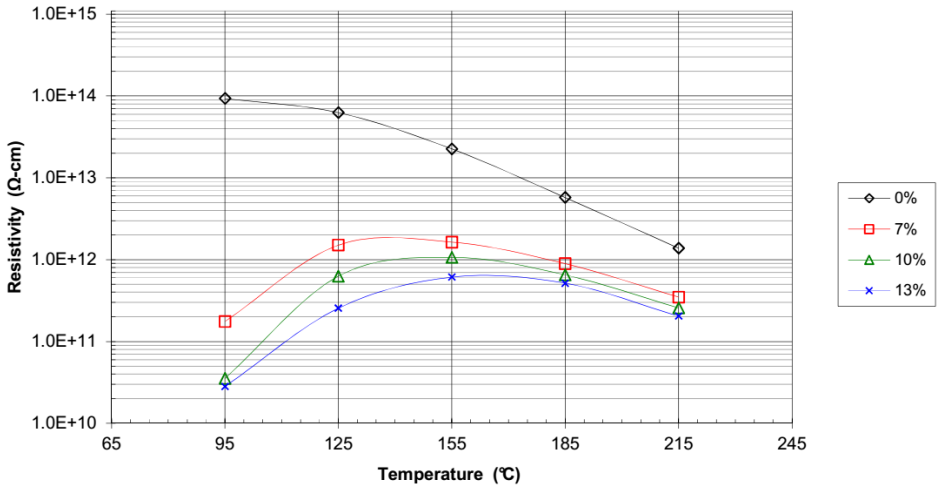


Figure 2-14: Ash Resistivity as a function of temperature for various ambient moisture contents (Taken from: Chauke, 2013)

Chauke (2013) noted a reduction in fly ash resistivity as the moisture content increased. It was concluded that the reduction in resistivity is due to a coating of moisture on the surface of the ash particle, creating a path for the corona current to leak to ground.

Recently, resistivity analyses were conducted on 10 ash samples from the Eskom fleet to determine the effect of sulphur trioxide on South African ashes. It was found that South African fly ashes showed a significantly higher resistivity when compared with ash samples from North America, in some cases differing as much as 2 orders of magnitude (Van Wyk, 2015). It was found that South African ashes strongly responded to conditioning with sulphur trioxide. In Figure 2-15, the effect of SO_3 on the resistivity of a typical South African coal ash is depicted.

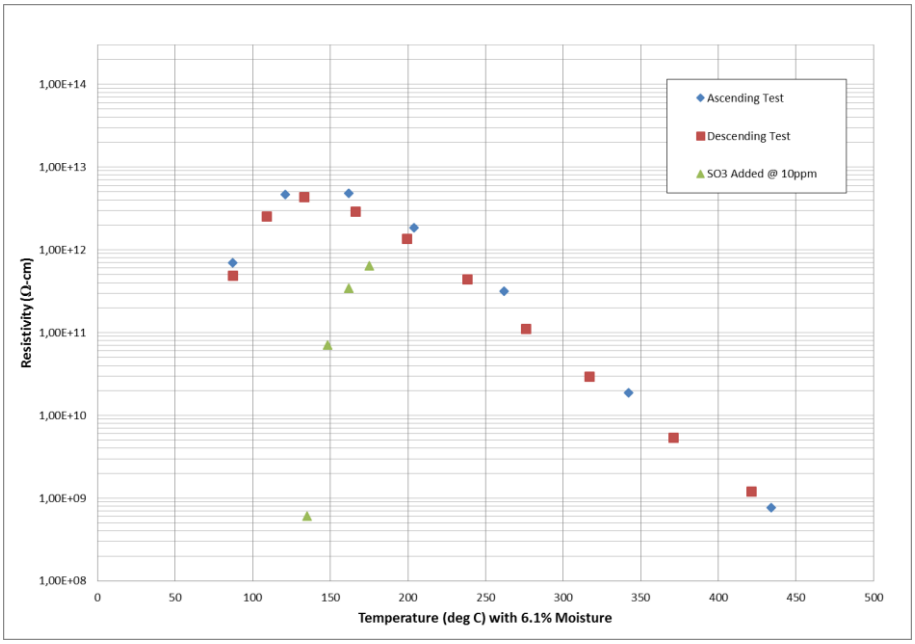


Figure 2-15: Resistivity as a function of temperature with 10 ppm SO_3 (Adapted from: Van Wyk, 2015)

Van Wyk (2015) found that the resistivity of the majority of the ashes sampled could be reduced to 1 x 10^{11} Ω cm with the addition of SO_3. In some cases the addition of SO_3 yielded three orders of magnitude reduction in resistivity.

The resistivity of South African fly ash reported in literature (Chauke, 2013; Van Wyk, 2015) is several orders of magnitude higher than those reported for American ashes, with American ashes seldom exceeding 1 x 10^{12} Ω cm (Bickelhaupt, 1979). Indian ashes prove more relatable to South African ashes, with resistivity values ranging from 4.5 ×10^{12} Ω cm to 3.4 ×10^{13} Ω cm (Chandra *et al.,* 2006)

2.11. Flue Gas Conditioning

A number of parameters can aid in increasing ESP efficiencies namely; changing the feed coal characteristics, an increase in collection plate area, wet ESP to minimize re-entrainment, varying flue gas temperatures and lastly the addition of chemical components to modify the electrical characteristics of the fly ash (Ross, 1972; Parker, 1997). A number of these parameters can prove difficult and costly to alter. Changing the feed coal is not considered a viable option as most power stations receive coal from nearby coal mines and the transportation cost associated with shipping an alternative coal to the powers station is costly. The enlargement of ESP collection plate area entails a complete geometry change of the ESP housing, this option is considered uneconomical due to the modification costs associated with an ESP rebuild. The operating costs associated with wet ESP systems are also considered too high, additionally, wet ESP systems are prone to lump formation of ash, which in turn degrades the ESP construction materials (Hankins & George, 2011; Lister & Peterson, 1996).

The last option to be considered is the addition of chemicals to modify the characteristics of the fly ash, a process broadly known as flue gas conditioning (FGC). This approach offers reduced capital cost in terms of ESP modifications, while still delivering an effective reduction in emission levels. This method is considered more flexible, being able to effectively operate over a wide range boiler loads, ESP voltages and coal types (Shanthakumar *et al*., 2008a).

Various approaches and chemicals are available to alter the physical and chemical properties of the fly ash. Some of the chemicals generally used for flue gas conditioning are sulphur trioxide, sulphuric acid, ammonium sulphate, ammonium bisulphate, sulphamic acid and ammonia (Ray, 2004; Oglesby & Nichols, 1978). Additionally, either steam or water can be injected into the flue gas stream in an attempt to increase the collection efficiency (Shanthakumar *et al*., 2008b). These substances are specifically chosen to perform one of three tasks namely: to modify the surface of the fly ash (whereby the surface resistivity is decreased), to increase the inter-electrode space charge and lastly to increase dust cohesion (minimizing re-entrainment during rapping) (Shanthakumar *et al*., 2008b). The chemicals of concern to this study are those capable of altering the resistivity of fly ash.

The most basic and inexpensive method of flue gas conditioning is the injection of steam or atomized water into the flue gas steam. The injection of H_2O reduces the temperature and increases the relative humidity of the flue gas. The slight reduction in temperature reduces the overall fly ash resistivity due to the temperature dependency of resistivity. The increase

in relative humidity allows for the formation of a very thin moisture layer on the surface of the fly ash particles. This thin layer increases the surface conductivity, facilitating the transfer of electrons along the surface of the particles (Ray, 2004). The result of water injection is a reduction in both surface and volume resistivity which leads to increased collection efficiencies without significant gas volume or temperature changes. This method of flue gas conditioning does however have some downfalls. The slight reduction in temperature might lead to acid condensation, which might cause corrosion of the ESP equipment. Additionally, slight lumping of fly ash might occur which will impede the working of the ash hoppers (Shanthakumar *et al*., 2008b).

Sodium species are the principle charge carriers in ash and can aid in the transfer of electrons making sodium injection a viable conditioning method. Sodium conditioning, as with water injection, also relies on increased surface conduction to increase the collection efficiencies of ESPs. Unlike water injection, sodium conditioning does not require any chemical to be injected into the flue gas but rather the addition of sodium, either sodium carbonate or sodium sulphate, to the coal before milling (Shanthakumar *et al*., 2008b). The addition of sodium to the coal alters the morphological characteristics of the fly ash, increasing the amount of sodium ions available for electron transfer (Gooch *et al*., 1981). The ability of sodium conditioning to function correctly is somewhat dependent on original coal content with high calcium coal requiring additional sodium to adequately reduce the surface resistivity (Shanthakumar *et al*., 2008b).

Sulphur trioxide (SO_3) conditioning is the most commonly used type of flue gas conditioning, capable of effectively treating high resistivity fly ashes (Shanthakumar *et al*., 2008b). Sulphur trioxide is injected into the flue gas stream and proceeds to react with the moisture present in the flue gas, forming sulphuric acid. The resultant sulphuric acid is then absorbed on the surface of the fly ash particles, forming a thin conductive layer on the surface which can facilitate the transfer of electrons (Shanthakumar *et al*., 2008a). Numerous SO_3 conditioning systems are available ranging from direct injection of SO_3, to catalytic processes with SO_2 oxidation and injection (Shanthakumar *et al*., 2008a). An important consideration with SO_3 conditioning is the acid dew point, insufficient flue gas temperature can cause acid condensation on the ESP ducting and equipment leading to extreme corrosion (Shanthakumar *et al*., 2008a).

3. Sample Preparation and Analysis

In Chapter 3 fly ash sampling along with sample characterization and analysis is discussed. In Section 3.1, the criteria for sample selection are given, together with the ash sampling process, sampling locations and sample storage procedures. In Section 3.2, the sample preparation process is discussed while in Section 3.3, the analytical methods to be used for ash characterization are presented. In Section 3.4, the characterization results are presented and discussed.

3.1. Fly Ash Sampling

Three ashes derived from coal, fired in conventional PF power plants, were selected for analysis and characterization. The ash selection process was based on the current collection method of the power stations, where only power stations utilizing electrostatic precipitators were considered. Furthermore, previously estimated resistivity values and current particulate emission levels of the ESP units were considered. Coal ashes from power station A (PS A), power station B (PS B) and power station C (PS C) were selected, where the location of the power stations is given in Figure 3-1, relative to the capital of South Africa, Pretoria.



Figure 3-1: Fly ash sampling sites

PS A was selected for its low ash resistivity and low particulate emissions levels, PS B was selected for its high resistivity and low particulate emissions levels and PS C for its medium to high resistivity and high particulate emission levels (Patel & Swart, 2014, Van Wyk, 2015).

The ash samples were collected directly from the power stations to ensure industrial representative conditions. The location of the ash sampling sites and the mine/coalfield where their respective feed coal was sourced is shown in Table 3-1 (Hancox & Götz, 2014).

Table 3-1: Fly ash sampling sites

Power Station	Location	Coal Mine	Coal Field
PS A	Sasolburg, Free State	New Vaal Colliery	Vereeniging-Sasol Coalfield, Opencast
PS B	Lephalale, Limpopo	Grootegeluk Coal Mine	Waterberg Coalfield, Opencast
PS C	Standerton, Mpumalanga	New Denmark Colliery	Highveld Coalfield, Seam No. 4

Between 350 and 460 kg of fly ash was collected from each power stations, with each ash sample being stored in two sealed 220 litre plastic drums. Both power stations A and B have Ash Resources divisions, South Africa's largest supplier of fly ash products, which facilitated ash collection (Ash Resources, 2017). For PS A and PS B fly ash is routed from below the ESP bunkers to their respective Ash Resources facility, where the ash samples were subsequently collected. Fly ash from PS C was collected from the ESP ash hopper conveyors, upstream of the ash dumps.

3.2. Sample Preparation

The selected ash samples were cone and quartered to 10 kg, to be used for testing, characterization and archiving. Further splitting of the 10 kg ash sample was done using a SMC rotary splitter set at 14 rpm to limit the amount of dust produced. Representative samples from the rotary splitter were used for resistivity measurements, particle size distribution (PSD), X-Ray Diffraction (XRD), X-Ray Florescence (XRF), QEMSCAN and archiving as illustrated in Figure 3-2.

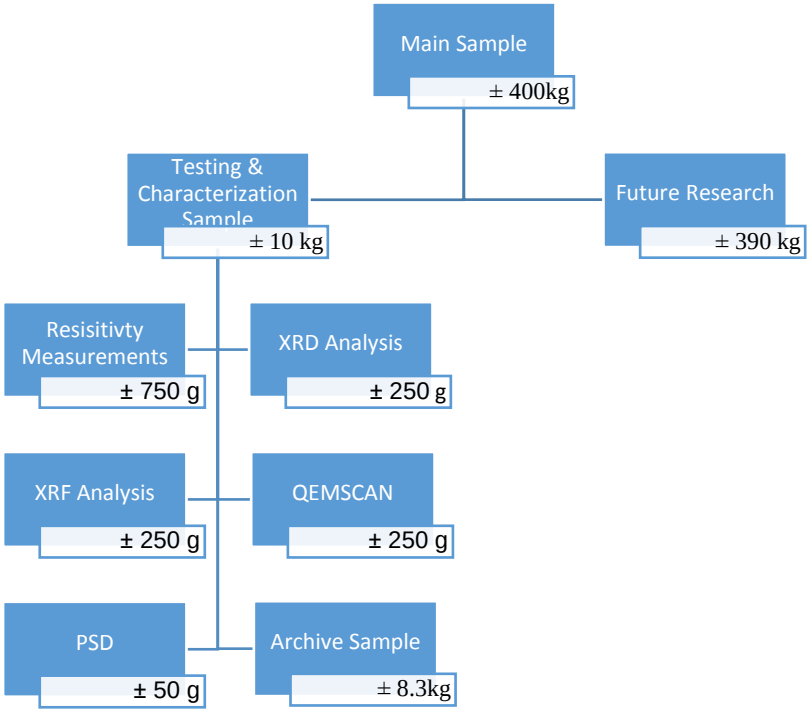


Figure 3-2: Sample preparation and sample size for various analyses

The ash sample allocated to resistivity testing was further split, using a rotary splitter, to acquire individual samples of ±50 grams each, and stored in sealed bags.

3.3. Ash Analysis & Characterization

3.3.1. Particle Size distribution

The particle size distribution of the coal ashes was determined using a Malvern Mastersizer 2000 located at the NWU, Potchefstroom Campus, School of Chemical and Minerals Engineering, according to ISO std. 13320 of 2009. See Appendix B, Table B-1 for Malvern Mastersizer settings.

3.3.2. Proximate Analysis and Calorific Value

The proximate analysis and calorific value determination was carried out by Bureau Veritas Testing and Inspection, Southerland Ridge according to the standards listed in Table 3-2.

Table 3-2: Standard methods for proximate and calorific analysis

Analysis	Standard
Sample Preparation	ISO 13909-4: 2001
Moisture Content	ISO 11722: 1999
Ash Content	ISO 1171: 2010
Volatile Matter Content	ISO 562: 2010
Gross Calorific Value	ISO 1928: 2009

3.3.3. Elemental analysis

3.3.3.1. X-Ray Florescence

XRF analysis of the fly ash samples was carried out by Bureau Veritas Testing and Inspection, Southerland Ridge according to ASTM standard D4326.

3.3.4. Mineralogical analysis

3.3.4.1. X-Ray Diffraction

XRD analysis was carried out by the Geology Department of the NWU, Potchefstroom Campus. An X'Pert Pro PANalytic (Philips) – Unit 2 diffractometer system was used to determine the concentrations of crystalline phases and amorphous materials in the ash sample. The Rietveld-based X'Pert PRO Highscore Plus Software was used to identify and quantify the crystalline phases and amorphous content of the ash sample. See Appendix B, Table B-2 for XRD instrument details and settings.

3.3.4.2. QEMSCAN

QEMSCAN analysis was carried out by Eskom RT&D, Rosherville, South Africa using a Zeiss Evo 50 SEM along with 4 light element Bruker Xflash Silicon Drift energy dispersive X-ray detectors. See Appendix B, Table B-3 for QEMSCAN instrument details and settings.

3.4. Results and Discussion

3.4.1. Particle Size distribution

The particle size distribution of the sampled ashes is illustrated in Figure 3-3. Ash sample PS B and PS C showed similar distributions, peaking at a particle size of ±90 µm. PS A showed a different trend with a higher percentage of particles in the 1.3 – 6.3 µm range and a slight reduction in the percentage of particles in the 12 µm – 100 µm range, peaking at a particle size of ±100 µm. The 10, 50 and 90% intercepts for the cumulative mass for ash samples PS A, B and C is shown in Table 3-3.

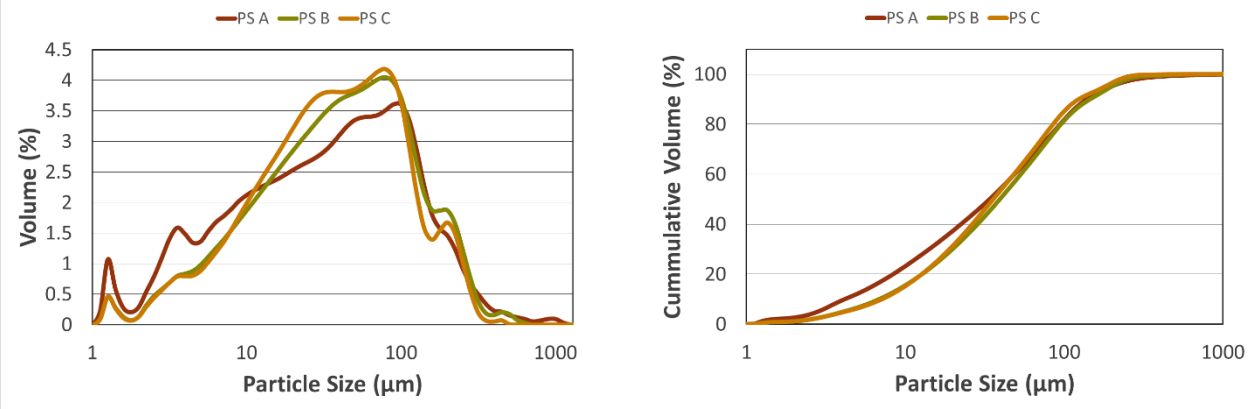


Figure 3-3: Fly ash particle size distribution

Table 3-3: 10%, 50% and 90% intercepts for the cumulative mass of ash samples PS A, B and C

Ash Sample	d(0.1) (µm)	d(0.5) (µm)	d(0.9) (µm)
PS A	4.7	13	155
PS B	7.7	44	163
PS C	8.0	40	138

PS A showed the highest concentration of fine particles with 10% of the cumulative volume consisting of particle sizes below 4.7 µm, while PS B showed the highest mean particle size (d(0.5)). The particle size distribution of all three ash samples showed the presence of course particles (> 150 µm), which according to Hower *et al*. (2017) often represents unburnt coal. The results obtained from the three sampled ashes were compared to historical Eskom data (Bosch, 1993, Bosch, 1995), and is shown in Figure 3-4. For PS A, the historical data showed a similar trend, with the three data sets showing some deviation

between 1 and 100 µm. These variations can be attributed to differences in feed coal characteristics and mill operation or performance.

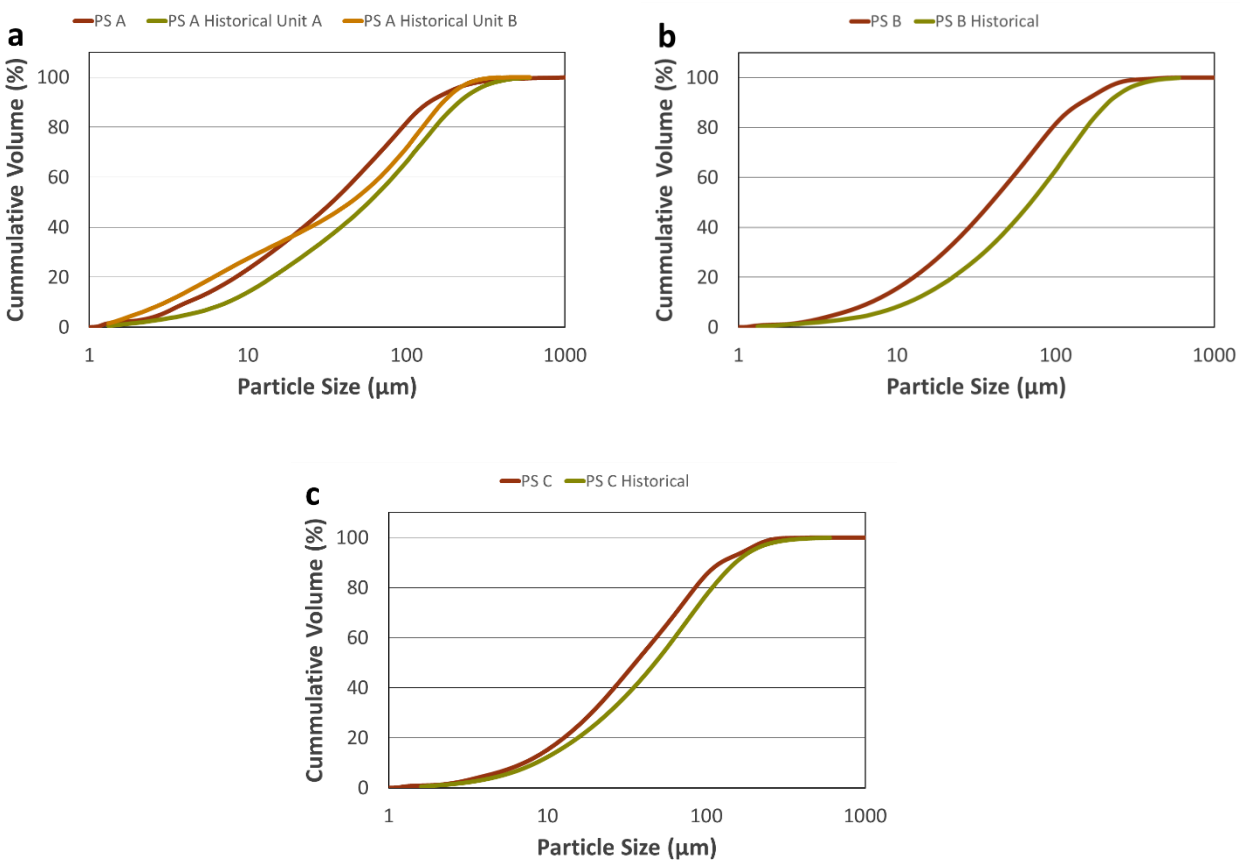


Figure 3-4: Comparison with previously sampled ash for PS A (a), PS B (b) and PS C (c) (Adapted from: Bosch, 1993, Bosch, 1995)

Variations were present for PS B with the newly sampled ash showing a larger concentration of fine particles. PS C also showed a deviation from historical data, with the historical data having a larger percentage of particles in the 40 to 90 µm range.

3.4.2. Proximate Analysis and Calorific Value

The proximate analysis and calorific values of the sampled ashes is shown in Table 3-4. See Appendix C for the original Proximate and Calorific report.

Table 3-4: Proximate analysis and calorific values of fly ash samples PS A, PS B and PS C (wt%)

Sample	PS A	PS B	PS C
Inherent Moisture	0.1	0.2	0.2
Volatile Matter	0.6	1.0	2.0
Fixed Carbon	0.0	0.1	1.1
Ash	99.3	98.7	96.7
Calorific Value (MJ/kg)	0.2	0.4	0.2

All ash samples showed ash values above 95%, with ash sample PS C showing the largest concentrations of both volatiles and fixed carbon. The observed calorific values were all below 0.5 MJ/kg, and did not show an inverse relation with the fixed carbon and volatile matter content.

3.4.3. Elemental analysis

3.4.3.1. X-Ray Florescence

The XRF results for the three ashes are shown in Table 3-5. See Appendix D for the original XRF report.

Table 3-5: Normalized XRF results of coal ash samples on a LOI-free Basis (wt%)

Sample	PS A	PS B	PS C
Al_2O_3	30.4	27.2	29.0
CaO	4.3	3.4	5.4
Fe_2O_3	3.6	6.5	5.5
K_2O	0.7	0.8	0.7
MgO	1.0	1.0	1.3
MnO	<0.01	0.1	0.1
Na_2O	0.4	<0.1	0.1
P_2O_5	0.3	0.4	0.4
SiO_2	57.2	58.5	55.3
TiO_2	1.5	1.3	1.6
SO_3	0.3	0.5	0.4

For comparison, some significant major and minor components (See Section 2.9, Table 2-2) were compared with a study conducted by Van Wyk (2015) and historical data compiled by Bosch (1993 & 1995). The comparison between the elemental composition obtained for this study and those of previous studies is shown in Table 3-6.

Table 3-6: Major elements comparison of coal ash samples (wt%)

Sample	**PS A**	**PS B**	**PS C**
	Al_2O_3		
This Study	30.4	27.2	29.0
Van Wyk	28.7	26.6	28.7
Bosch	35.1	20.6	25.4
	SiO_2		
This Study	57.2	58.5	55.3
Van Wyk	57.9	59.5	55.8
Bosch	53.5	66.9	57.1
	Al_2O_3 + SiO_2		
This Study	87.6	85.7	84.3
Van Wyk	86.6	86.1	84.5
Bosch	88.6	87.5	82.5

Table 3-7: Minor elements comparison of coal ash samples (wt%)

Sample	PS A	PS B	PS C
	Fe_2O_3		
This Study	3.6	6.5	5.5
Van Wyk	4.2	6.7	5.2
Bosch	3.6	6.3	5.3
	CaO		
This Study	4.3	3.4	5.4
Van Wyk	4.7	3.2	4.7
Bosch	4.4	2.7	5.7
	MgO		
This Study	1.00	1.0	1.3
Van Wyk	1.1	1.0	1.4
Bosch	1.3	1.0	2.1
	Na_2O		
This Study	0.4	<0.1	0.1
Van Wyk	0.4	0.2	0.4
Bosch	0.2	0.1	0.5

The major species showed some variations between the three sampled ashes, the study conducted by Van Wyk (2015) and the historical data (Bosch, 1993 &1995). The sum of alumina and silica, a common factor used to determine the suitability of FGC, proved more relatable, with values not varying by more than 3% between studies. Some variations were also present when considering the minor elements, most notably variations in the sodium concentration of PS B and PS C.

The elemental composition of the coal ash samples were also compared to typical North American and Indian ashes. The elemental concentrations of the sampled ashes, Indian ashes examined by Chandra (2013) and North American ashes examined by Bickelhaupt (1979) are shown in Table 3-8. Averaged values are listed for ashes that were sourced outside of South Africa.

Table 3-8: Comparison of averaged XRF result based on ash origin (wt%)

Ash Origin	PS A	PS B	PS C	India (avg.)	America (avg.)
Al_2O_3	30.4	27.2	29.0	29.8	22.8
CaO	4.3	3.4	5.4	2.1	8.2
Fe_2O_3	3.6	6.5	5.5	5.8	9.1
K_2O	0.7	0.8	0.7	0.9	1.9
MgO	4.3	3.4	5.4	0.6	2.7
MnO	<0.01	0.1	0.1	-	-
Na_2O	0.4	<0.1	0.1	0.1	1.4
P_2O_5	0.3	0.4	0.4	0.3	0.4
SiO_2	57.2	58.5	55.3	58.1	50.5
TiO_2	1.5	1.3	1.6	2.1	1.9
SO_3	0.3	0.5	0.4	0.3	1.6
LiO_2	-			-	<0.1

The ashes sampled for this study compare well with Indian ashes, with major components, such as Al and Si not varying by more than 9%. More importantly, similar amounts of species such as; Fe and Na where found, species commonly seen as noteworthy when considering the electrostatic properties of fly ash. When comparing the Fe and Na concentration of the ashes to American ashes, it was found that they differ greatly, with American ashes showing an order of magnitude larger Na concentrations when compared to the South African ashes. The American ashes, in general, showed lower quantities of major components and higher concentrations of Fe, Ca, Na, S, K and Li.

3.4.4. Mineralogical analysis

3.4.4.1. X-Ray Diffraction

The XRD results of the ash samples are shown in Table 3-9.

Table 3-9: Normalised XRD results of coal ash samples with amorphous content

Mineral	PS A + Amorphous	PS B + Amorphous	PS C + Amorphous
Mullite	29.7	28.6	27.9
Quartz	12.6	12.9	14.3
Silimanite	11.8	4.7	2.2
Hematite	0.7	5.0	3.7
Rutile	0.1	0.1	ND
Anatase	0.1	ND	ND
Anorthite	1.5	0.7	0.9
Cristobalite	0.1	0.1	0.1
Lime	0.2	0.2	0.4
Magnetite	0.4	0	0.7
Amorphous Content	42.8	47.6	49.9

ND - Not Detected

XRD analysis of the fly ash showed that quartz and mullite were the two most abundant minerals. Similar results were found by Eze *et al.* (2013) and Sighn and Kolay (2002) who considered ash samples that were combusted at high temperatures. Quartz is considered the primary constituent of fly ash and commonly found as pore and cell infilling in the organic matter of coal (Eze *et al.,* 2013; Ward, 2002). Mullite is the second most abundant constituent of fly ash and is believed to be formed from kaolinite by thermal decomposition. Lime is also present in small quantities in all three ash samples having been formed by the decomposition of calcite or dolomite (Eze *et al.,* 2013). Minerals such as mullite and lime are not commonly found in coal samples which have been subjected to low temperature ashing (LTA), with these minerals occurring in the form of kaolinite, calcite and dolomite (Eze *et al.,* 2013; Ward, 2002; Matjie *et al.,* 2011). Temperatures inside conventional PF furnaces exceed 1200°C, suggesting that minerals such as kaolinite, calcite and dolomite have

undergone thermal decomposition (Speight, 2013). Large amounts of glassy or amorphous components are also present in the fly ash sample. These are most likely formed during the combustion process where various components may melt and fuse, only partially crystallizing upon cooling (Matjie *et al.*, 2011).

3.4.4.2. QEMSCAN

The results of the QEMSCAN analysis of the ash samples are shown on Table 3-10.

Table 3-10: QEMSCAN analysis (vol%)

Mineral	PS A	PS B	PS C
Iron Oxides	1.3	2.8	3.2
Anhydrite	0	0.1	0.2
Ca Oxides	1.7	1.2	3.4
Ca Mg Oxides	0.1	0.2	0.5
Quartz	20.6	23.3	21.1
Aluminosilicate(Kaolinite)	36.2	37.5	31.6
Microcline	0.9	1.9	0.9
Muscovite/Illite	1.1	1.1	1.1
Anorthite	1.1	0.3	1.2
Glass: Aluminosilicate(Ca, Mg, Fe)	18.1	15.1	17.4
Glass: Silica(Ca, Mg, Fe)	3	5.2	3.1
Char: Vitrinite/RSF	1.3	1.1	1.4
Char: Fusinite	14.3	10.0	14.8
Other	0.2	0.1	0.1

Ash samples from PS B and PS C showed higher levels of iron oxides when compared to that of PS A. Iron oxides are formed during the combustion process when pyrite rich particles are combusted (Van Alphen, 2016). PS C also showed elevated levels of calcium/calcium magnesium oxides when compared to PS A and PS B. Like iron oxide, these oxides are formed during the combustion of cleat minerals present in coal (Van Alphen, 2016). The high temperatures present in the combustion zone of a PF boiler may cause certain minerals such as pyrite, calcite, dolomite and kaolinite to form molten slag

(Van Alphen, 2016). The molten slag droplets, upon cooling, typically form glassy, spherical ash particles known as cenospheres. Due to the non-crystalline nature of glass cenospheres they will not be detected by XRD analysis (Huggins, 2002). PS A and PS C showed higher levels of glass aluminosilicate cenospheres while PS B showed higher levels of glass silica cenospheres. PS A and PS C showed higher levels of unburnt carbon or char which are characterised by a notably high proportion of voids (Van Alphen, 2016). QEMSCAN results were converted from volume percentage to weight percentage. See Appendix F, Table F-2 for the applicable densities and Table F-3 for QEMSCAN results in wt%. See Appendix F for a pictorial representation of the minerals present in the fly ash samples. Also see Appendix G for a comparison between the elemental and mineral composition of the sampled ashes.

3.5. Summary

XRF analysis of the ash samples showed the highest contributing elements to be silica and alumina. Similar results were reported by Van Wyk (2015) and Bosch (1993 & 1995) for South African coal ashes. The XRF results were compared to Indian and American ashes and found to compare well with Indian ashes (Chandra, 2013) with components such Fe and Na appearing in similar concentrations. The XRF results did not compare well with American ashes which showed reduced concentrations of major components and higher concentrations of components such as Fe, Ca, Na, S, K and Li.

XRD analysis of the samples showed quartz and mullite to be the most abundant minerals. Similar results were found by Eze *et al*. (2013) and Sighn and Kolay (2002) who considered ash samples combusted at high temperatures. Quartz is considered the primary constituent of fly ash (Eze *et al.,* 2013; Ward, 2002) and mullite the second most abundant constituent of fly ash and is believed to be formed from kaolinite by thermal decomposition.

QEMSCAN analysis of the samples also showed quarts and kaolinite (mullite) to be the most abundant components. The QEMSCAN analysis also indicated the presence of cenospheres most likely caused by the high temperatures experienced by the ash in the furnace of a PF boiler. These cenospheres cannot be detected by XRD analysis and would be classified as amorphous content.

4. Experimental Methodology

In Chapter 4, the experimental setup and methodology used to determine the resistivity of the coal ashes is discussed. Due to the high resistivity values of fly ash and the need for accurate environmental control over a wide temperature range, conventional resistivity analysis methods, such as those described in Section 2.7.1 and Section 2.7.2 were not considered. Equipment, colloquially known as a resistivity oven, was used to determine the fly ash resistivity over a wide range of conditions. The resistivity oven was constructed by Eskom RT&D in 1994. The test facility was then decommissioned in 2012 and later donated to the NWU EPPEI research program in late 2014. The test apparatus received could then only be used to test fly ash resistivity at dry conditions. Consequently, the rig was retrofitted for climate moisture control, and recommissioned. The details of the experimental rig are described in Section 4.1 and includes the working and layout of the oven itself, the control panel and the humidifiers. The experimental procedure is explained in Section 4.2 and discusses the loading of the ash bowls, the humidifier start-up procedure and the process in which resistivity measurements are taken. In Section 4.3 the validity of the two test modes, ascending and descending, is discussed. This section also includes the testing and commissioning phases, used to test the accuracy of the resistivity oven.

4.1. Experimental Rig

The resistivity rig consists of numerous subsystems and has the ability to control the gas composition, moisture levels, temperature and voltage to which ash is subjected prior to current measurement. The resistivity oven was designed and constructed in accordance with IEEE standard 548 of 1984. The resistivity oven comprises of an environmental chamber, housed inside a temperature controlled oven, a control panel and two humidifiers.

The resistivity test cells, which contain the ash samples during testing, are situated inside the environmental chamber. The chamber comprises of a stainless steel plate on which a glass bowl is located to seal the chamber. Gas enters the chamber via the stainless steel plate after having passed through a heat exchanger located in the rear of the oven, next to the heating elements and convection fan.

The control panel comprises of several rotameters and controllers, responsible for regulating both the flow rates of the gases and controlling the temperature of the humidifiers, the oven

and the trace heating. The environmental gas is supplied to the control panel from gas cylinders. Once the gas has passed through the control panel it travels to the humidifiers. With the gas stream humidified, it enters the oven and flows to the environmental chamber via the heat exchanger.

4.1.1. Oven & Environmental Chamber

The environmental chamber is housed inside a Scientific Engineering CC oven. The environmental chamber consists of a stainless steel plate that has been recessed to seat an 18 litre glass bowl. The glass bowl, illustrated in Figure 4-1, reduces the environmental volume and seals the environment from the outside atmosphere.

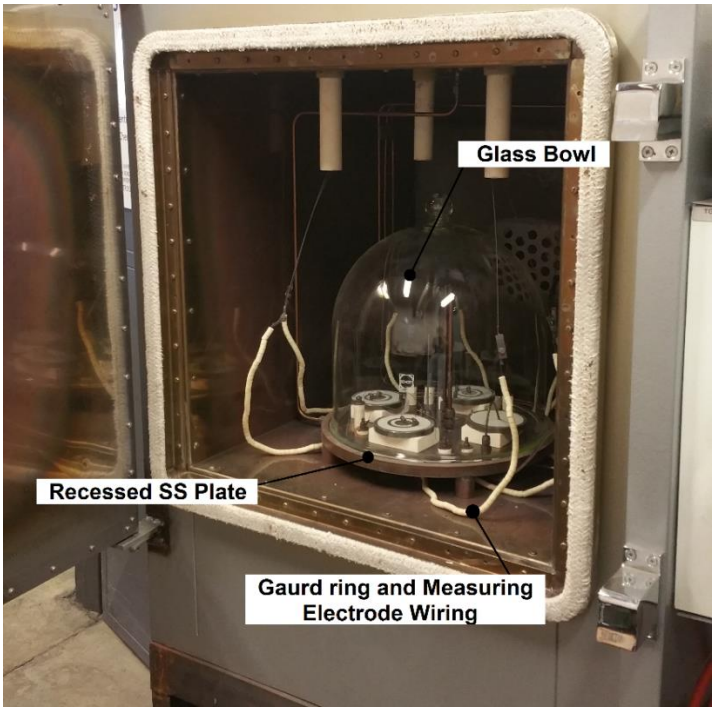


Figure 4-1: Oven and environmental chamber

The environmental chamber contains various thermocouples, gas inlets and outlets, electrical connectors and also houses the ash bowls, as illustrated in Figure 4-2. The three thermocouples housed inside the oven include the environmental gas thermocouple, the dummy ash bowl thermocouple and the oven control thermocouple. The environmental gas thermocouple measures the temperature of the air once it enters the glass bowl, while the

dummy ash bowl thermocouple is used to determine the temperature of the dummy ash bowl. It is assumed that the other three ash samples present in the bowls are at the same temperature as the dummy ash bowl. The oven control thermocouple is used for temperature control of the oven. This temperature is usually several degrees higher that the ash and environment temperature. The bowls, electrodes and guard rings are made of 304 grade stainless steel.

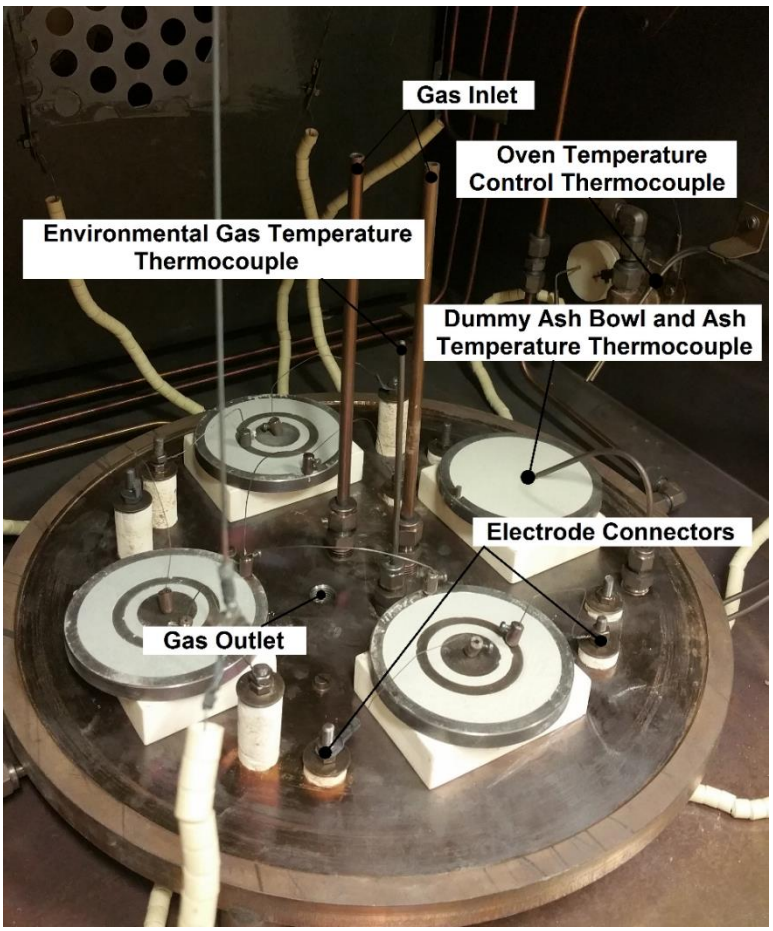


Figure 4-2: Environmental chamber inlet, outlet and connectors

The resistivity oven utilizes a high voltage direct-current power supply to impress a negative voltage on the test cells, also known as ash bowls. As illustrated in Figure 4-3, the ash bowls consist of a 5 mm deep stainless steel dish with the guard ring electrode and current-measuring electrode placed on the ash layer.

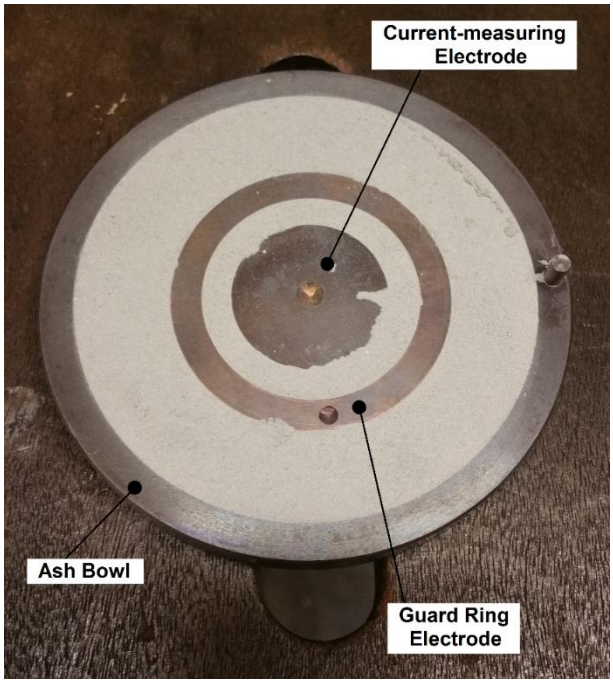


Figure 4-3: Ash bowls and electrode configuration

The voltage applied to the ash bowl creates a small current through the ash layer. The current induced by the high voltage power supply can then be measured between the current-measuring electrode and guard ring electrode, using a Keithley 486 picoammeter. With the applied voltage, induced current and test cell geometry known, the resistivity of the ash samples can be determined. To determine the temperature dependency of fly ash resistivity, the test procedure is carried out in a “round trip” technique, consisting of an ascending temperature phase, overnight purge followed by a descending temperature phase.

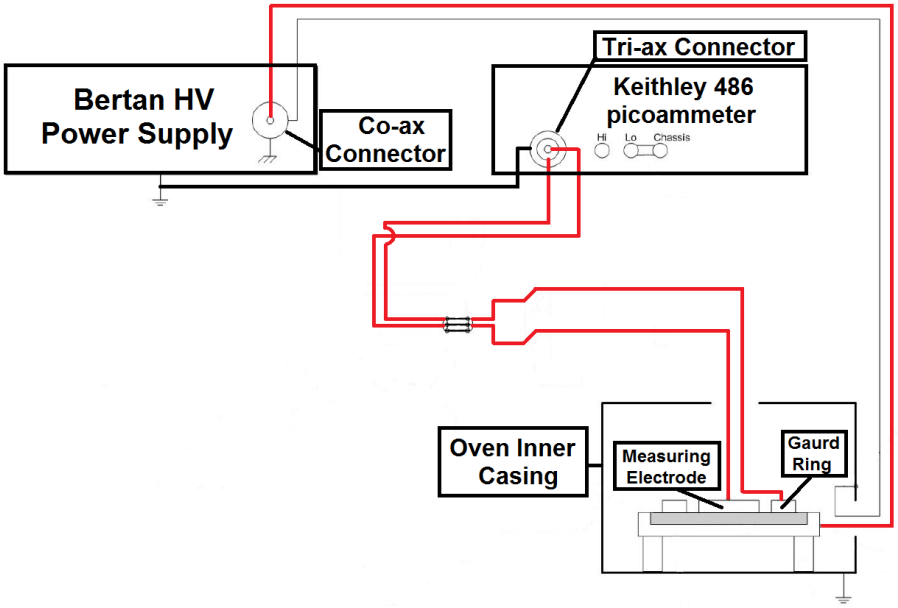


Figure 4-4: Resistivity oven wiring diagram

The wiring diagram of the various electrical components is shown in Figure 4-4. The current-measuring electrode and guard ring electrode wires enter the oven via the roof, as shown in Figure 4-1, and are connected to the bottom of the stainless steel plate. Ceramic sleeves and beads are used on all electrical wires connected to the stainless steel plate to avoid short circuits.

4.1.2. Control Panel

The control panel consist of the high voltage power supply, the picoammeter, several rotameters, temperature displays and controllers, as depicted in Figure 4-5. Coaxial wires are used to connect the current-measuring electrode and the guard ring electrode to the picoammeter. As the picoammeter is only able to measure one channel at any given time, the four incoming coaxial wires are connected to a four-way switch from which a single coaxial output is connected to the picoammeter.

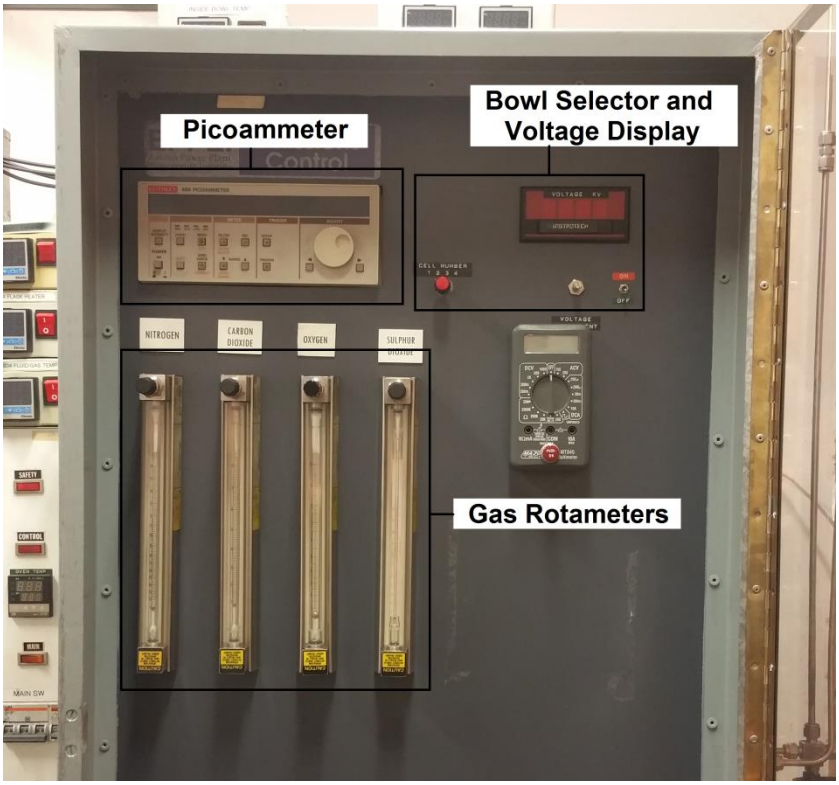


Figure 4-5: Resistivity oven control panel

The IEEE standards allow for the use of either dried air or simulated flue gas when measuring fly ash resistivity. For this study, dried air (Moisture < 10 vpm) is used for the ascending and descending phases and nitrogen (Purity > 99.999%) for the overnight purge. Both of these are supplied by gas cylinders fitted with regulators kept at 200 kPa. Dried air from the gas cylinder is routed through a rotameter and into a three-way valve. The three-way valve can either shut-off the gas supply, route the gas supply to the sampling port, which used to measure flow rate, or direct the flow towards the humidifiers. From the humidifier system, the gas enters a heated communal manifold. The nitrogen line is routed through a separate rotameter, passing through a shut-off valve and then onwards to the communal manifold. In Figure 4-6, the piping exiting the rotameters, the three-way sampling valve and nitrogen shut-off valve is shown.

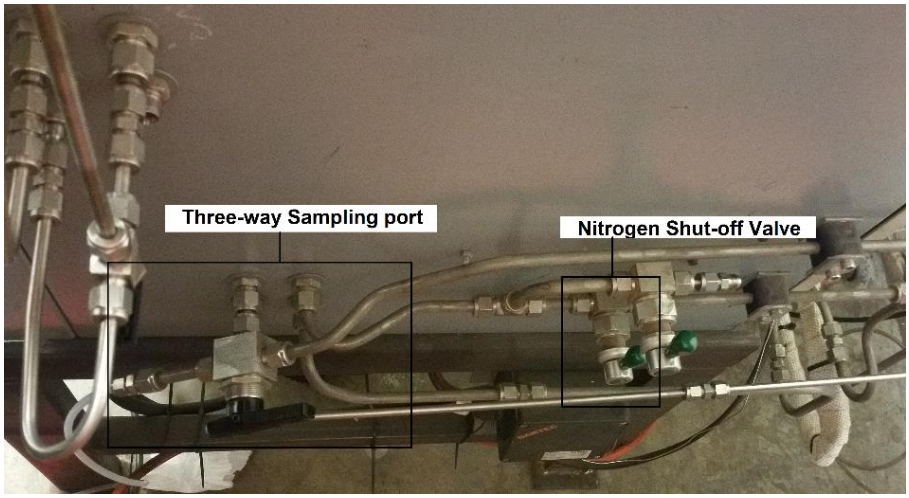


Figure 4-6: Flow sampling valve and nitrogen shut-off valve

The nitrogen shut-off valve is closed during the ascending and descending phase to ensure no air can escape from the communal manifold via the nitrogen line. The three-way sampling valve is used to measure the flow rate of dried air prior to humidification. The sampling port of the three-way valve is connected to a bubble flow meter.

4.1.3. Humidifiers

The humidifier system consists of two insulated Erlenmeyer flasks, connected in series as shown in Figure 4-7. The incoming gas from the three-way valve travels to the bottom of the primary humidifier, where it is bubbled through a micro-porous sintered glass stone, creating small bubbles for more effective gas saturation. The humidified air leaves the primary humidifier and enters the secondary flask where the process is repeated. The secondary humidifier is fitted with a thermocouple which is used for control purposes. Both flasks are placed in a stirred oil bath which is used to regulate the humidifier temperature. The pipes downstream the humidifiers are trace heated and kept at a temperature above the saturation temperature of the humidifiers.

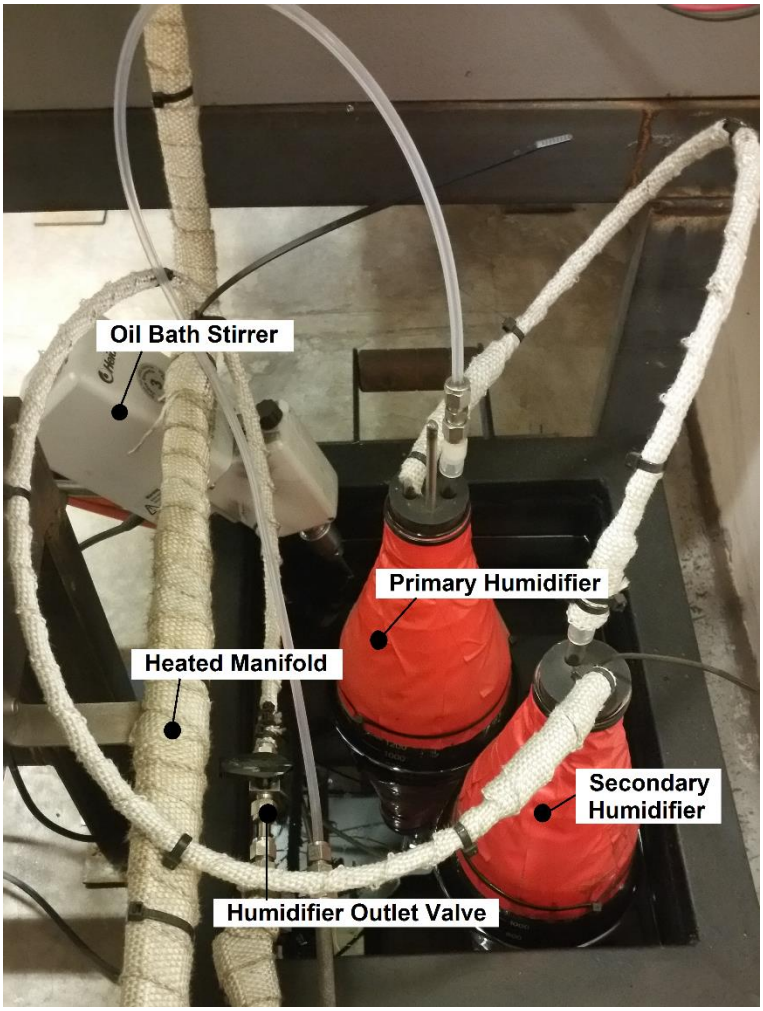


Figure 4-7: Humidifier system

The outlet from the secondary humidifier is fitted with a shut-off valve to ensure no nitrogen can escape the communal manifold via the humidifier system. The heated manifold is routed to the heat exchanger, passing through the oven casing as shown in Figure 4-8

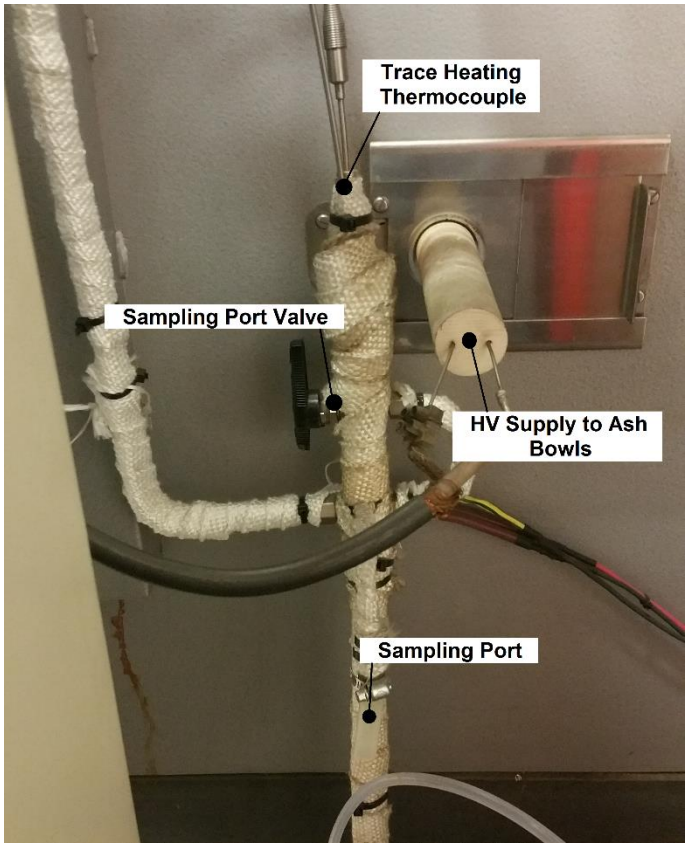


Figure 4-8: Humidifier sampling port

A sampling port is located downstream of the heated manifold and is used to test the moisture content of the air prior to entering the oven.

4.2. Experimental Procedure

4.2.1. Loading of Ash Bowls

Prior to ash loading, all ash bowls, sieves and other equipment are thoroughly cleaned. Once clean, the empty ash bowls are weighed and the mass recorded. As per IEEE standards a representative sample (50 – 60 g) of fly ash is sieved through an 180µm sieve to remove any foreign objects and larger pieces of unburnt char. This also allows for a flat measuring surface to seat the current-measuring electrode and guard ring electrode thoroughly. The sieved ash is then loaded into the ash bowl until the fly ash overflows the edge. The bottom of the bowl is subsequently tapped 10 times, with a strait metal edge, to allow the fly ash to settle. The remaining ash is then levelled with a straight metal edge. Following the ash loading procedure, both the current-measuring electrode and guard ring

electrode are gently placed onto the ash surface. Care is taken to ensure the current-measuring electrode and guard ring electrode are equally spaced. The measuring electrode and guard ring electrodes are now gently tapped with the straight metal edge to sink the electrodes into the ash layer. This yields an even ash layer with equally spaced electrodes, as shown in Figure 4-3. This process is repeated for each ash bowl, cleaning the sieve and accompanying equipment between each sample.

Once the bowls are filled and levelled, the bowl is weighed again and the weight recorded. The three loaded ash bowls are then placed in the environmental chamber. Each ash bowl is connected to the high voltage supply while the current-measuring electrode and guard ring electrode is connected to the picoammeter.

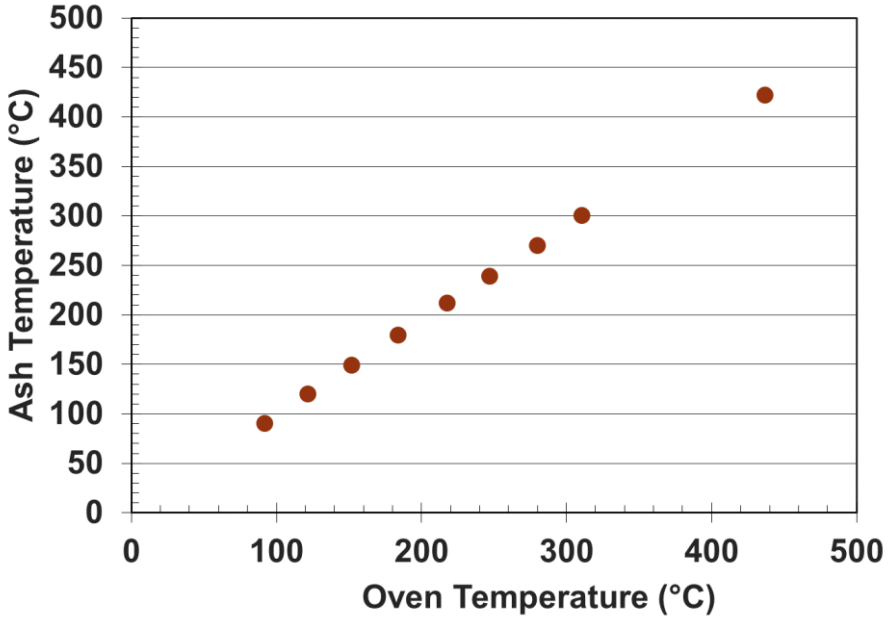


Figure 4-9: Fly Ash temperature as a function of oven temperature

A fourth dummy ash bowl, also filled with ash, is placed in the environmental chamber and a thermocouple positioned in the ash, to provide representative ash temperature readings. The correlation between oven temperature and fly ash temperature is given in Figure 4-9. Once all the ash bowls are connected to the electrical components, the environmental chamber is sealed using the glass bowl.

4.2.2. Humidifier Start-up and Testing

A day prior to resistivity analysis, the primary and secondary humidifiers are filled to the 1 litre mark. The three-way sampling valve and humidifier outlet valve is closed and the oil bath switched on without air flow, allowing the humidifiers to heat-up. On the day of testing, the valves are opened, the stirrer switched on and the air flow started. Upon starting the air flow to the humidifier, the oven is also switched on and set to 92°C. The picoammeter is switched on and given a minimum of two hours to warm up.

With the air flow initiated, the humidifier system is given a minimum of 2 hours' time to stabilize. Once the system is providing constant humidity levels, the gas flow rate is measured using a bubble flow meter. IEEE standards require 5 to 10 volume changes of the environmental chamber per hour. For this study, 6 volume changes per hour were kept at all times, which equates to 108 L/h at STP. Once all the subsystems are stable, the humidity levels in the air stream can be measured. A PVC column filled with silica is weighed and the mass recorded. The filled column is connected to the humidifier sampling port and left to collect moisture for approximately one hour. Once the hour has elapsed, the desiccate column is weighted again and the results recorded. With the weight difference, gas flow rate, gas temperature and pressure known, the moisture content is determined.

4.2.3. Resistivity Measurement

Once the moisture content of the gas stream is found to be within 5% of the desired humidity, the sampling port valve is closed and the flow directed to the environmental chamber. As per IEEE standards, time is given for the oven environment to achieve 99% dilution, occurring within 60 minutes when using 5 volume changes per hour.

With the humidifier delivering the correct moisture levels, the picoammeter having warmed up, the dummy ash bowl showing a constant ash temperature and the environmental chamber having achieved 99% dilution, the first current measurement can be taken.

4.2.3.1. Current Measuring Procedure

The picoammeter is set to “zero check” and given time for the reading to stabilize. If the reading is not zero or close to zero, a “zero correct” is done to cancel any internal offsets that might be present. With no voltage applied, the leakage current is firstly measured with 12 readings being taken of each ash bowl. The minimum and maximum of the 12 readings are eliminated and the remaining 10 readings averaged, to yield the average leakage current of the ash bowl (Keithley, 2000). The bowl selector switch is then turned to the next bowl and the process repeated for the remaining test cells.

The induced current is measured next. To measure the induced current of a test cell, a 2 kV negative high voltage is impressed on the cell. The voltage is applied for 60 seconds after which 12 current readings are recorded (Keithley, 2000). The minimum and maximum of the 12 readings are then eliminated and the remaining 10 readings averaged, to yield the average induced current of the cell. The next bowl is then selected and the process repeated for the remaining test cells. This concludes the first current measurement, after which the oven temperature is increased and the process repeated at the next temperature set point.

From the first current measurement at an ash temperature of 90°C, current readings are taken in 30°C intervals up to 310°C after which a final reading is taken at 370°C. This concludes the ascending phase of the “round trip” test program.

Air flow to the test environment is now switched off and the three-way sampling valve and humidifier outlet valve closed. The nitrogen shut-off valve is opened and nitrogen flow to the test environment is started. The ash samples are left overnight (16 hours) at 370°C. During the overnight purge the oil bath is left on.

Once the overnight purge is complete, the nitrogen shut-off valve is closed and the same start-up and testing procedure followed as described in Section 4.2.2. Once all requirements have been met, the descending phase is started. The descending phase current measurements are carried out in the same manner as the ascending phase current measurements, with the oven being switched off to allow for quicker cooling. Due to the rate at which the cooling of the environmental chamber takes place and the time required to measure each ash bowl, temperature differences occur between the individual bowls. As such the dummy ash temperature is recorded separately upon triggering the measuring event.

Once current measurements are complete the system can be switched off, the glass bowl removed and the ash bowls weighed once they have cooled down.

4.2.3.2. Calculation Methods

With the ash layer thickens, current-measuring electrode face area, applied voltage and measured current known, the ash resistivity can be calculated using Eq. 4-1.

$$\rho = \left(\frac{V}{I}\right)\left(\frac{A}{L}\right) \quad (4\text{-}1)$$

4.3. Experimental

Since this study is tailored to the power generation industry, the IEEE standard on moisture content was not followed. Instead representative moisture levels, in line with practical values in the flue gas of a power station, were chosen. In Table 4-1, moisture content for each power station from which ash samples were collected for the period of April 2013 to March 2014 (Keir, 2017) are shown.

Table 4-1: Moisture content of flue gas by volume for April 2013 to March 2014 at 6% O_2

	PS A	**PS B**	**PS C**
April 2013	6.57	6.16	5.50
March 2013	6.57	6.03	5.23
June 2013	6.64	5.99	5.27
July 2013	6.59	6.31	5.32
August 2013	6.29	6.24	5.23
September 2013	6.59	6.47	5.08
October 2013	6.38	6.24	4.90
November 2013	6.36	5.97	4.7
December 2013	6.77	6.68	5.02
January 2014	6.54	6.25	5.22
February 2014	6.72	6.14	5.38
March 2014	6.69	5.80	5.39

The values shown in Table 4-1 do not take into account any process variations such as boiler tube leaks. A moisture content of 6 vol% H_2O was chosen as the value that best suited the three power stations at the various times of the year. Two additional moisture contents were chosen to gauge the effect of moisture on resistivity, one below 6%, chosen as 4.6 vol% and another above, chosen as 9 vol%. Resistivity measurements were also conducted without moisture to serve as a baseline measurement.

The resistivity analysis was repeated twice at every moisture content to ensure repeatable results. Any results that showed a deviation larger than the allowed error ratio of 2 were carried out again, as per IEEE standards.

4.3.1. IEEE Round Trip Protocol - Ascending versus Descending Resistivity Results

When conducting resistivity analyses according to IEEE standards, current measurements are taken on both ascending and descending stages, commonly referred to as a "round trip". These measurements can sometimes vary and numerous sources have debated which of these two stages would yield resistivity results representative to ESP operation (IEEE std. 548, 1984).

Arguments can be made for both the ascending and descending results. It is speculated that inside an ESP unit, the freshly formed ash surface is attacked by acid and water vapour, commonly present in the flue gas stream, as the particle cools and is collected. This action can also continue in storage where the ash particle is exposed to moisture much greater than those found inside operating ESP units (IEEE std. 548, 1984). The fly ash layer can, however, be restored by "thermal annealing". At temperatures of 45°C or higher, the ash particle surface can be restored to its original condition. Hence, thermal annealing is the most common argument made for descending above ascending.

Under certain conditions, ashes can exhibit large amounts of residual combustibles or co-precipitated, thermally degradable compounds (IEEE std. 548, 1984). These species can have an effect on fly ash resistivity and their impact will be most noticeable on the ascending phase. If this is the case the ascending stage becomes more favourable as these components are likely to influence ESP operation. A further argument is made when resistivity analysis is carried out for the sole purpose of ESP sizing. For such a case, the IEEE standards recommend choosing the highest resistivity value at any given temperature.

This practise will negate the risk of an under designed ESP unit, with minimal risk of overdesign.

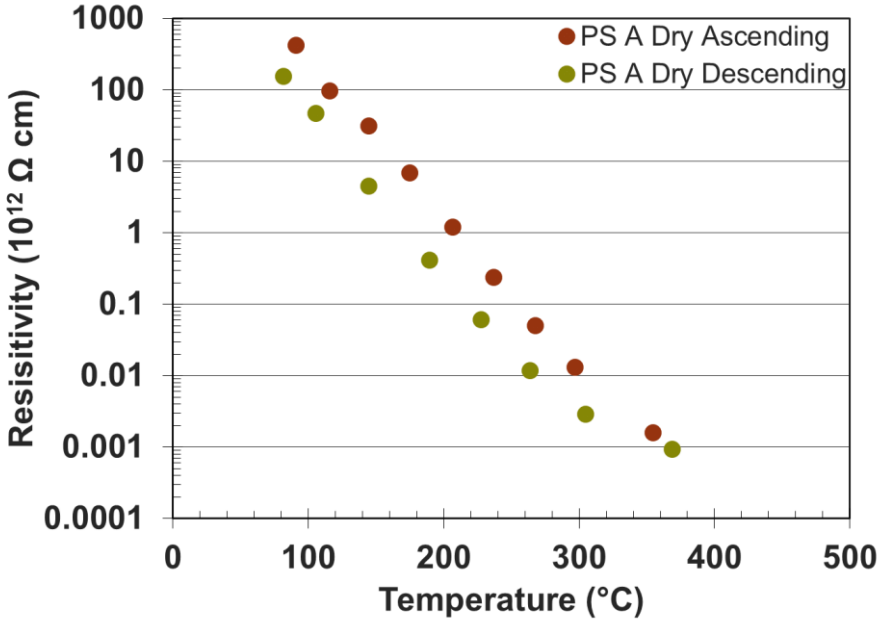


Figure 4-10: PS A ascending and descending resistivity as a function of temperature at dry ambient conditions

All ashes subjected to resistivity analysis for this study showed higher resistivity values on the ascending stage than those of the descending stage, as illustrated in Figure 4-10. This trend is present for both dry and humidified conditions. While ascending and descending measurements vary, they do not differ by more than one order of magnitude and are therefore satisfactory as per IEEE standards. For this study the ascending results were used since the resistivity values are more representative for industrial ESP operation and design (IEEE std. 548, 1984).

4.3.2. Oven Commissioning and Calibration

The commissioning of the resistivity oven consisted of three stages. For the first stage, all three bowls were loaded with an identical ash sample and the resistivity measured without any moisture. This was done to verify the cross-bowl repeatability, confirming whether the three bowls would yield similar resistivity measurements. Phase 2 included resistivity analysis with moisture introduced at 5.9 vol% for three different ash samples. The three ash

samples, PS X, Y and Z, were sampled from commercial South African coal fired power stations in 2014 and were previously tested for resistivity at the Southern Research Institute in Birmingham, Alabama (Van Wyk, 2015). Phase 2 was repeated three times, rotating the ash samples each time to gauge cross-bowl and within-laboratory repeatability simultaneously. Phase 3 was lastly carried out to verify the between-laboratory repeatability. The results from phase 2 were compared with those measured by Van Wyk (2015) at SRI in the USA. It should be noted the test carried out at the SRI were conducted at 6.2 wt. % while the results from phase 2 are at 5.9 vol%. The data will be assessed using an error ratio (Value 1 / Value 2). An error ratio of 2 is considered acceptable for within-laboratory repeatability while 2.7 is considered acceptable for between-laboratory repeatability (IEEE std. 548, 1984).

4.3.2.1. Cross-bowl Repeatability

The comparison of the three individual bowls loaded with an identical ash sample is shown in Figure 4-11.

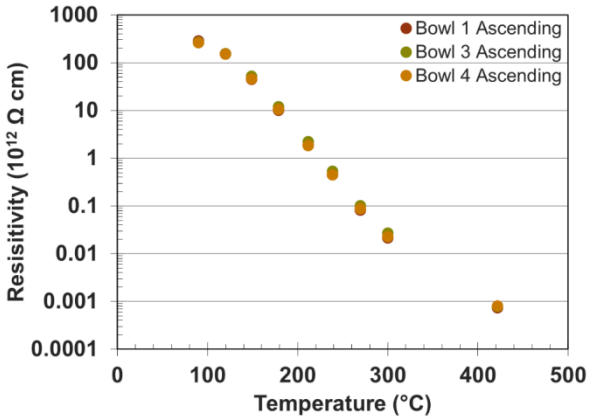


Figure 4-11: Commissioning - Phase 1 – cross-bowl repeatability at dry ambient conditions

The bowl showed acceptable repeatability, keeping well within the error ratio of 2 (higher or lower) required by the IEEE standards, as shown in Table 4-2.

Table 4-2: Cross-bowl error ratio (Relative to Bowl #1)

Cross-bowl Repeatability

Reading	1	2	3	4	5	6	7	8	9
Bowl #2	1.1	1.0	1.2	1.2	1.2	1.2	1.2	1.3	1.1
Bowl #3	1.1	1.0	1.0	1.1	1.0	1.0	1.1	1.1	1.1

4.3.2.2. Within-laboratory Repeatability

The within-laboratory repeatability of ash sample PS X, PS Y and PS Z is shown in Figure 4-12.

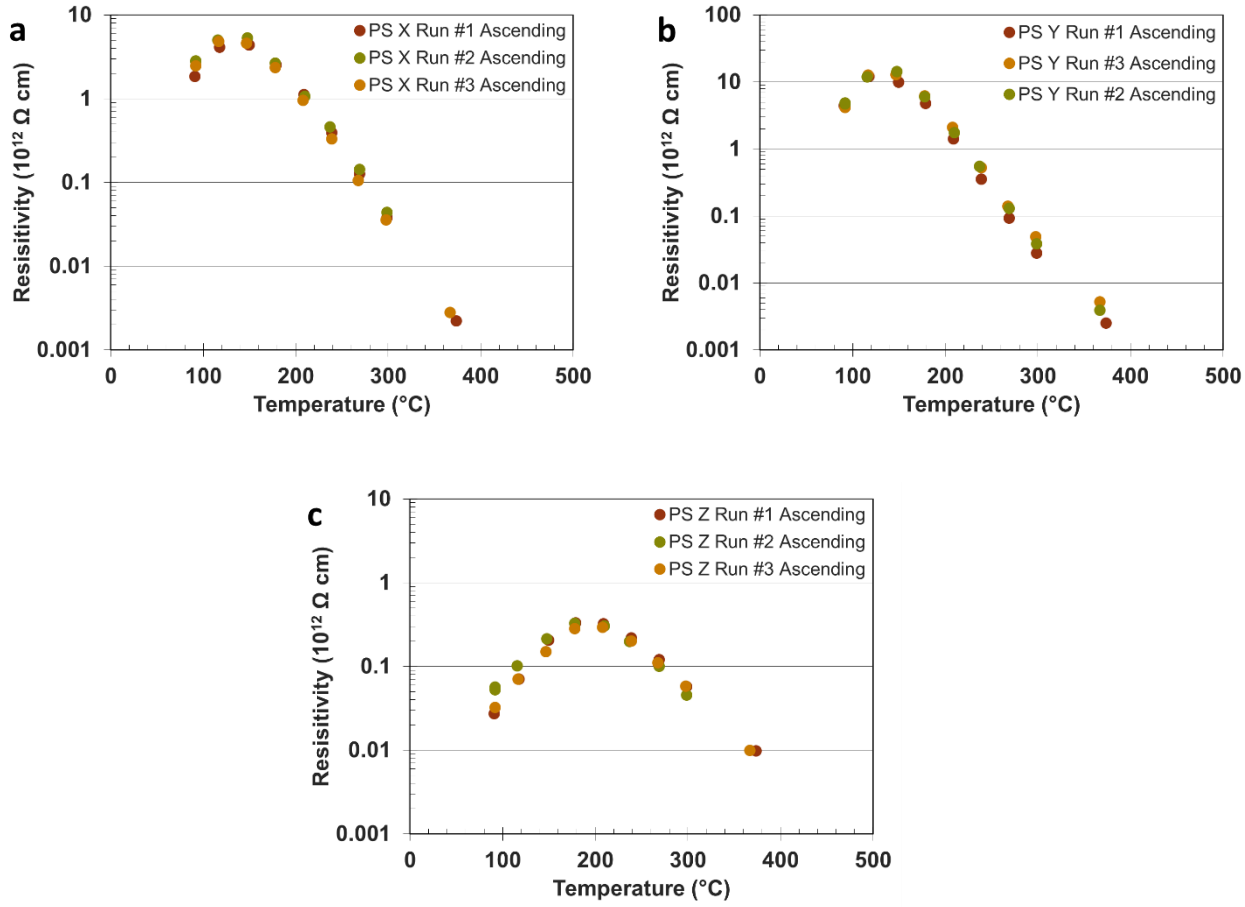


Figure 4-12: Commissioning Phase 2 – within-laboratory repeatability at 5.9 vol% ambient moisture for PS X (a), PS Y (b) and PS Z (c)

The error ratio of ash sample PS X kept within the error ratio of 2 (higher or lower) required by the IEEE standards, as shown in Table 4-3. Ash sample PS Y showed acceptable repeatability venturing outside the ratio of 2 once at high temperatures. Ash sample PS Z also showed acceptable repeatability venturing outside the ratio of 2 once at low temperatures.

Table 4-3: Within-laboratory error ratio

Within-laboratory Repeatability (Run #1 relative to Run #2)

Reading	**1**	**2**	**3**	**4**	**5**	**6**	**7**	**8**	**9**
PS X	1.5	1.2	1.2	1.1	1.1	1.2	1.1	1.2	1.7
PS Y	1.1	1.0	1.1	1.3	1.2	1.6	1.4	1.4	1.6
PS Z	2.1	1.4	1.0	1.0	1.1	1.1	1.2	1.3	1.4

Within-laboratory Repeatability (Run #1 relative to Run #3)

Reading	**1**	**2**	**3**	**4**	**5**	**6**	**7**	**8**	**9**
PS X	1.3	1.2	1.1	1.1	1.2	1.2	1.2	1.1	1.3
PS Y	1.1	1.0	1.3	1.3	1.5	1.5	1.5	1.8	2.1
PS Z	1.2	1.0	1.4	1.2	1.1	1.1	1.1	1.0	1.0

4.3.2.3. Between-laboratory Repeatability

The result of the between-laboratory test for sample PS X, PS Y and PS Z is illustrated in Figure 4-13. The figure shows both the upper and lower limit (2.7 ratio) of the tests conducted by SRI, the SRI measured resistivity values and the results from phase 2. For PS X, the results measured during phase 2 of commissioning compared well with the SRI measurements. The trend seen in both resistivity versus temperature graphs are similar and showed no measurements that fell outside the 2.7 ratio.

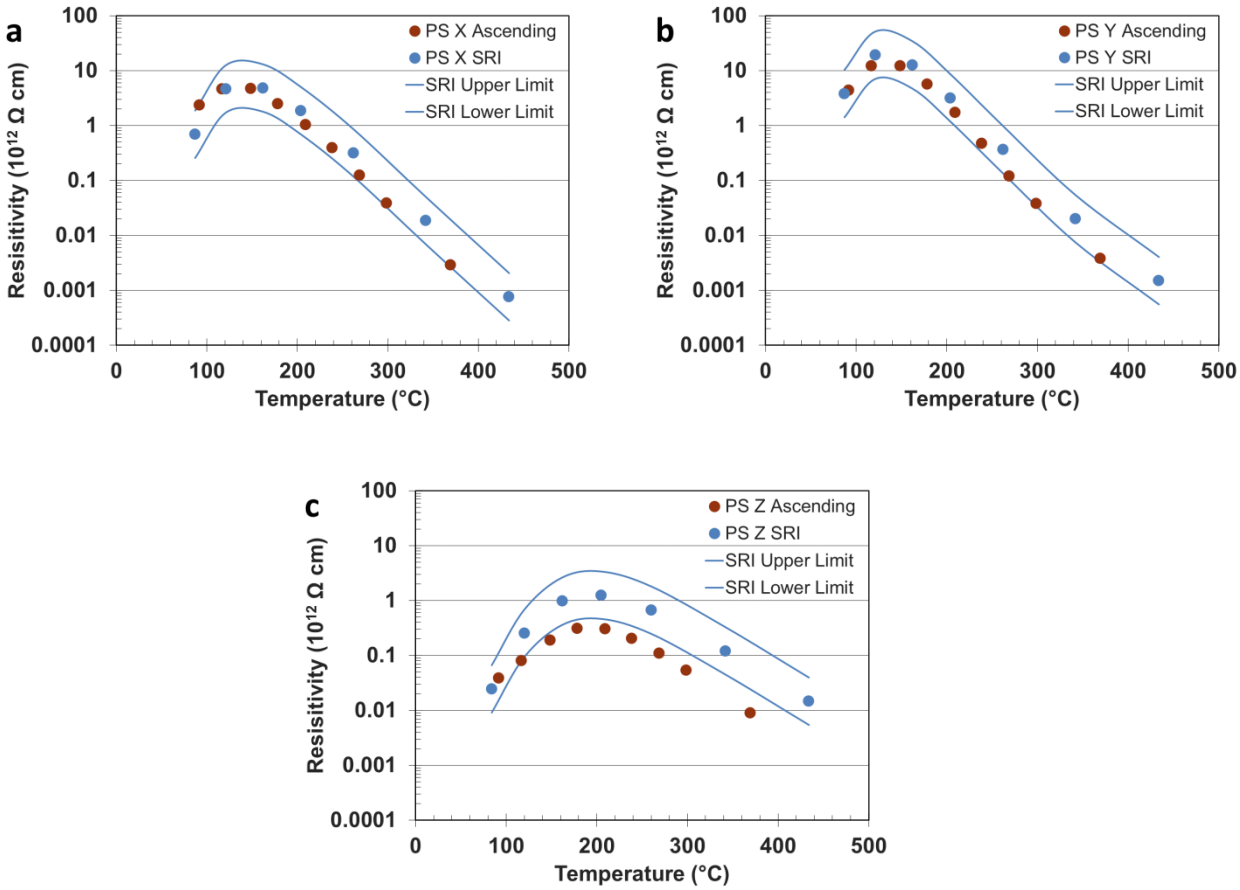


Figure 4-13: Commissioning Phase 3 – Between-laboratory repeatability for PS X (a), PS Y (b) and PS Z (c)

For PS Y both graphs showed a similar trend with the measurements taken during phase 2, keeping within the allowed 2.7 ratio. The graphs of PS Z showed a similar trend to SRI, however, several measurements taken during phase 2 fell outside the allowed 2.7 ratio.

4.3.2.4. Critical evaluation of Commissioning

A difference in resistivity values was observed between the ascending and descending measurements, with the descending stage showing higher resistivity across the entire temperature range. The difference between ascending and descending is most dominant in the surface resistivity range, indicating that some moisture, volatiles or unburnt char might be present. Said species became irrelevant as the electron transfer mechanism transitioned to volume resistivity. It is hypothesised by Van Wyk (2015) that during the ascending phase and the 16 hour overnight purge, the moisture and volatile species is driven off, causing a

resistivity increase in the surface resistivity region on the descending stage. IEEE standards stipulate that any sample that shows more than 1 order of magnitude difference between ascending and descending phase should be treated as suspect and subsequently resampled and retested. A comparison of the ascending and descending measurements for PS Z is shown in Figure 4-14 for both the EPPEI and SRI resistivity ovens. Both show an order of magnitude or more difference between ascending and descending resistivity values.

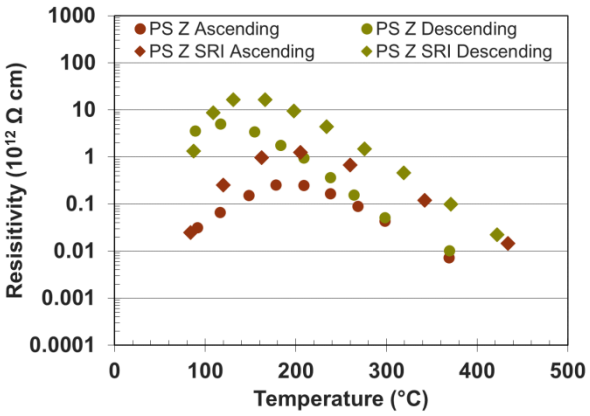


Figure 4-14: PS Z resistivity comparison with SRI resistivity for the ascending and descending stages

While several key differences could be found between the methods used in this study and those used by SRI, the most likely to cause discrepancies, is the difference in sieve size. Ash samples are sieved to remove foreign object before they are loaded in the ash bowls. The IEEE standards stipulate that an 80 mesh (177 µm) sieve is to be used before loading. All ash samples were passed through a 180µm sieve before loading, while SRI used a 60 mesh (250µm) sieve for all ash samples. It is known that particle size is an important physical parameter effecting resistivity of fly ash (McLean, 1976). Finer ash particles allow for greater surface area, increasing electron transfer both across the surface and through the volume of the ash particles. This, in turn, effectively reduces the resistivity across the entire temperature range (McLean, 1976). The difference in particle size could explain why the resistivity from phase 2, generally proved lower that those found by SRI in the USA.

The resistivity oven used in this study proved very capable at replicating within-laboratory results, staying within the error ratio of 2. Between-laboratory repeatability proved acceptable, staying within the 2.7 error ratio for two of the three ashes analysed. The resistivity oven generally recorded a lower resistivity reading, which might in part, be due to the differences in particle size.

5. Results and Discussion

In Chapter 5, the results of experimental resistivity determination and the accuracy of the Bickelhaupt model when applied to South African coal ashes are discussed. In Section 5.1, resistivity results for 0, 4.6, 6.0 and 9.0 vol% ambient moisture are presented and compared to literature. In section 5.2, the experimental data will be modelled using readily available models from literature. Modelled data will be assessed using an error or deviation ratio; of which 2 is considered acceptable for within-laboratory repeatability while 2.7 is considered acceptable for between-laboratory repeatability (IEEE std. 548, 1984). Finally, in Section 5.3, the conventional models will be modified to account for the unique nature of the South African coal ashes in an attempt to improve on the accuracy of the predictive techniques.

5.1. Resistivity Measurement

5.1.1. Resistivity Results for Dry Ambient Conditions

The resistivity measurements of the sampled ashes, under dry ambient conditions for the ascending stage, are illustrated in Figure 5-1. Ash sample PS A showed the lowest resistivity over the majority of the temperature range, while PS B showed the highest resistivity in the low temperature region. PS B and PS C showed similar resistivity values in the volume resistivity range, which is at higher temperature. The decreased resistivity shown by PS A can be attributed to the increased amount of sodium found in the ash, as shown in Table 3-5. Sodium is a known resistivity reducing species, facilitating the transfer of electrons through the ash layer, thereby, reducing the resistivity (Bickelhaupt, 1975; Qi and Yaun, 2013).

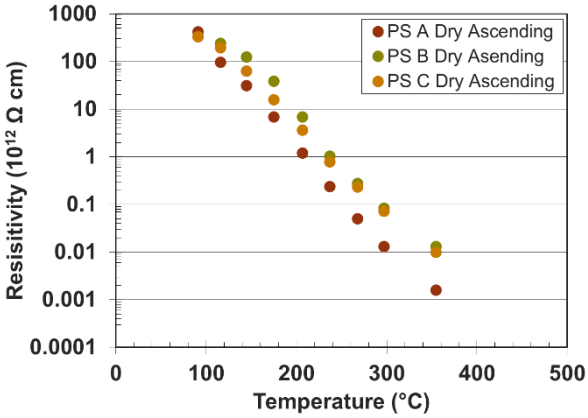


Figure 5-1: Resistivity as a function of temperature for dry ambient conditions

With dry ash, the only active electron transfer mechanism is volume resistivity. Volume resistivity is commonly considered to have a linear relation between the log of resistivity and temperature, as shown by Figure 2-4 between 250 and 450°C (Bickelhaupt, 1979). As moisture or other chemical substances are introduced, surface resistivity becomes an active electron transfer mechanism in the lower temperature range. PS A and PS C exhibits this linear relation between the log of resistivity and temperature, while ash sample PS B showed a slight departure from linearity in the surface resistivity region. The trend exhibited by PS B is reminiscent of a humidified resistivity curve, showing a slight arc in the temperature range of 90 to 180°C. This arc is however not as pronounced as an ash sample exposed to elevated moisture levels, such as those shown in Figure 2-14. The departure from linearity might be due to the presence of certain chemical species that were not removed by drying, facilitating the transfer of electrons along the surface of the particle. It is unlikely that this deviation is due to moisture as the sample was extensively dried before testing. One possibility for this occurrence is the presence of co-precipitated volatile species, which can influence the resistivity in the temperature range of 90 to 180°C (IEEE std. 548, 1984).

5.1.2. Resistivity Results for Humidified Ambient Conditions

The effect of ambient moisture on the resistivity of the fly ash samples is illustrated in Figure 5-2. The trends exhibited by the ash samples are similar. Samples tested under dry ambient conditions showed the highest resistivity values, with the resistivity decreasing as the temperature increases. When moisture was applied to the samples, a decrease in resistivity was observed at temperatures below 200°C. The decrease in resistivity became

more pronounced as the amount of ambient moisture was increased. As the temperature increased, the effect of moisture became less pronounced, becoming insignificant at temperatures above 250°C, where the resistivity values approached those of dry conditions. When ambient moisture is introduced, the resistivity tends to decline in the surface resistivity region, 90 to 180°C. The reduction in surface resistivity is generally attributed to the formation of a thin, conducting moisture layer along the surface of the particle, accelerating the transfer of electrons (Shanthakumar *et al*., 2008a).

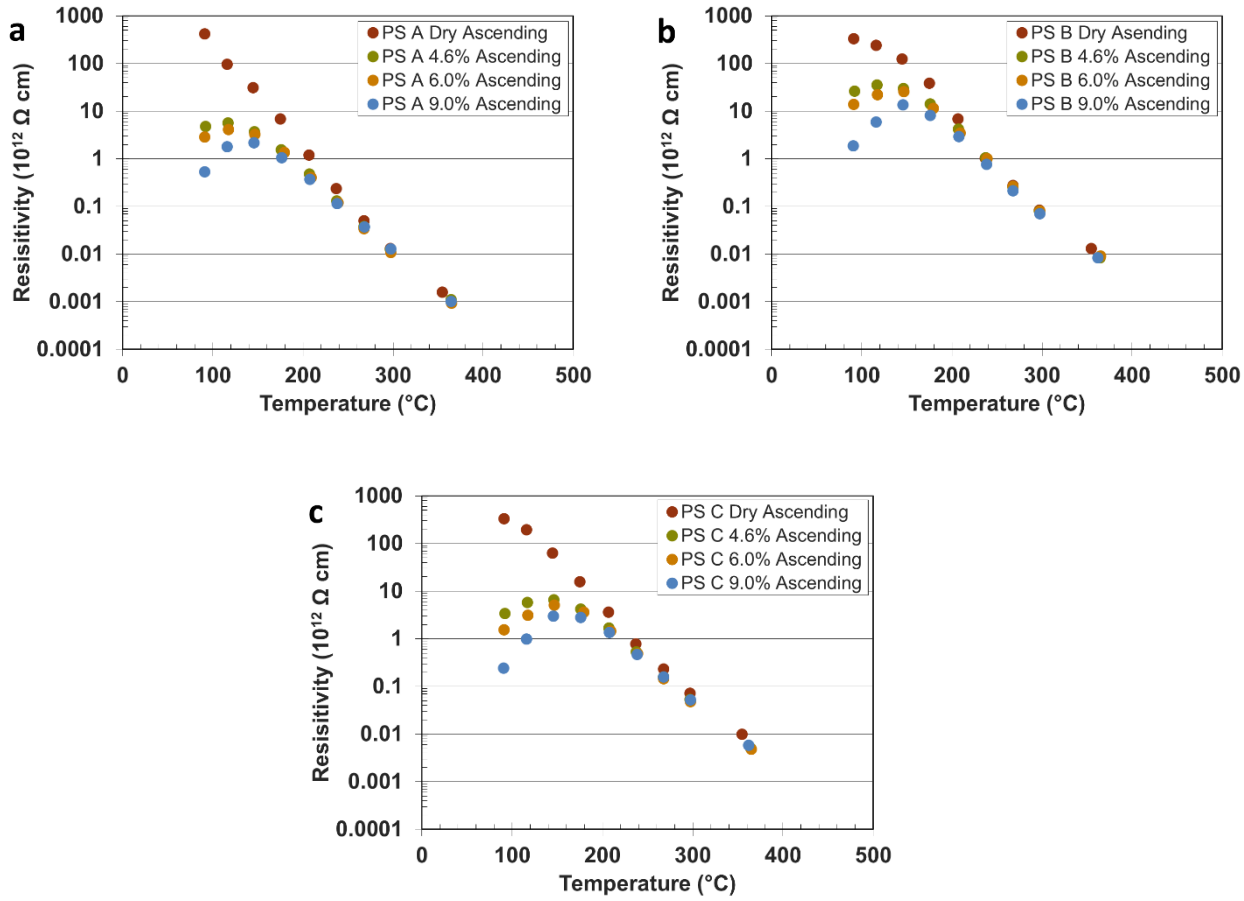


Figure 5-2: Resistivity as a function of temperature and ambient moisture for PS A (a), PS B (b) and PS C (c)

The effect of moisture is only present in the surface resistivity range. As the temperature increases beyond 180°C the electrons progressively starts transferring via the volume of the ash particles rather than the surface. The effect of moisture is more pronounced on ash samples PS A and C than that of PS B, as indicated by Table 5-1 where the reduction of resistivity compared to dry ambient conditions at 150°C is shown. Ash sample PS B was

shown to be less effected, while ash samples PS A & PS C showed a similar reduction in resistivity.

Table 5-1: Percentage resistivity reduction relative to dry ambient conditions at 150°C (vol%)

	Percentage Reduction in Resistivity		
Ambient Moisture (vol%)	PS A	PS B	PS C
4.6	88%	76%	90%
6.0	90%	80%	92%
9.0	93%	89%	95%

The fly ash resistivity as a function of temperature for the three samples is compared in Figure 5-3 at an ambient moisture content of 9 vol%. Ash sample PS B showed the highest resistivity values over the entire temperature range, peaking at 1.1 $\times 10^{13}$ Ω cm at a temperature of approximately 150°C. Ash samples PS A and C also peaked around this temperature, but lower resistivities values of 1.7 $\times 10^{12}$ and 2.4 $\times 10^{12}$ Ω cm, respectively, were observed.

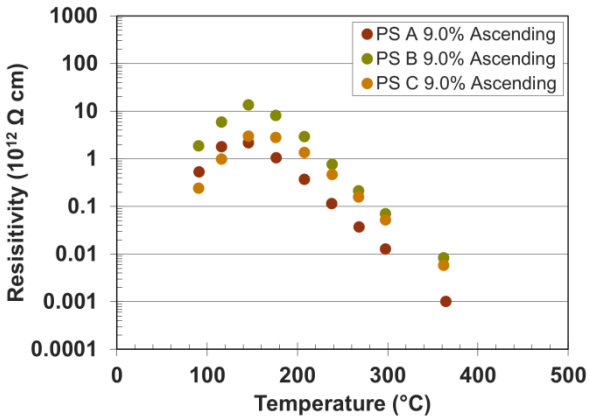


Figure 5-3: Resistivity as a function of temperature at an ambient moisture content of 9.0 vol%

The trend illustrated in Figure 5-3 can also be seen in previous studies conducted on American and Indian ashes when considering a moisture content of 9.0 vol%. The American ashes analysed by Bickelhaupt (1979) peaked at 144 - 182°C, however, these ashes generally exhibited lower resistivity values. The ashes analysed by Bickelhaupt seldom showed resistivity values exceeding 1 $\times 10^{12}$ Ω cm, with the highest recorded resistivity value

being 5.3 $\times 10^{12}$ Ω cm. The resistivity obtained from Indian ashes, analysed by Chandra *et al.* (2006) were more comparable to South African ashes, with the maximum resistivity of ashes ranging from 4.5 $\times 10^{12}$ to 3.4 $\times 10^{13}$ Ω cm at 150°C.

The ashes analysed by Bickelhaupt (1979) showed high concentrations of lithium, sodium and iron compounds. These ash components are known to reduce both surface and volume resistivity, as shown in Table 2-2. The concentration of these resistivity reducing elements are generally higher in American ashes, with South African and Indian ashes having lower concentrations of these components, which in turn, leads to increased resistivity values across the entire temperature range.

5.2. Comparison with the Bickelhaupt Model

The predictive method developed by Bickelhaupt (1979) is the most general case of ash resistivity prediction. In this model, only the chemical properties of coal ash are considered while physical properties are not taken into account (Bickelhaupt, 1979). For the development of the model, both industrial coal fired ashes and synthetically prepared ashes were used, where the laboratory ashing procedure resulted in similar ash than the industrially collected ash. The proposed model can also be expanded to accommodate flue gas conditioning agents such as sulphur trioxide and water. Furthermore, the predictive technique only considered American coal ashes, from both the eastern and western seaboard (Bickelhaupt, 1975). The Bickelhaupt model was used and the results compared with experimental resistivity data to gauge the effectiveness of the model on South African ashes. A detailed description of the Bickelhaupt model is given in Appendix H using ash sample PS A as example.

The difference between experimentally obtained resistivity values and resistivity values predicted with the standard Bickelhaupt model is depicted in Figure 5-4. From the figure it is apparent that the Bickelhaupt model predicts the trends of the resistivity values reasonably well, but large absolute deviations were observed.

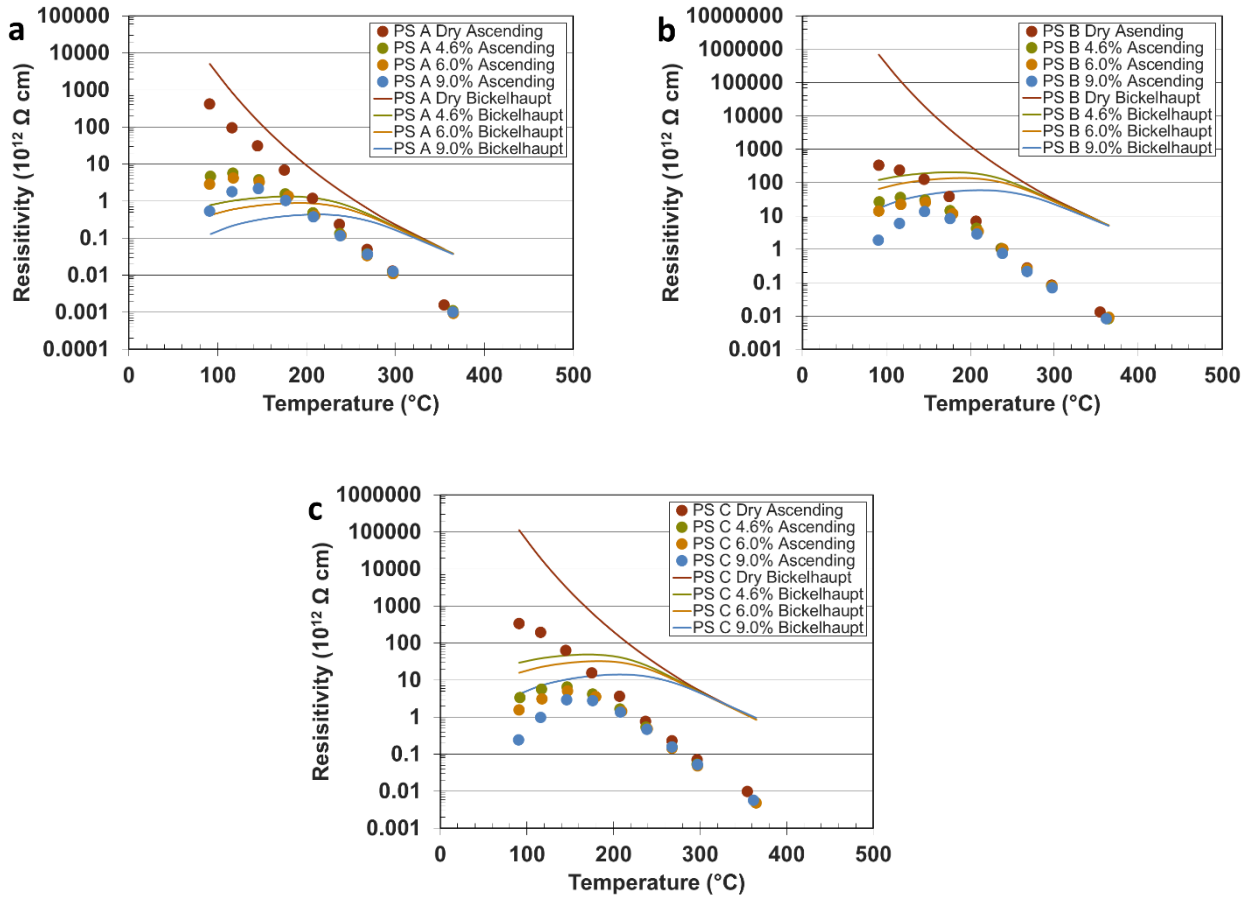


Figure 5-4: Experimental and Bickelhaupt resistivity as a function of temperature and ambient moisture for PS A (a), PS B (b) and PS C (c)

The Bickelhaupt model yielded large deviations when applied to ash samples PS B and C, with PS A generally showing the smallest deviation, as shown in Table 5-2. The large discrepancy between predicted and experimental resistivity values can be attributed to differences in ash composition, with the Bickelhaupt model being developed solely from North American ashes. Of the three sampled ashes, PS A showed an elemental composition most similar to those of American ashes and as a result yielded the most accurate prediction. The standard Bickelhaupt model showed the largest deviations when applied to ash sample PS B. This ash sample showed the lowest concentration of sodium, the principle charge carrier which resulted in deviation ratios as large as 600 at 400°C. Ash sample PS C also showed a low sodium concentration and as a result, large differences between predicted and experimental values were observed.

Table 5-2: Error ratios of standard Bickelhaupt model at 120°C, 270°C and averaged for dry, 4.6, 6.0 and 9.0 vol% ambient moisture

Ambient Moisture (vol%)	PS A	PS B	PS C
120°C			
Dry	9.1	500	100
4.6	1.8	27	39
6.0	6.8	4.3	7.4
9.0	25.6	1.2	1.3
270°C			
Dry	13	320	63
4.6	12.6	310	74
6.0	12.1	225	75
9.0	7.9	160	56
Average (90 - 400°C)			
Dry	12.1	501.2	56.9
4.6	9.5	193.8	39.8
6.0	11.0	147.5	45.8
9.0	15.4	128.1	47.5

In general, it can be seen that the resistivity at dry ambient conditions is overestimated by the standard Bickelhaupt model over the entire temperature range, and that the effect of ambient moisture on surface resistivity is also underestimated. This suggests that this predictive method is not applicable to South African ashes, and that the various parameters associated with the model may need to be reconsidered to describe the ash resistivity of South African derived coal ashes more accurately.

In conclusion, the Bickelhaupt model proved inaccurate at predicating resistivity values of the three sampled ashes. The inability of the Bickelhaupt model to predict South African and other ashes with similar compositions, such as Indian ashes, has been previously reported in literature (Chandra, 2008; Van Wyk, 2015).

5.3. Bickelhaupt Correction

5.3.1. Modelling Approach

In an attempt to develop a predictive model to more accurately describe the resistivity of South African fly ashes, modifications were proposed to the Bickelhaupt model. A strategy was followed that first considered modifications in the temperature region dominated by volume resistivity (200 - 400°C), which is presented in Section 5.3.2. The original volume resistivity term as proposed by Bickelhaupt describes the (log of) volume resistivity as a function of temperature and uses as input the chemical properties of the coal ash. The volume resistivity term makes use of several constants, determined from the experimental data of North American coal ashes, to describe how species such as Na, Fe, Mg and Ca influence the volume resistivity. Alterations were made to these constant to better describe the unique chemical nature of South African ashes. Corrections to the volume resistivity constants were proposed such that the deviation between the predicted values and experimental values was minimised by altering the five volume resistivity constants, as given in Eq. 5.1, according to the least square method.

The alterations to the volume resistivity term of the Bickelhaupt model proved effective in reducing the deviations between predicted and experimental values in the volume resistivity region. However, large deviations were still present in the surface resistivity region and as a result, modifications were made to the surface resistivity term of the Bickelhaupt model, and these are presented in Section 5.3.3. The Bickelhaupt model describes the (log of) surface resistivity as a function of temperature and requires as input the ambient moisture concentration and the elemental concentration of sodium. Once again, the surface resistivity term of the standard Bickelhaupt model uses constants to describe how sodium influences the resistivity, as given in Eq. 5.2. Alterations were made to the constants to better describe how the resistivity of South African ashes is influenced by sodium in the surface resistivity region. Corrections to the surface resistivity constants were again performed by minimizing the error between the predicted values and experimental values by altering the two surface resistivity constants, using the least square method. The altered surface and volume resistivity terms were applied and the determined resistivity values compared with experimental results at 0, 4.6, 6.0 and 9.0 vol% ambient moisture. In Appendix I, a detailed description of the alterations made to the Bickelhaupt model is given.

5.3.2. Volume Corrected Bickelhaupt Correlation

The modifications to the volume resistivity term of the Bickelhaupt model are displayed in Figure 5-5. The figure depict the experimental dry resistivity of the sampled ashes, the volume resistivity predicted by the standard Bickelhaupt model and the volume resistivity predicted by the modified Bickelhaupt model.

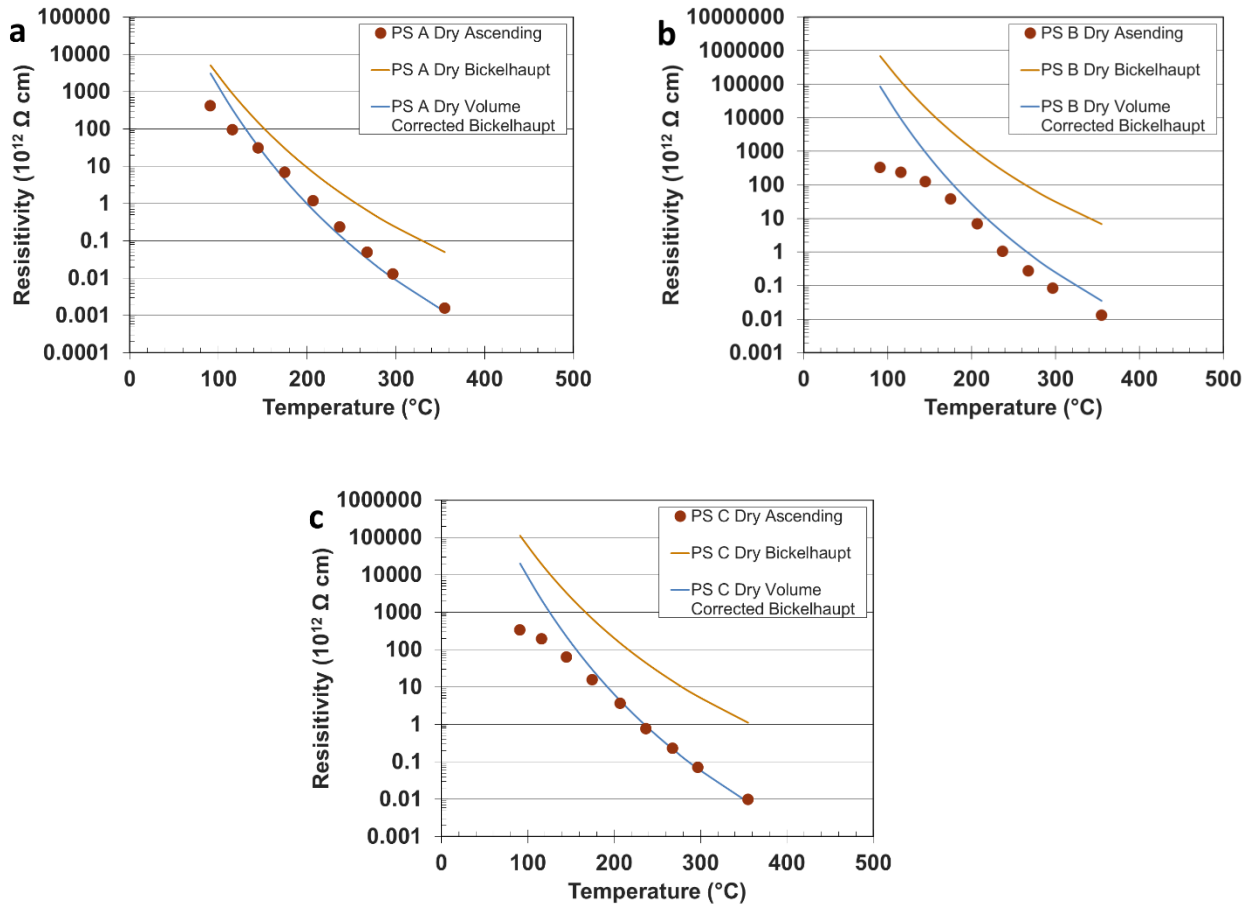


Figure 5-5: Experimental, Bickelhaupt and volume corrected Bickelhaupt resistivity as a function of temperature at dry ambient conditions for PS A (a), PS B (b) and PS C (c)

The changes made to the Bickelhaupt model significantly improved the accuracy with which the model can describe the volume resistivity of South African ashes. The modified volume resistivity term, represented by Eq. 5-1 and Table 5-3, better describes how elements such as sodium, magnesium, iron and calcium influence the resistivity of South African fly ashes.

$$\log \rho_{v,\ 352^{\circ}C} = A_v - (B_v \log x) - (C_v \log y) + \left(D_v\ (\log z - \log E_v)\right) \qquad (5\text{-}1)$$

Table 5-3: Volume corrected Bickelhaupt constants

Bickelhaupt Constant	Original Value	Modified Value
A_V	8.9434	8.3771
B_V	1.8916	1.2327
C_V	0.9696	1.2160
D_V	1.2370	0.6908
E_V	2.5	2.5974

The deviations of the volume corrected Bickelhaupt model is shown in Table 5-4 for dry ambient conditions. The volume corrected model best described the resistivity of ash sample PS A, having the lowest deviations across the entire temperature range, 90 - 400°C. The error ratios of PS A in the volume resistivity range did not exceed 1.8, within the error ratio of 2.0 allowed by IEEE standard 548 for within-laboratory repeatability. Modifications to the volume resistivity term proved less effective on ash sample PS B, with the ash with the lowest sodium concentration still showing the largest deviation between experimental and predicted values. The deviation ratios of ash sample PS B varied between 2.7 and 3.7 in the volume resistivity range. Ash sample PS C also showed an improved correlation between the predicted resistivity and experimental results, with the deviation ratio not exceeding 1.2 in the volume resistivity range. The modifications to the volume resistivity term of the Bickelhaupt model proved effective, since the average deviation decrease from 12 to 2.5 for PS A, 501 to 36 for PS B and 57 to 9 for PS C.

Table 5-4: Error ratio of volume corrected Bickelhaupt model at 120, 270°C and averaged for dry ambient conditions

Ambient Moisture (vol%)	PS A	PS B	PS C
120°C			
Dry	3.4	38	11
270°C			
Dry	1.5	3.4	1.1
Average (90 - 400°C)			
Dry	2.3	35.9	9.2

The volume corrected resistivity model was subsequently applied to humidified resistivity data to determine its accuracy in predicting the resistivity in moisturised environments, which is illustrated in Figure 5-6 for an ambient condition of 9.0 vol% moisture.

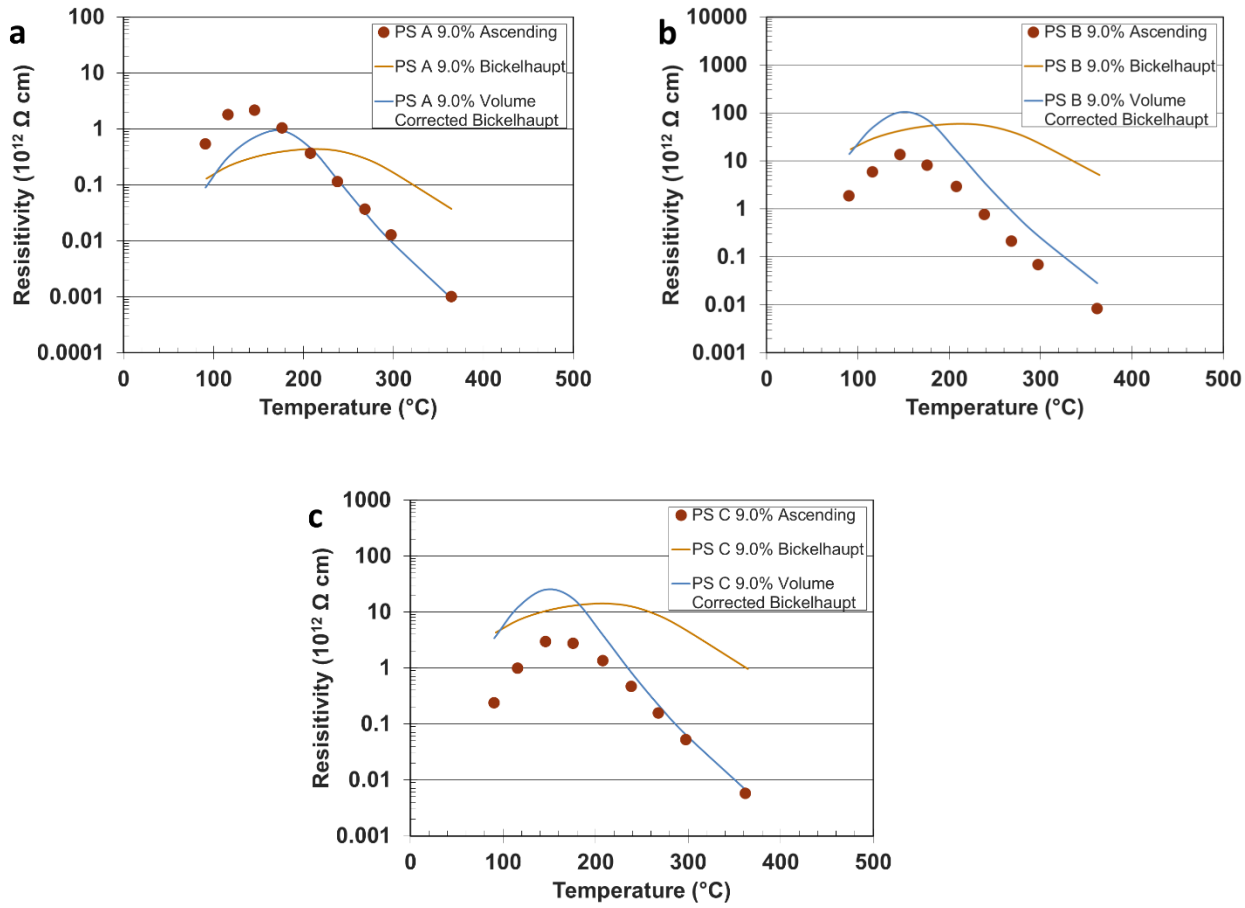


Figure 5-6: Experimental, Bickelhaupt and volume corrected Bickelhaupt resistivity at 9.0 vol% moisture for PS A (a), PS B (b) and PS C (c)

Different trends were shown by the figures, with the volume corrected model both over and under predicting the humidified resistivity data. For ash sample PS A the corrected Bickelhaupt model under predicted the surface resistivity, with deviations up to a factor of 5.9. While the volume corrected Bickelhaupt model under predicted the surface resistivity of PS A, it over predicted the surface resistivity of the two low sodium ash samples, PS B and PS C, yielding deviation ratios as high as 14 in the surface resistivity regime, suggesting further modifications to the model are required to improve the description of the surface resistivity. This is further supported when considering Table 5-5 where the deviation ratios of the volume corrected Bickelhaupt model are shown.

Table 5-5: Error Ratio of volume corrected Bickelhaupt model at 120, 270°C and averaged for 4.6, 6.0 and 9.0 vol% ambient moisture

Ambient Moisture (vol%)	PS A	PS B	PS C
	120°C		
4.6	5.4	4.7	7.1
6.0	5.8	5.1	8.9
9.0	5.8	8.5	12
	270°C		
4.6	1.2	3.7	1.4
6.0	1.1	3.5	1.5
9.0	1.1	4.3	1.4
	Average (90 - 400° C)		
4.6	4.3	5.2	6.4
6.0	4.6	5.6	7.5
9.0	4.0	8.1	10.4

5.3.3. Surface Corrected Bickelhaupt Correlation

Due to the inability of the volume corrected Bickelhaupt model to accurately predict the surface resistivity of the ash samples, further modifications were made to the surface resistivity term. The corrected model was expanded to take into account how South African ash components such as sodium influence the surface resistivity. In Figure 5-7, the comparison of the surface and volume corrected Bickelhaupt model together with the resistivity of experimental humidified ash samples are illustrated. Modifications to the surface resistivity term further reduced the error between the predicted value and the experimental values in the surface resistivity range. Ash sample PS A showed error ratios not exceeding 2.0 in the surface resistivity region, an error ratio acceptable for within-laboratory repeatability. Ash sample PS B, the sample which showed the largest deviation when applying the standard Bickelhaupt model, see Figure 5-4b, now showed an acceptable correlation with the error ratio not exceeding 2.4 in the surface resistivity region. Ash sample PS C showed an error ratio of 2.4, an error ratio considered acceptable for between-laboratory repeatability.

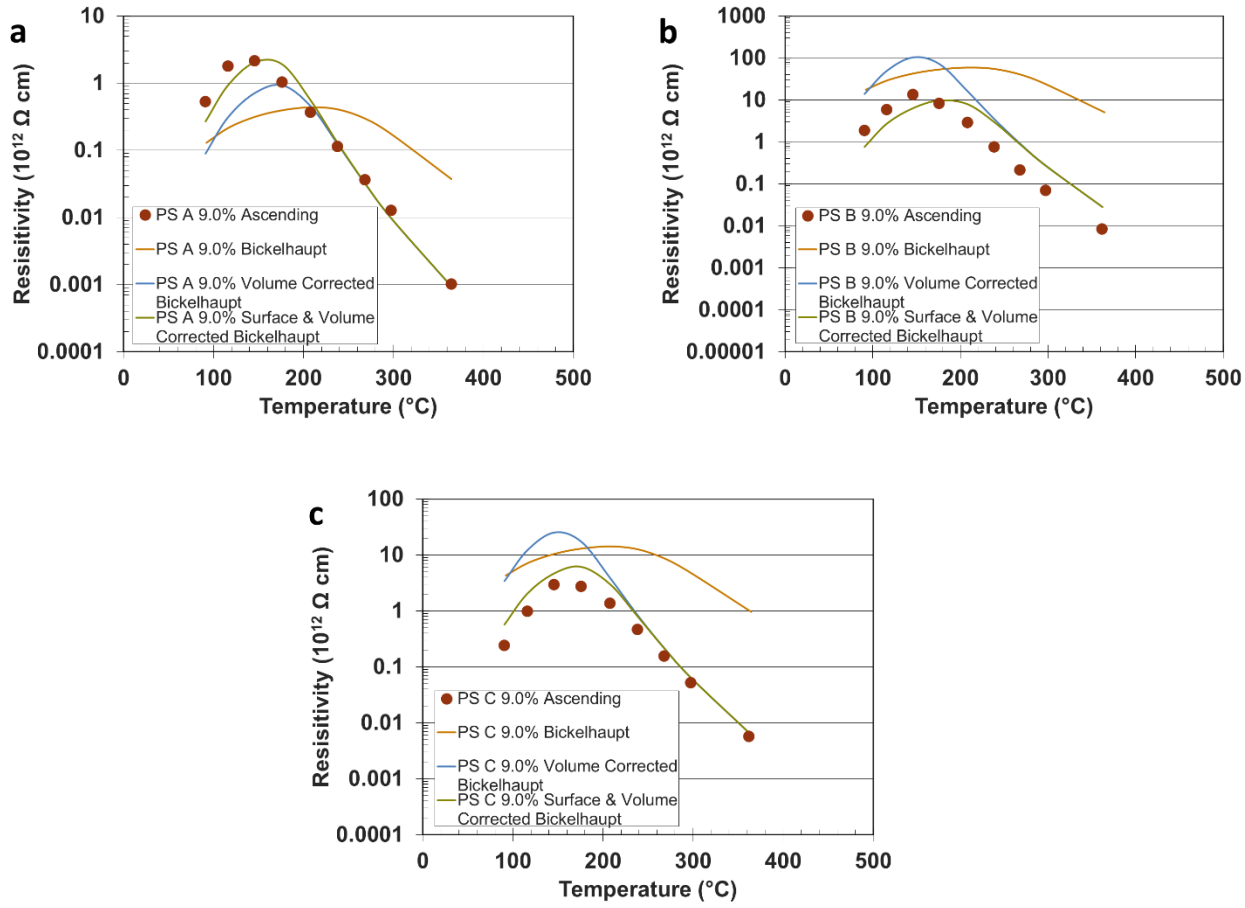


Figure 5-7: Experimental, Bickelhaupt, surface and volume corrected Bickelhaupt resistivity as a function of temperature at 9.0 vol% ambient moisture for PS A (a), PS B (b) and PS C (c)

The changes made to the Bickelhaupt model significantly improved the accuracy with which the model describes the surface resistivity of South African ashes. The modified surface resistivity term, represented by Eq. 5.2 and Table 5-6, better describes how sodium influences the resistivity of South African fly ashes.

$$\rho_{s0} = e^{A_s}\, x^{B_s} \qquad (5\text{-}2)$$

Table 5-6: Surface corrected Bickelhaupt constants

Bickelhaupt Constant	Original Value	Modified Value
A_S	22.6416	25.8948
B_S	-2.0618	-0.4267

The error ratios of the surface and volume corrected Bickelhaupt model at 120 and 270°C is shown in Table 5-7. It is apparent that the modified Bickelhaupt model is more adept at predicting resistivity values of low to medium sodium ashes, showing increased accuracy when compared to the standard Bickelhaupt model. The surface and volume corrected resistivity term reduced the average error from 12 to 1.7 for PS A, 501 to 2 for PS B and 57 to 2.1 for PS C.

Table 5-7: Error ratio of corrected Bickelhaupt model at 120, 270°C and averaged at 9.0 vol% ambient moisture

Ambient Moisture (vol%)	**PS A**	**PS B**	**PS C**
	120°C		
9.0	1.9	2.1	2.1
	270°C		
9.0	1.1	4.1	1.4
Average (90 - 400° C)			
9.0	1.7	2.0	2.1

5.3.4. Corrected Bickelhaupt Model at Various Moisture Levels

The modifications to the Bickelhaupt model were only carried out at 9.0 vol% moisture as this was also the original moisture content at which Bickelhaupt conducted the research and developed the model. In this prediction technique, the resistivity value at 9 vol% moisture is firstly determined, after which a correction, as given in Eq. H-6 in Appendix H, is applied to correct the resistivity to the required moisture content. Figure 5-8 illustrates how the surface and volume corrected Bickelhaupt model describes the resistivity of the sampled ashes at various ambient moisture conditions.

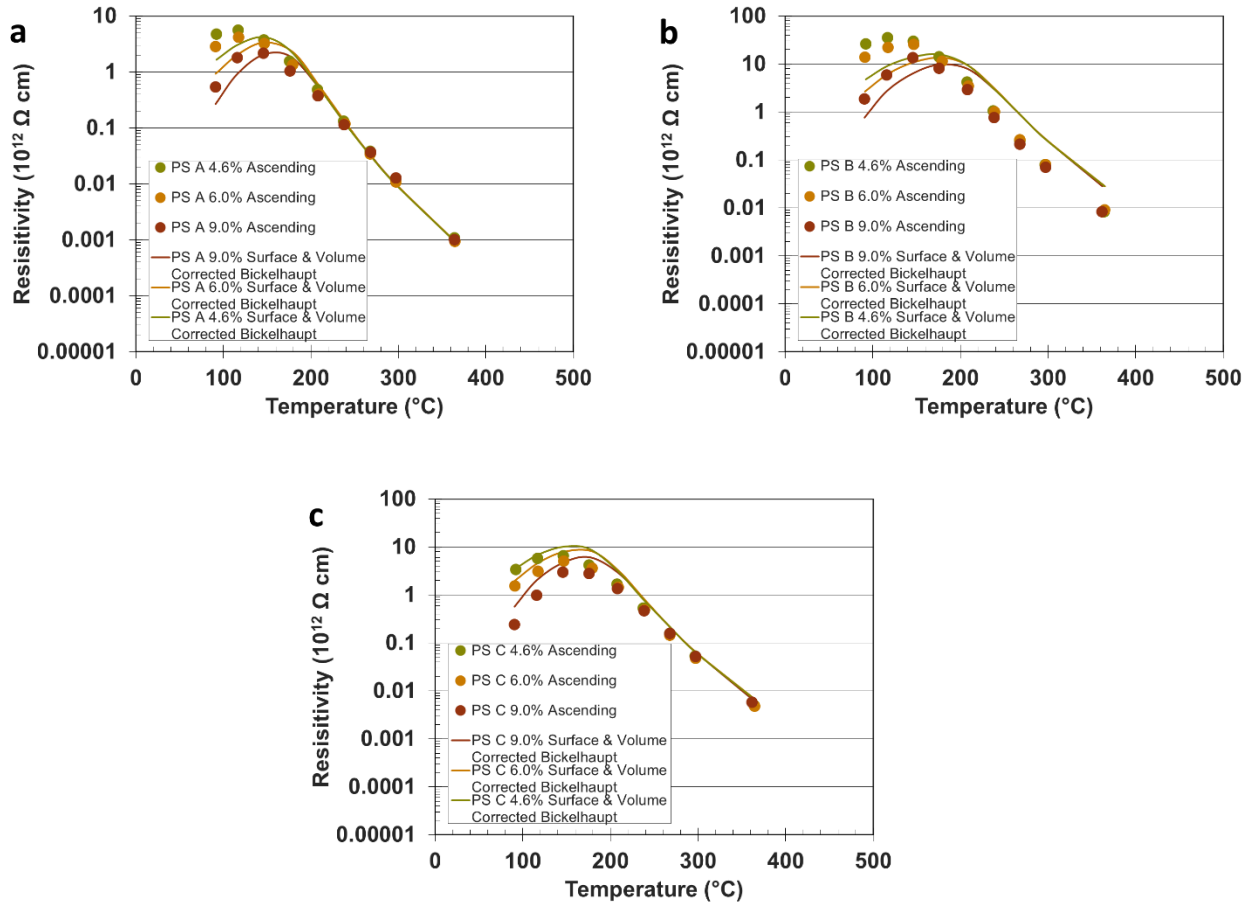


Figure 5-8: Experimental and corrected Bickelhaupt model resistivity as a function of temperature at 4.6, 6.0 and 9.0 vol% ambient moisture for PS A (a), PS B (b) and PS C (c)

The corrected Bickelhaupt model yielded mixed results at various moisture levels, as seen in Table 5-8, with the model becoming less accurate as the moisture was decreased for ash sample PS A. PS A, the ash sample which showed the best results thus far, yielded acceptable deviation ratios at 9.0 vol% moisture, however, at 4.6 and 6.0 vol% the error ratio increased to a maximum of 3 in the surface resistivity region, with the corrected model under estimating the resistivity. Ash sample PS B was also under estimated by the corrected model, showing larger deviations as the moisture content decreased. Alternatively, with ash sample PS C the model became more accurate with a decrease in moisture levels, with the corrected Bickelhaupt model reaching an error ratio of 1.1 at 90°C and 4.6 vol% moisture.

Table 5-8: Error ratio of corrected Bickelhaupt model at 120, 270°C and averaged for 4.6, 6.0 vol% ambient moisture

Ambient Moisture	PS A	PS B	PS C
	120°C		
4.6%	1.8	3.8	1.2
6.0%	1.9	3.5	1.5
	270°C		
4.6%	1.2	3.5	1.4
6.0%	1.1	3.4	1.5
	Average (90 - 400° C)		
4.6%	1.8	3.1	1.5
6.0%	1.9	3.0	1.7

6. Conclusion and Recommendations

The results from the elemental analysis of the sampled ashes were compared to American and Indian ashes and found to be more relatable with those of India. Like Indian ashes, the South African ashes showed no traces of lithium, an important resistivity reducing component. The South African ashes, like the Indian ashes, also showed reduced concentrations of sodium, the component considered the primary charge carrier.

Resistivity analysis of the sampled ashes at dry ambient conditions showed a linear relation between the log of resistivity and temperature. When moisture was introduced, the resistivity as a function of temperature showed the expected “bell curve” graph, with resistivity decreasing at temperatures below 200°C. As the amount of moisture increased, the decrease in resistivity became more pronounced. At temperature above 200°C, the effect of moisture became less noticeable, with resistivity values approaching those of dry conditions. It was concluded that the formation of a thin moisture layer on the surface of the ash particle facilitated the transfer of electrons below 200°C. At 150°C and 9.0 vol% ambient moisture the resistivity of the ash samples showed a reduction of 89 to 95% when compared to dry resistivities.

The Bickelhaupt model, along with the elemental composition of the coal ashes, was used to predict the resistivity of South African ashes. When compared with experimental data, large deviations were observed between the predicted values and the experimental values, with the Bickelhaupt model over estimating the resistivity of the South African ashes. Averaged error ratios of 12, 501 and 57 were found for PS A, B and C respectively when using the standard Bickelhaupt model. The inaccuracy of the Bickelhaupt model was attributed to low concentrations of sodium in South African ashes when compared to those of American coal ashes.

Alterations were made to the volume resistivity term of the Bickelhaupt model to better account for South African ash chemistry. Modifications to the volume resistivity term improved upon the accuracy with which the model could predict the resistivity at dry ambient conditions. When the volume corrected model was subsequently compared to humidified resistivity data it proved ineffective, over estimating the effect ambient moisture has on resistivity, suggesting that further modifications were required on the surface resistivity term of the Bickelhaupt model. The modifications to the surface resistivity term showed a further reduction, in the deviation between the predicted and experimental values, in the surface resistivity region. The modifications to the Bickelhaupt model increased the accuracy with

which the model could predict the dry and humidified resistivity of South African ashes. The corrected model showed averaged deviations of 1.7, 2.0 and 2.1 at 9 vol% ambient moisture for PS A, PS B and PS C respectively, less than the factor of 2.5 considered acceptable for Between-laboratory repeatability by the IEEE, proving that the modified Bickelhaupt correlations can in future be used for effective ESP design and operation when firing South African coals.

7. References

Aksay, I.A. & Pask, J.A. 1979. Densities of SiO_2 – Al_2O_3 melts. *Journal of the American Ceramic Society*, 62(1979): 7-8.

Ash Resources. 2017. Unclassified products. http://ashresources.co.za/ash-resources-products/ Date of Access: 19 November 2017.

Ayling, B., Rose, P., Petty, S., Zemach, E. & Drakos, P. 2012. QEMSCAN: Capability and application to fracture characterization in geothermal systems. 73rd Workshop on Geothermal Reservoir Engineering.

Bickelhaupt, R.E. 1974. Influence of fly ash composition factors on electrical volume resistivity. Washington: United States Environmental Protection Agency.

Bickelhaupt, R.E. 1975. Effect of chemical composition on surface resistivity of fly ash. Washington: United States Environmental Protection Agency.

Bickelhaupt, R.E. 1978. Measuring of fly ash resistivity using simulated flue gas environments. Washington: United States Environmental Protection Agency.

Bickelhaupt, R.E. 1979. A technique for predicting fly ash resistivity. Washington: United States Environmental Protection Agency.

Borm, P.J.A. 1997. Toxicity and occupational health hazards of coal fly ash (cfa). A review of data and comparison to coal mine dust. *The Annals of Occupational Hygiene*, 41(6): 659-676.

Bosch, F.J. & Buttle, R.S. 1993. Particulate emission control technology evaluation. Technology Research and Investigations. Eskom Holdings SOC Pty Ltd. (Unpublished).

Bosch, F.J., Tilley, H.A. & Khanda, E. 1995. Tutuka ash resistivity measurements. Technology Research and Investigations. Eskom Holdings SOC Pty Ltd. (Unpublished).

Chandra, A. 2013. Some investigations on fly ash resistivity generated in Indian power plants. 11th International Convergence on Electrostatic Precipitation.

Chandra, A., Kumar, S., Kumar, S & Sharma, P.K. 2006. Investigations on fly ash resistivity: Development of empirical relations based on experimental measurement. Australia, ICESP-X

Chauke, G & Gouws, R. 2013. Fly ash resistivity profiling for South African coal fired power stations. *Journal of Energy and Power Engineering*, 7(2013): 2306-2311.

Crelling, J.C. 1994. Targeting single coal macerals with density gradient centrifugation experiments. Carbondale: Southern Illinois University.

Eskom Holdings SOC Pty Ltd. 2013. Application for postponement of the minimum emission standards compliance timeframes for the Duvha power stations. https://cer.org.za/wp-content/uploads/2014/03/Annexure-1_Duvha-PS_Postponement-Application_Final_2013-12-13.pdf Date of Access: 19 November 2017.

Eskom Holdings SOC Pty Ltd. 2014a. Integrated report 2014. integratedreport.eskom.co.za /pdf/full-integrated.pdf Date of Access: 10 Feb 2015.

Eskom Holdings SOC Pty Ltd. 2014b. Cop17 Fact Sheet. http://www.google.com/url?sa=t&rct=j&q=&esrc=s&source=web&cd=1&ved=0CB8QFjAA&url=http%3A%2F%2Fwww.eskom.co.za%2FAboutElectricity%2FFactsFigures%2FDocuments%2FKusile_and_Medupi.pdf&ei=iNnZVLH7L8jharWngfAH&usg=AFQjCNFlsU23FpYZjS18BHBjzWh5z6S7JA&sig2=A6wdo_o1ajzJttktLcsaSg&bvm=bv.85464276,d.d2s Date of Access: 10 Feb 2015.

Eskom Holdings SOC Pty Ltd. 2015. Coal Power. http://www.eskom.co.za/AboutElectricity/ElectricityTechnologies/Pages/Coal_Power.aspx Date of Access: 10 Feb 2015.

Eskom Holdings SOC Pty Ltd. 2017. Company information interview. http://www.eskom .co.za/OurCompany/CompanyInformation/Pages/Company_Information.aspx Date of Access: 31 Oct 2017.

Eze, C.P., Nyale, S.M., Akinyeye, R.O., Gitari, W.M., Akinyemi, S.A., Fatoba, O.O. & Petrik, L.F. 2013. Chemical, mineralogical and morphological changes in weathered coal fly ash: A case study of a brine impacted wet ash dump. *Journal of Environmental Management*, 129(2013): 479-492.

Gooch, J.P., Bickelhaupt, R.E., Marchant, G.H., McRanie, R.D., Sparks, L.E. & Altman, R.F. 1981. Improvement of hot-side precipitator performance with sodium conditioning—An interim report. *Journal of the Air Pollution Control Association*, 31(1981): 291-297.

Haliday, D. Walker, J. & Resnick, R. 1970. Principles of physics. 9th ed. Danvers, MA: John Wiley & Sons Inc.

Hancox, P.J. & Götz, A.E. 2014. South Africa's coalfields-A 2014 perspective. *International Journal of Coal Geology*, 132(2014): 170-254.

Hankins, W.G. & George, R.E. 2011. Economic advantages of improved SO3 flue gas conditioning process. www.chemithon.com Date of Access: 6 June 2015.

Harrison, W.A., Nicholson, J.K., DuBard, J.L., Carlton, J.D. & Sparks, L.E. 1988. Medium-sulphur coal and fly ash resistivity. *Journal of the Air Pollution Control Association*, 38(2): 209-216.

Heaney, M.B. 1999. The Measurement, instrumentation and sensors handbook. 2nd ed. Boca Raton, FL: CRC Press LLC.

Hower, J.C., Groppo, J.G., Graham, U.M., Ward, C.R., Kostova, I.J., Maroto-Valer, M.M. & Dai, S. 2017. Coal-derived unburned carbons in fly ash: A review. *International Journal of Coal Geology*, 179(2017):11-27.

Huggins, F.E. 2002. Overview of analytical methods for inorganic constituents in coal. *International Journal of Coal Geology,* 50(2002): 169-214.

IEA. 2016. Key world energy statistics. Paris Cedex, France: IEA Coal Research.

IEEE. 1984. Standard criteria and guidelines for the laboratory measurement and reporting of fly ash resistivity, New York: Institute of Electrical and Electronics Engineers.

Jaworek, A., Krupa, A. & Czech, T. 2007. Modern electrostatic devices and methods for exhaust gas cleaning: A brief review. *Journal of Electrostatics,* 65(3): 133-155.

Jędrusik, M & Świerczok, A. 2004. The influence of fly ash physical and chemical properties on electrostatic precipitation process. *Journal of Electrostatics*, 67(2-3): 105-109.

Keir, J.B. 2017. Moisture values April 2013 to March 2014 [email]. 16 June 2017.

Keithley. 2000. Model 486 Pico-ammeter Model 487 Pico-ammeter/Voltage source instruction manual. Keithley Instruments. Cleveland, Ohio.

Keithley. 2001. Volume and surface resistivity measurements of insulating materials using the Model 6517A electrometer/High resistivity meter. www.keithley.com/data?asset=6069 Date of Access: 14 May 2015.

Keithley. 2005. Measuring the resistivity and determining the conductivity type of semiconductor materials using a four-point collinear probe and the Model 6221 DC and AC current source. www.keithley.com/data?asset=50280 Date of Access: 19 May 2015.

Klingspor, J.S. & Vernon, J.L. 1988. Particulate control for coal combustion. Putney Hill, London: IEA Coal Research.

Lister, R.A. & Peterson, T.J. 1996. Recent developments in dry ash handling. In: Raju VS, Datta M, Seshadri V, Agarwal VK, Kumar V, editors. Ash ponds and ash disposal systems. New Delhi: Narosa Publishing House.

Lowrie, W. 2010. Fundamentals of geophysics. 2nd ed. New York, NY: Cambridge University Press.

Malvern. 2017. Mastersizer 3000 smarter particle sizing https://www.malvern.com/en/assets/MRK1872_tcm22-17232.pdf Date of Access: 19 November 2017.

Marom, H. Mullin, J. & Eizenberg, M. 2006. Size-dependent resistivity of nanometric wires. *Physical Review B*. 74(45411): 1-9.

Matjie, R.H. French, D. Ward, C.R. Pistorius, P.C. & Li, Z. 2011. Behaviour of coal mineral matter in sintering and slagging of ash during the gasification process. *Fuel Processing Technology*, 92(8): 1426-1433.

McLean. K.J. 1976. Factors affecting the resistivity of a particulate layer in electrostatic precipitators. *Journal of the Air Pollution Control Association*, 26(9): 866-870

Mindat. 2018a. Anhydrite. https://www.mindat.org/min-234.html Date of Access: 14 Nov. 2018.

Mindat. 2018b. Anorthite. https://www.mindat.org/min-246.html Date of Access: 14 Nov. 2018.

Mindat. 2018c. Hematite. https://www.mindat.org/min-1856.html Date of Access: 14 Nov. 2018.

Mindat. 2018d. Kaolinite. https://www.mindat.org/min-2156.html Date of Access: 14 Nov. 2018.

Mindat. 2018e. Muscovite. https://www.mindat.org/min-2815.html Date of Access: 14 Nov. 2018.

Mindat. 2018f. Microcline. https://www.mindat.org/min-2704.html Date of Access: 14 Nov. 2018.

Mindat. 2018g. Pyrite. https://www.mindat.org/min-3314.html Date of Access: 14 Nov. 2018.

Mindat. 2018h. Quartz. https://www.mindat.org/min-3337.html Date of Access: 14 Nov. 2018.

Mindat. 2018i. Rutile. https://www.mindat.org/min-3486.html Date of Access: 14 Nov. 2018.

Nalbandian, H. 2006. Economics of retrofit air pollution control technologies. Putney Hill, London: IEA Coal Research.

Nimomiya, Y., Zhang, L., Sato, A. & Dong, Z.B. 2004. Influence of coal particle size on particulate matter emission and its chemical species produced during coal combustion. *Fuel Process Technology,* 85(8-10): 1065-1088.

Oglesby, S. & Nichols, G.B. 1978. Electrostatic precipitation. 1st ed. New York. NY: Marcel Dekker Inc.

Parker, K.R. 1997. Applied electrostatic precipitation. London: Blackie Academic & Professional.

Patel, E.M. & Swart, P. 2014. Eskom's experience in pulse jet fabric filter plants and filtration media. http://www.p84.com/sites/dc/Downloadcenter/Evonik/Product/P84/ppt_ eskom.pdf Date of Access: 16 Feb 2015.

Qi, L. & Yaun, Y. 2013. Mechanism of the effect of alkali metal on the electrostatic precipitability of fly ash. *Fuel,* 107(2013):848-851.

Ray, T.K. 2004. Air Pollution Control in industries-application of air pollution control equipment, vol 2. New Delhi: TechBooks International.

Ross, R.D. 1972. Air pollution and Industry. 1st ed. New York, NY: Van Nostrand Reinhold Company.

Senior, C.L., Zeng, T., Che, J., Amesb, M.R., Sarofimb, A.F. & Olmez, I. 2000. Distribution of trace elements in selected pulverized coals as a function of particle size and density. *Fuel Process Technology,* 63(2-3): 215-241.

Shanthakumar, S., Singh, D.N. & Phadke, R.C. 2008b. Influence of flue gas conditioning on fly ash characteristics. *Fuel,* 87(15-16):3216-3222.

Shanthakumar, S., Singh, D.N. & Phadke, R.C. 2008a. Flue gas conditioning for reducing suspended particulate matter from thermal power stations. *Progress in Energy and Combustion Science*, 34(6): 685-695.

Singh, D.N. & Kolay, P.K. 2002. Simulation of ash – water interaction and its influence on ash characteristics. *Progress in Energy and Combustion Science*, 28(3): 267-299.

Smith, W.F. & Hashemi, J. 2010. Foundations of material science and engineering. 5th ed. New York, NY: McGraw-Hill.

Soud, H.N. & Mitchell, S.C. 1997. Particulate control handbook for coal-fired plants. Putney Hill, London: IEA Coal Research.

Speight, J.G. 2013. Coal-fired power generation handbook. 1st ed. Beverly, MA: Scrivener Publishing.

Steinhögl, W., Shindler, G., Steinlesberger, G. & Engelhardt, M. 2002. Size-dependent resistivity of metallic wires in the mesoscopic range. *Physics Review B*, 66(75414): 1-4.

Swedish Energy Agency. 2012. Energy in Sweden, facts and figures. https://www.energimyndigheten.se/Global/Engelska/Facts%20and%20figures/Energy%20in%20Sweden%20facts%20and%20figures%202012%20%282%29.pdf Date of Access: 02 Feb 2015.

Van Alphen, C. 2007. Automated mineralogical analysis of coal and ash products – challenges and requirements. *Minerals Engineering*, 20(2007): 496-505.

Van Alphen, C. 2016. Power station fly ash. Research, Testing and Development. Technical memorandum. (Unpublished).

Van Wyk, L. 2015. The Correlation between Mineralogy and Resistivity in Typical South African Coal Ashes. Potchefstroom: NWU. (Thesis – MEng).

Ward, C.R. 2002. Analysis and significance of mineral matter in coal seams. *International Journal of Coal Geology,* 50(2002): 135-168.

White, H.J. 1953. Electrical resistivity of fly ash. *Air Repair,* 3(2): 79-86

White, H.J. 1974. Resistivity problems in electrostatic precipitation. *Journal of the Air Pollution Control Association*. 24(4): 313-338.

Wikipedia. 2018a. Calcium Oxide. https://en.wikipedia.org/wiki/Calcium_oxide Date of Access: 14 Nov 2018.

Wikipedia. 2018b. Dolomite. https://en.wikipedia.org/wiki/Dolomite Date of Access: 14 Nov 2018.

Williams, H., Pourkashanian, M., Jones, J.M. & Skorupska, N. 2000. Combustion and gasification of coal. New York: Taylor & Francis.

Xu, J. Gu, Z. & Zhang, J. 2014. Experimental study on fly ash resistivity at temperatures above 673K. *Fuel*, 116(2014): 650-654.

Yu, D.X., Xu, M.H., Sui, J.C., Liu, X.W., Yu, Y. & Cao, Q. 2004. Effect of coal particle size on the proximate composition and combustion properties. *Thermochimica Acta*, 439(1-2):103-109.

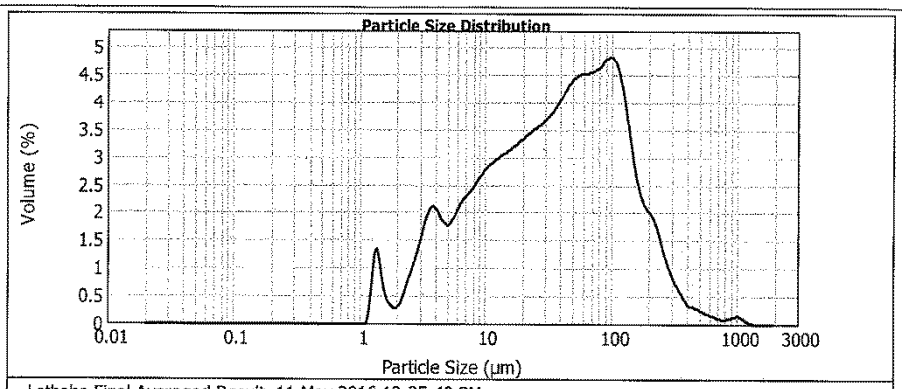
Appendix A: Particle Size Distribution for PS A, PS B and PS C

MASTERSIZER 2000

Result Analysis Report

Sample Name: Lethabo Final Averaged Result	**SOP Name:**	**Measured:** 11 May 2016 12:35:40 PM	
Sample Source & type: Malvern	**Measured by:** micron	**Analysed:** 11 May 2016 12:35:41 PM	
Sample bulk lot ref: 195325	**Result Source:** Averaged		
Particle Name: Silica 0.0	**Accessory Name:** Hydro 2000MU (A)	**Analysis model:** Single narrow mode (spherical)	**Sensitivity:** Enhanced
Particle RI: 1.544	**Absorption:** 0	**Size range:** 0.020 to 2000.000 um	**Obscuration:** 14.13 %
Dispersant Name: Water	**Dispersant RI:** 1.330	**Weighted Residual:** 1.178 %	**Result Emulation:** Off
Concentration: 0.0237 %Vol	**Span :** 3.964	**Uniformity:** 1.39	**Result units:** Volume
Specific Surface Area: 0.464 m²/g	**Surface Weighted Mean D[3,2]:** 12.935 um	**Vol. Weighted Mean D[4,3]:** 67.542 um	

d(0.1): 4.645 um d(0.5): 38.026 um d(0.9): 155.386 um



Size (µm)	Volume In %	Size (µm)	Volume In %	Size (µm)	Volume In %	Size (µm)	Volume In %	Size (µm)	Volume In %	Size (µm)	Volume In %
0.020	0.00	0.142	0.00	1.002	0.00	7.096	1.78	50.238	3.35	355.656	0.34
0.022	0.00	0.159	0.00	1.125	0.22	7.962	1.89	56.368	3.39	399.052	0.23
0.025	0.00	0.178	0.00	1.262	1.07	8.934	2.03	63.246	3.41	447.744	0.21
0.028	0.00	0.200	0.00	1.416	0.68	10.024	2.12	70.963	3.43	502.377	0.16
0.032	0.00	0.224	0.00	1.589	0.28	11.247	2.20	79.621	3.51	563.677	0.12
0.036	0.00	0.252	0.00	1.783	0.20	12.619	2.26	89.337	3.61	632.456	0.09
0.040	0.00	0.283	0.00	2.000	0.29	14.159	2.32	100.237	3.60	709.627	0.05
0.045	0.00	0.317	0.00	2.244	0.55	15.887	2.38	112.468	3.36	796.214	0.07
0.050	0.00	0.356	0.00	2.518	0.60	17.825	2.46	126.191	2.86	893.367	0.09
0.056	0.00	0.399	0.00	2.825	1.10	20.000	2.53	141.589	2.26	1002.374	0.09
0.063	0.00	0.448	0.00	3.170	1.41	22.440	2.61	158.866	1.80	1124.683	0.03
0.071	0.00	0.502	0.00	3.557	1.59	25.179	2.67	178.250	1.57	1261.915	0.00
0.080	0.00	0.564	0.00	3.991	1.48	28.251	2.74	200.000	1.45	1415.892	0.00
0.089	0.00	0.632	0.00	4.477	1.34	31.698	2.83	224.404	1.23	1588.656	0.00
0.100	0.00	0.710	0.00	5.024	1.36	35.566	2.96	251.765	0.91	1782.502	0.00
0.112	0.00	0.796	0.00	5.637	1.53	39.905	3.10	282.508	0.66	2000.000	0.00
0.126	0.00	0.893	0.00	6.325	1.68	44.774	3.25	316.979	0.49		
0.142		1.002		7.096		50.238		355.656			

Operator notes: *Average of 3 measurements from Jandri_Fly Ash1.mea*

Malvern Instruments Ltd.
Malvern, UK
Tel := +[44] (0) 1684-892456 Fax +[44] (0) 1684-892789

Mastersizer 2000 Ver. 5.60
Serial Number : MAL100928

File name: Jandri_Fly Ash1.mea
Record Number: 121
2016/05/12 01:10:22 PM

MASTERSIZER 2000

Result Analysis Report

Sample Name:
Matimb Final Averaged Result

SOP Name:

Measured:
11 May 2016 02:21:36 PM

Sample Source & type:
Malvern

Measured by:
micron

Analysed:
11 May 2016 02:21:38 PM

Sample bulk lot ref:
195325

Result Source:
Averaged

Particle Name:
Silica 0.0

Accessory Name:
Hydro 2000MU (A)

Analysis model:
Single narrow mode (spherical)

Sensitivity:
Enhanced

Particle RI:
1.544

Absorption:
0

Size range:
0.020 to 2000.000 um

Obscuration:
15.64 %

Dispersant Name:
Water

Dispersant RI:
1.330

Weighted Residual:
0.619 %

Result Emulation:
Off

Concentration:
0.0386 %Vol

Span :
3.520

Uniformity:
1.11

Result units:
Volume

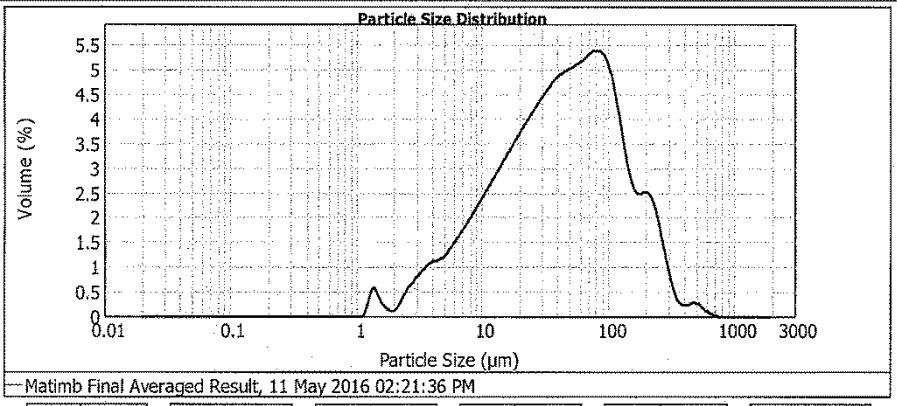
Specific Surface Area:
0.33 m²/g

Surface Weighted Mean D[3,2]:
18.209 um

Vol. Weighted Mean D[4,3]:
68.743 um

---

d(0.1): 7.667 um d(0.5): 44.115 um d(0.9): 162.961 um



Size (µm)	Volume In %
0.020	0.00
0.022	0.00
0.025	0.00
0.028	0.00
0.032	0.00
0.036	0.00
0.040	0.00
0.045	0.00
0.050	0.00
0.056	0.00
0.063	0.00
0.071	0.00
0.080	0.00
0.089	0.00
0.100	0.00
0.112	0.00
0.126	0.00
0.142	0.00

Size (µm)	Volume In %
0.142	0.00
0.159	0.00
0.178	0.00
0.200	0.00
0.224	0.00
0.252	0.00
0.283	0.00
0.317	0.00
0.356	0.00
0.399	0.00
0.448	0.00
0.502	0.00
0.564	0.00
0.632	0.00
0.710	0.00
0.796	0.00
0.893	0.00
1.002	0.00

Size (µm)	Volume In %
1.002	0.00
1.125	0.09
1.262	0.45
1.416	0.28
1.589	0.13
1.783	0.07
2.000	0.13
2.244	0.32
2.518	0.47
2.825	0.58
3.170	0.69
3.557	0.80
3.991	0.84
4.477	0.88
5.024	0.98
5.637	1.11
6.325	1.25
7.096	1.39

Size (µm)	Volume In %
7.096	1.39
7.962	1.55
8.934	1.71
10.024	1.87
11.247	2.03
12.619	2.20
14.159	2.37
15.887	2.53
17.825	2.69
20.000	2.85
22.440	3.01
25.179	3.16
28.251	3.31
31.698	3.45
35.566	3.58
39.905	3.68
44.774	3.74
50.238	3.80

Size (µm)	Volume In %
50.238	3.80
56.368	3.86
63.246	3.94
70.963	4.02
79.621	4.05
89.337	3.97
100.237	3.71
112.468	3.24
126.191	2.65
141.589	2.13
158.866	1.88
178.250	1.87
200.000	1.87
224.404	1.65
251.785	1.21
282.508	0.75
316.979	0.37
355.656	0.18

Size (µm)	Volume In %
355.656	0.18
399.052	0.16
447.744	0.20
502.377	0.17
563.677	0.08
632.456	0.03
709.627	0.00
796.214	0.00
893.387	0.00
1002.374	0.00
1124.683	0.00
1261.915	0.00
1415.892	0.00
1588.656	0.00
1782.502	0.00
2000.000	

Operator notes: *Average of 3 measurements from Jandri_Fly Ash1.mea*

Malvern Instruments Ltd.
Malvern, UK
Tel := +[44] (0) 1684-892456 Fax +[44] (0) 1684-892789

Mastersizer 2000 Ver. 5.60
Serial Number : MAL100928

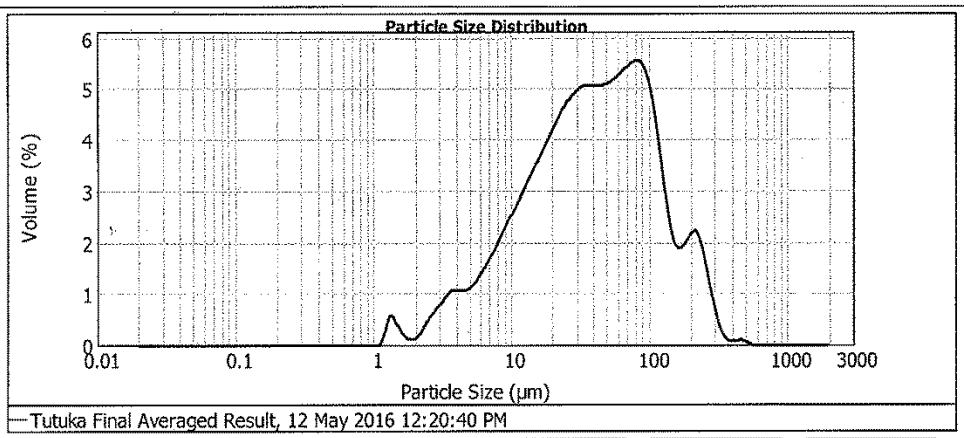
File name: Jandri_Fly Ash1.mea
Record Number: 125
2016/05/12 01:15:48 PM

MASTERSIZER 2000

Result Analysis Report

Sample Name: Tutuka Final Averaged Result	**SOP Name:**	**Measured:** 12 May 2016 12:20:40 PM	
Sample Source & type: Malvern	**Measured by:** micron	**Analysed:** 12 May 2016 12:20:41 PM	
Sample bulk lot ref: 195325	**Result Source:** Averaged		
Particle Name: Silica 0.0	**Accessory Name:** Hydro 2000MU (A)	**Analysis model:** Single narrow mode (spherical)	**Sensitivity:** Enhanced
Particle RI: 1.544	**Absorption:** 0	**Size range:** 0.020 to 2000.000 um	**Obscuration:** 14.67 %
Dispersant Name: Water	**Dispersant RI:** 1.330	**Weighted Residual:** 0.868 %	**Result Emulation:** Off
Concentration: 0.0358 %Vol	**Span :** 3.245	**Uniformity:** 1.06	**Result units:** Volume
Specific Surface Area: 0.333 m²/g	**Surface Weighted Mean D[3,2]:** 18.017 um	**Vol. Weighted Mean D[4,3]:** 60.929 um	

d(0.1): 7.981 um **d(0.5):** 40.042 um **d(0.9):** 137.928 um



Size (µm)	Volume In %	Size (µm)	Volume In %	Size (µm)	Volume In %	Size (µm)	Volume In %	Size (µm)	Volume In %	Size (µm)	Volume In %
0.020	0.00	0.142	0.00	1.002	0.00	7.096	1.36	50.238	3.86	355.656	0.07
0.022	0.00	0.159	0.00	1.125	0.10	7.962	1.56	56.368	3.94	399.052	0.05
0.025	0.00	0.178	0.00	1.262	0.46	8.934	1.78	63.246	4.04	447.744	0.07
0.028	0.00	0.200	0.00	1.416	0.26	10.024	1.99	70.963	4.14	502.377	0.01
0.032	0.00	0.224	0.00	1.589	0.11	11.247	2.20	79.621	4.18	563.677	0.00
0.036	0.00	0.252	0.00	1.783	0.07	12.619	2.41	89.337	4.04	632.456	0.00
0.040	0.00	0.283	0.00	2.000	0.13	14.159	2.60	100.237	3.63	709.627	0.00
0.045	0.00	0.317	0.00	2.244	0.30	15.887	2.80	112.468	2.94	796.214	0.00
0.050	0.00	0.356	0.00	2.518	0.44	17.825	3.01	126.191	2.15	893.367	0.00
0.056	0.00	0.399	0.00	2.825	0.57	20.000	3.22	141.589	1.57	1002.374	0.00
0.063	0.00	0.448	0.00	3.170	0.69	22.440	3.42	158.866	1.39	1124.683	0.00
0.071	0.00	0.502	0.00	3.557	0.79	25.179	3.60	178.250	1.54	1261.915	0.00
0.080	0.00	0.564	0.00	3.991	0.79	28.251	3.73	200.000	1.67	1415.692	0.00
0.089	0.00	0.632	0.00	4.477	0.80	31.698	3.79	224.404	1.48	1588.656	0.00
0.100	0.00	0.710	0.00	5.024	0.88	35.566	3.81	251.785	1.01	1782.502	0.00
0.112	0.00	0.796	0.00	5.637	1.03	39.905	3.81	282.508	0.53	2000.000	0.00
0.126	0.00	0.893	0.00	6.325	1.19	44.774	3.82	316.979	0.19		
0.142	0.00	1.002	0.00	7.096	1.36	50.238	3.82	355.656	0.07		

Operator notes: *Average of 3 measurements from Jandri_Fly Ash1.mea*

Malvern Instruments Ltd.
Malvern, UK
Tel := +[44] (0) 1684-892456 Fax +[44] (0) 1684-892789

Mastersizer 2000 Ver. 5.60
Serial Number : MAL100928

File name: Jandri_Fly Ash1.mea
Record Number: 129
2016/05/12 01:20:50 PM

Appendix B: Instrument Details and Settings

The instrument details and settings for the Malvern Mastersizer, used for particle size distribution, are shown in Table B-1.

Table B-1: Malvern Mastersizer instrument settings

Specification	Setting
Particle Name	Silica 0.0
Particle RI	1.544
Dispersant Name	Water
Dispersant RI	1.330
Accessory Name	Hydro 2000MU (A)
Analysis Model	Single Narrow Mode (Spherical)
Size Range	0.020 – 2000 µm

The instrument details and setting used for XRD analysis, are shown in Table B-2.

Table B-2: XRD instrument settings

Specification	Setting
Scan Axis	Gonio
Start Position [°20]	6.0084
End Position[°20]	109.9804
Step Size [°20]	0.0170
Scan Step Time [s]	15.2400
Scan Type	Continuous
PSD Mode	Scanning
PSD Length [°20]	2.12
Offset [°20]	0.0000
Divergence Slit Type	Fixed
Divergence Slit Size [°]	0.9570
Specimen Length [mm]	10.00
Measurement Temperature [°C]	25
Anode Material	Co
K-Alpha 1 [Å]	1.78901
K-Alpha 2 [Å]	1.792

The instrument details and setting used for QEMSCAN analysis, are shown in Table B-3.

Table B-3: QEMSCAN instrument settings

Specification	Setting
iMeasure	v. 5.2
Platform	SEM
Accelerating Voltage [kV]	25
Specimen Current [nA]	-5
Beam Optimization Frequency [hrs.]	0.5
Working Distance [mm]	22
BSE Background Threshold	17
Brightness	-48
Contrast	-19
B&C Line Scan Setting	Min. on Faraday Cup, Max. on Gold Std.
BSE Calibration	
Std. 1, BSE Target	Gold, 232
Std. 2, BSE Target	Quartz, 42
Std. 3, BSE Target	Faraday Cup, 5

Bureau Veritas Testing and Inspections South Africa
Sunderland Ridge
Reg N° 2002/003217/07

North West University
For Attention: Jandri Ribberink
Email: jandriribberink@gmail.com

Ref No:	**1718-1102**
Date Received:	19/10/2017
Contact Person:	W Swanepoel
Report Status:	FINAL
Report Date:	03/11/2017

308 Barolong Street
Icon Industrial Park
Sunderland Ridge X10
PO Box 11498
Wierda Park South 0057
Tel: +27(0)12 940 0911
Fax: +27(0)86 631 4743

AMENDMENT TEST REPORT / CERTIFICATE OF ANALYSIS

Sample Identification			MATIMBA	TUTUKA	LETHA
Proximate Analysis	% Inherent moisture content	*(air-dried)*	0.2	0.2	0.1
	% Ash content	*(air-dried)*	98.7	96.7	99.4
	% Ash content	*(dry basis)*	98.9	96.9	99.5
	% Volatile Matter	*(air-dried)*	1.0	2.0	0.6
	% Volatile Matter	*(dry basis)*	1.0	2.0	0.6
	%Fixed carbon *(by calculation)*	*(air-dried)*	0.1	1.1	0.0
	Calorific Value (MJ/kg)	*(Determined)*	0.36	0.21	0.19

Description	Procedure / Test Method
Sample preparation	ACT-TPM-001 based on ISO 13909-4: 2001
Moisture content (%)	ACT-TPM-010 based on ISO11722: 1999
Ash content (%)	ACT-TPM-011 based on ISO 1171: 2010
Volatile matter content (%)	ACT-TPM-012 based on ISO 562: 2010
Gross calorific value (MJ/kg)	ACT-TPM-014 based on ISO 1928: 2009

Results marked "Not SANAS Accredited" in this report are not included in the SANAS Schedule of Accreditation for this laboratory.
Results marked "Subcontracted Test" in this report are not included in the SANAS Schedule of Accreditation for this laboratory.

Results reported are only representative of the sample received for testing. Sample preparation will deviate from ISO13909-4: 2001(E) Table 1 (Minimum Mass of Samples After Division) where insufficient material was supplied or generated due to the nature of the requirements. While every endeavour has been made to ensure that the results reported are accurate, Bureau Veritas Testing and Inspections South Africa shall not be liable for any error nor for any damage or loss what so ever that may arise from the issuing of this certificate. This certificate may not be reproduced in part or full without written permission from the Technical Managers of Bureau Veritas Testing and Inspections South Africa. Please note that samples will be discarded three months after date of Final Report unless instructed otherwise by client.

C.W. Swanepoel
Technical Signatory

sanas Testing Laboratory
T0469

Appendix C: Proximate Analysis and Calorific Values

Bureau Veritas Testing and Inspections South Africa
Sunderland Ridge
Reg Nº 2002/003217/07

North West University
For Attention: Jandri Ribberink
Email: jandriribberink@gmail.com

Ref No:	**1718-849**
Date Received:	08/08/2017
Contact Person:	W Swanepoel
Report Status:	FINAL
Report Date:	23/08/2017

308 Barolong Street
Icon Industrial Park
Sunderland Ridge X10
PO Box 11498
Wierda Park South 0057
Tel: +27(0)12 940 0911
Fax: +27(0)86 631 4743

Appendix D: XRF Results

AMENDMENT TEST REPORT / CERTIFICATE OF ANALYSIS

Sample Identification			PS B	PS C	PS A
Ash Composition (XRF)	Al_2O_3	%	26.92	29.00	30.19
	CaO	%	3.40	5.44	4.31
	Cr_2O_3	%	0.02	0.04	0.03
	Fe_2O_3	%	6.43	5.46	3.56
	K_2O	%	0.80	0.67	0.68
	MgO	%	1.03	1.33	0.99
	MnO	%	0.09	0.05	0.03
	Na_2O	%	0.03	0.06	0.35
	P_2O_5	%	0.39	0.38	0.34
	SiO_2	%	58.04	55.34	56.84
	TiO_2	%	1.25	1.57	1.51
	V_2O_5	%	0.03	0.02	0.03
	ZrO_2	%	0.07	0.07	0.06
	BaO	%	0.12	0.12	0.10
	SrO	%	0.05	0.12	0.09
	ZnO	%	0.02	0.01	nd
	SO_3	%	0.47	0.39	0.28

Description	Procedure / Test Method
Ash composition	ASTM D4326 XRF – By fusion bead (Subcontracted Test)

Results marked "Not SANAS Accredited" in this report are not included in the SANAS Schedule of Accreditation for this laboratory.
Results marked "Subcontracted Test" in this report are not included in the SANAS Schedule of Accreditation for this laboratory.

Results reported are only representative of the sample received for testing. Sample preparation will deviate from ISO13909-4: 2001(E) Table 1 (Minimum Mass of Samples After Division) where insufficient material was supplied or generated due to the nature of the requirements. While every endeavour has been made to ensure that the results reported are accurate, Bureau Veritas Testing and Inspections South Africa shall not be liable for any error nor for any damage or loss what so ever that may arise from the issuing of this certificate. This certificate may not be reproduced in part or full without written permission from the Technical Managers of Bureau Veritas Testing and Inspections South Africa. Please note that samples will be discarded three months after date of Final Report unless instructed otherwise by client.

C.W. Swanepoel
Technical Signatory

sanas Testing Laboratory
T0469

The XRF determined elemental ash composition of ash sample PS A, PS B and PS C is shown in Table D-1.

Table D-1: Elemental ash composition (wt%)

Sample	PS A	PS B	PS C
Al_2O_3	30.4	27.2	29.0
CaO	4.3	3.4	5.4
Fe_2O_3	3.6	6.5	5.5
K_2O	0.7	0.8	0.7
MgO	1.0	1.0	1.3
MnO	T	0.1	0.1
Na_2O	0.4	T	0.1
P_2O_5	0.3	0.4	0.4
SiO_2	57.2	58.5	55.3
TiO_2	1.5	1.3	1.6
SO_3	0.3	0.5	0.4

T – Trace Amounts

The historical XRF values determined by Bosch (1993, 1995) for ash sample PS A, PS B and PS C are shown in Table D-2.

Table D-2: Historical Eskom XRF results (wt%) (Taken from: Bosch, 1993, Bosch, 1995)

Sample	PS A	PS B	PS C
Al_2O_3	32.8	20.7	25.7
CaO	5.0	2.7	5.8
Fe_2O_3	3.8	6.3	5.4
K_2O	0.5	1.0	0.5
MgO	1.2	ND	2.1
MnO	T	0.1	0.2
Na_2O	0.1	0.1	0.5
P_2O_5	0.40	0.10	0.1
SiO_2	54.32	67.1	57.8
TiO_2	1.71	0.9	1.5
SO_3	0.10	0.2	0.5

ND – Not Detected

T – Trace Amounts

Appendix E: XRD Results

The XRD determined ash mineral composition of sample PS A, PS B and PS C is shown in Table E-1.

Table E-1: X-Ray Diffraction analysis (wt%)

Mineral	PS A	PS B	PS C	PS A + Amorphous	PS B + Amorphous	PS C + Amorphous
Mullite	49.7	44.6	47.7	29.7	28.6	27.9
Quartz	21.3	29.8	23	12.6	12.9	14.3
Silimanite	23	20	17.9	11.8	4.7	2.2
Hematite	3	2	9.7	0.7	5	3.7
Rutile	ND	0.1	ND	0.1	0.1	ND
Anatase	0.3	ND	0.2	0.1	ND	ND
Anorthite	1.4	0.6	0.6	1.5	0.7	0.9
Cristobalite	0.4	0.9	0.1	0.1	0.1	0.1
Lime	0.4	0.1	0.6	0.2	0.2	0.4
Magnetite	0.4	2	0.2	0.4	ND	0.7
Amorphous Content				42.8	47.6	49.9

ND – Not Detected

Appendix F: QEMSCAN Results

Figure F-1, Figure F-2 and Figure F-3 represent a pictorial representation of the mineralogical composition of the fly ash samples.

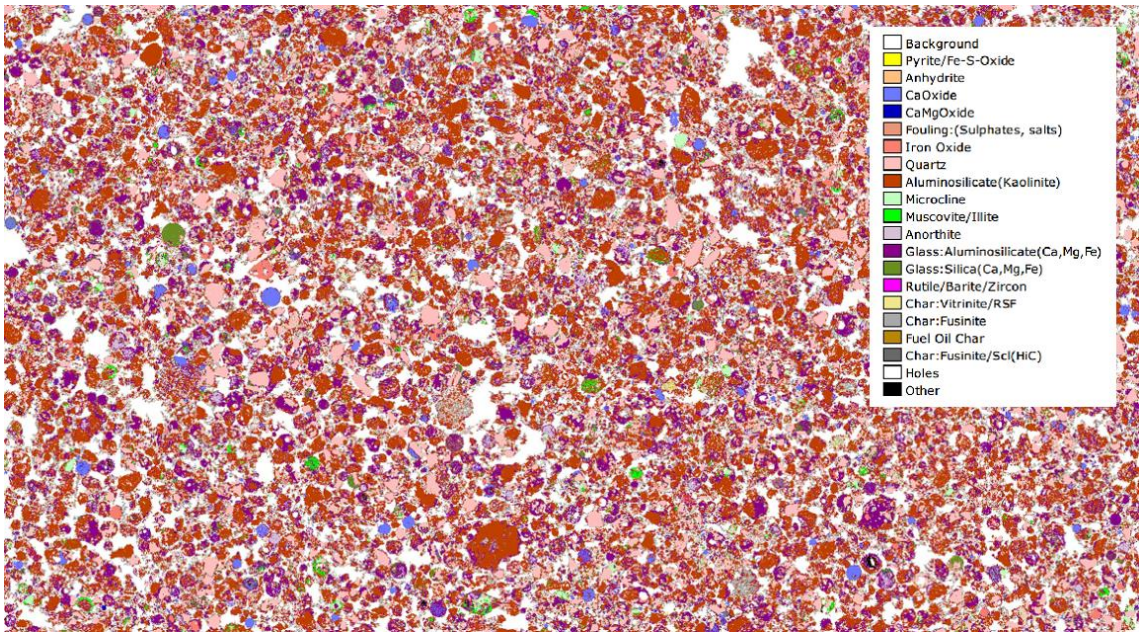


Figure F-1: Mineralogical QEMSCAN results of ash sample PS A

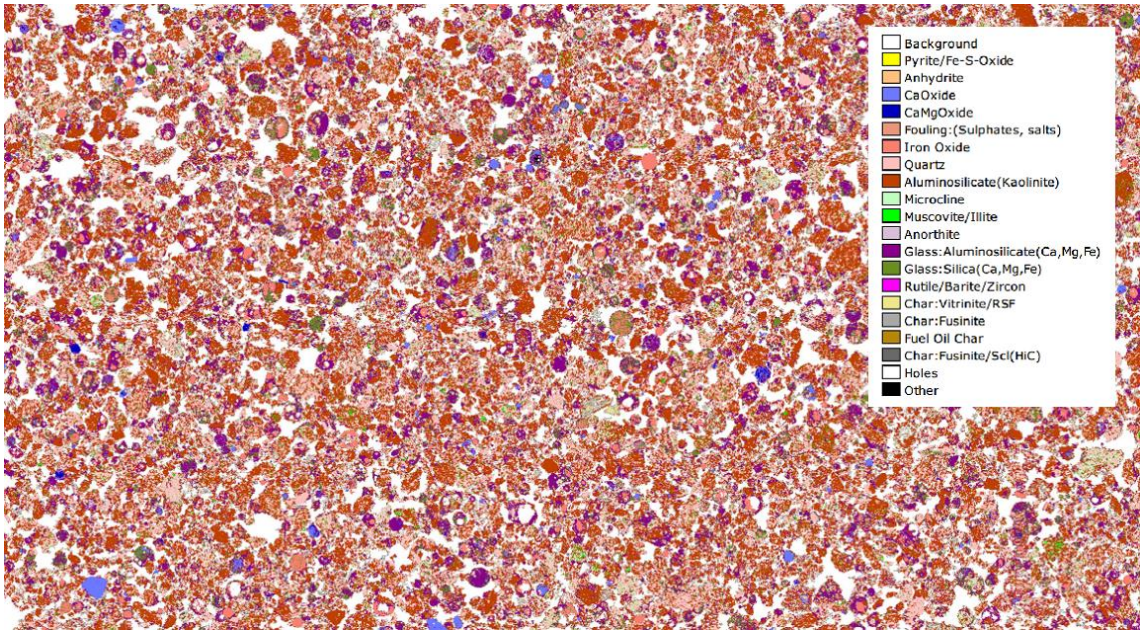


Figure F-2: Mineralogical QEMSCAN results of ash sample PS B

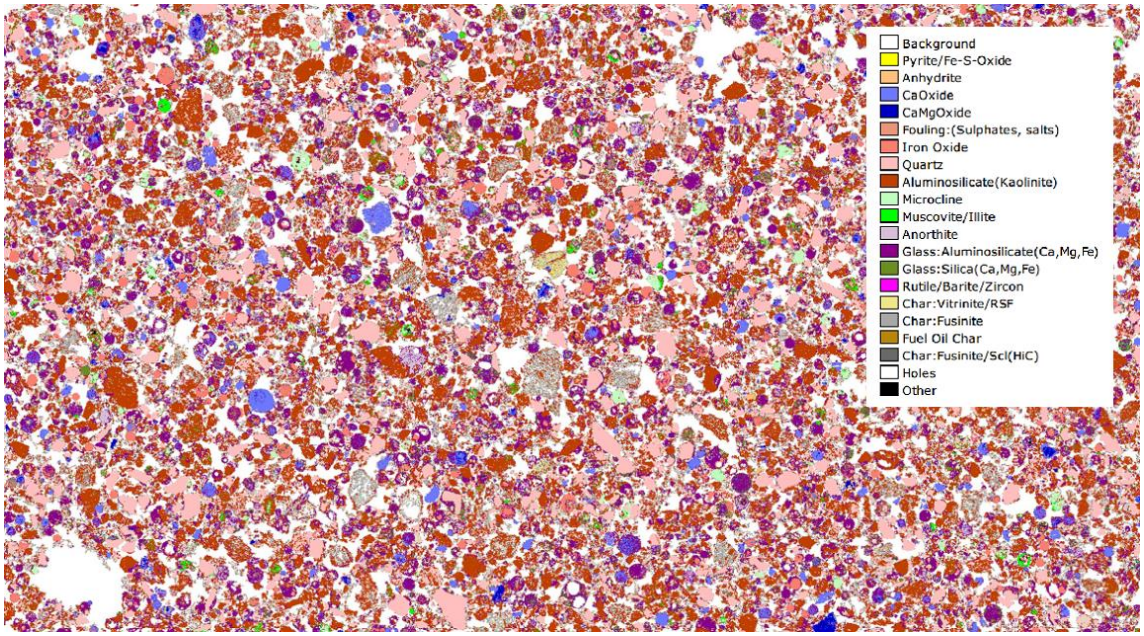


Figure F-3: Mineralogical QEMSCAN results of ash sample PS C

The volume proportions from QEMSCAN analysis of the sampled ashes are shown in Table F-1.

Table F-1: Mineralogical QEMSCAN volume proportions (vol%)

Mineral	PS A	PS B	PS C
Pyrite/Fe-S-Oxides	ND	ND	ND
Iron Oxides	1.3	2.8	3.2
Anhydrite	ND	0.1	0.2
CaOxides	1.7	1.2	3.4
CaMgOxides	0.1	0.2	0.5
Fouling:(Sulphates, Salts)	ND	ND	ND
Quartz	20.6	23.3	21.1
Aluminosilicate(Kaolinite)	36.2	37.5	31.6
Microcline	0.9	1.9	0.9
Muscovite/Illite	1.1	1.1	1.1
Anorthite	1.1	0.3	1.2
Glass: Aluminosilicate(Ca,Mg,Fe)	18.1	15.1	17.4
Glass: Silica(Ca,Mg,Fe)	3	5.2	3.1
Rutile/Barite/Zircon	0	0	0
Char: Vitrinite/RSF	1.3	1.1	1.4
Char: Fusinite	14.3	10	14.8
Char: Fusinite/Scl(HiC)	ND	ND	ND
Fuel Oil Char	ND	ND	0.1
Other	0.2	0.1	0.1

ND – Not Detected

The densities of the minerals detected by QEMSCAN analysis are shown in Table F-2

Table F-2: Mineral densities (kg/m^3)

Mineral	Mineral Density	Source
Pyrite/Fe-S-Oxides	5010	Mindat (2018g)
Iron Oxides	5240	Mindat (2018c)
Anhydrite	2970	Mindat (2018a)
CaOxides	3350	Wikipedia (2018a)
CaMgOxides	2850	Wikipedia (2018b)
Quartz	2650	Mindat (2018h)
Aluminosilicate(Kaolinite)	2650	Mindat (2018d)
Microcline	2560	Mindat (2018e)
Muscovite/Illite	2880	Mindat (2018f)
Anorthite	2730	Mindat (2018b)
Glass: Aluminosilicate(Ca,Mg,Fe)	2774	Aksay & Pask (1979)
Glass: Silica(Ca,Mg,Fe)	2650	Mindat (2018h)
Rutile/Barite/Zircon	4460	Mindat (2018i)
Char: Vitrinite/RSF	1300	Crelling (1994)
Char: Fusinite	1600	Crelling (1994)
Other	3045	Taken as Average

The weight proportions of the minerals detected by QEMSCAN analysis are shown in Table F-3. The weight percentages are determined from the volume percentage shown in Table F-1 and the mineral densities shown in Table F-2.

Table F-3: Mineralogical QEMSCAN weight proportions (wt%)

Mineral	PS A	PS B	PS C
Pyrite/Fe-S-Oxides	ND	ND	ND
Iron Oxides	2.7	5.6	6.4
Anhydrite	ND	0.1	0.2
CaOxides	2.2	1.5	4.4
CaMgOxides	0.1	0.2	0.6
Fouling:(Sulphates. Salts)	ND	ND	ND
Quartz	21.4	23.5	21.4
Aluminosilicate(Kaolinite)	37.6	37.8	32.1
Microcline	0.9	1.9	0.9
Muscovite/Illite	1.2	1.2	1.2
Anorthite	1.2	0.3	1.3
Glass: Aluminosilicate(Ca,Mg,Fe)	19.7	15.9	18.5
Glass: Silica(Ca,Mg,Fe)	3.1	5.2	3.2
Rutile/Barite/Zircon	ND	ND	ND
Char: Vitrinite/RSF	0.7	0.5	0.7
Char: Fusinite	9.0	6.1	9.1
Char: Fusinite/Scl(HiC)	ND	ND	ND
Fuel Oil Char	ND	ND	ND
Other	0.2	0.1	0.1

ND – Not Detected

Appendix G: Comparison of Elemental and Mineralogical Results

To compare the different analytical methods, a select number of species are displayed in Table G-1. The two most abundant species, Al and Si were summed and compared. XRF and QEMSCAN analysis proved more relatable with one another, with XRD showing a large deviation.

Table G-1: Comparison between XRF, XRD & QEMSCAN (wt%)

Species (PS A)	**XRF**	**XRD**	**QEMSCAN**	**QEMSCAN (without Cenospheres)**
Al and Si	87.6	54.1	81.8	59
Iron Oxides	3.6	1.1	2.7	-
Anorthite	-	1.5	1.3	-
Rutile	-	0.1	ND	-
Species (PS B)	**XRF**	**XRD**	**QEMSCAN**	**QEMSCAN (without Cenospheres)**
Al and Si	85.7	46.2	82.5	61.3
Iron Oxides	6.5	5	5.6	-
Anorthite	-	0.7	0.3	-
Rutile	-	0.1	ND	-
Species (PS C)	**XRF**	**XRD**	**QEMSCAN**	**QEMSCAN (without Cenospheres)**
Al and Si	84.3	44.4	75.2	53.5
Fe	5.5	4.4	5.6	-
Anorthite	-	0.9	1.3	-
Rutile	-	ND	ND	-

ND – Not Detected

XRD analysis uses elastic scattering of X-Rays to characterise the crystallographic structure of minerals and as a result cannot characterise non-crystalline structures (Ayling *et al.,* 2012). To account for this limitation, QEMSCAN minerals containing Al and Si were summed again, this time omitting amorphous content like glass cenospheres. This yielded an acceptable correlation for PS A and PS C, with PS B showing a larger deviation between the analytical methods, varying by as much as 25%. For iron oxides, an acceptable comparison was shown between XRF and QEMSCAN, with XRD underestimating the Fe content. This discrepancy can once again be attributed to the inability of XRD analysis to

detect amorphous content, with QEMSCAN analysis indicating the presence of Fe as glass cenospheres.

Appendix H: Bickelhaupt Correlation

The Bickelhaupt prediction technique (Bickelhaupt, 1974, Bickelhaupt, 1975 & Bickelhaupt, 1979) considers the surface resistivity, ρ_s, and volume resistivity, ρ_v, separately, combining the two to yield the total resistivity, ρ_{sv}. A detailed description of the Bickelhaupt prediction technique follows below, using ash sample PS A as example:

a. Adapting Input Data

Raw XRF data is give as oxides in weight percentage, these oxides need to be converted to atomic concentrations. The XRF data is firstly normalized, followed by dividing each oxide by its molecular weight to obtain the mole fraction of the individual oxides. The mole fractions are subsequently normalised to yield a mole percentage. Lastly the mole percentage of each oxide is multiplied by their respective cationic fraction to yield the atomic concentration of the cations, as shown in Table H-1.

Table H-1: Atomic concentration of cations (wt%)

Oxides	Determined	Normalized	Molecular Weight	Mole Fraction	Molecular Percentage	Cation Fraction	Atomic Concentration
Al_2O_3	30.2	30.4	102.0	0.3	21.1	0.4	8.4
CaO	4.3	4.3	56.1	0.1	5.5	0.5	2.7
Cr_2O_3	0.0	0.0	152.0	0.0	0.0	0.4	0.0
Fe_2O_3	3.6	3.6	159.7	0.0	1.6	0.4	0.6
K_2O	0.7	0.7	94.2	0.0	0.5	0.7	0.3
MgO	1.0	1.0	40.3	0.0	1.7	0.5	0.9
MnO	0.0	0.0	70.9	0.0	0.0	0.5	0.0
Na_2O	0.4	0.4	62.0	0.0	0.4	0.7	0.3
P_2O_5	0.3	0.3	141.9	0.0	0.2	0.3	0.0
SiO_2	56.8	57.2	60.1	1.0	67.3	0.3	22.4
TiO_2	1.5	1.5	79.9	0.0	1.3	0.3	0.4
V_2O_5	0.0	0.0	181.9	0.0	0.0	0.3	0.0
ZrO_2	0.1	0.1	123.2	0.0	0.0	0.3	0.0
BaO	0.1	0.1	153.3	0.0	0.0	0.5	0.0
SrO	0.1	0.1	103.6	0.0	0.1	0.5	0.0
ZnO	0.0	0.0	81.4	0.0	0.0	0.5	0.0
SO_3	0.3	0.3	80.1	0.0	0.2	0.3	0.1
Sum	**99.4**	**100.0**	**---**	**1.4**	**100.0**	**---**	**36.3**

b. Calculate Volume Resistivity, ρ_v

Eq. H-1 is used to calculate the volume resistivity at 352°C and an electric field strength of 2 kV/cm.

$$\log \rho_{v,\ 352℃} = 8.9434 - (1.8916 \log x) - (\ 0.9696 \log y) + \left(1.2370\ (\log z - \log 2.5)\right) \quad \text{(H-1)}$$

For sample PS A, log $\rho_{v,\ 352°C}$ = 10,797

The value calculated from Eq. H-1 can now be used to calculate log $\rho_{v\,0}$, a complex material parameter which takes into account the number of mobile charge carriers, at 352°C.

$$\log \rho_{v\,0} = \log \rho_v - \left(\left(\frac{\theta}{k}\right) \log e\right) \left(\frac{1}{T}\right) \quad \text{(H-2)}$$

For sample PS A, log $\rho_{v\,0}$ = 3.802

With $\rho_{v\,0}$ known, Eq. H-2 can be used to calculate the volume resistivity over the remainder of temperature range.

c. Calculate Surface Resistivity, ρ_s

The surface resistivity can next be calculated. The surface resistivity is firstly calculated at two temperature points, namely; 84°C and 112°C. The experimental resistivity data of American ashes as a function of lithium and sodium concentrations are shown in Figure H-1 and Figure H-2. With the lithium and sodium atomic concentration known, both resistivity points can be calculated.

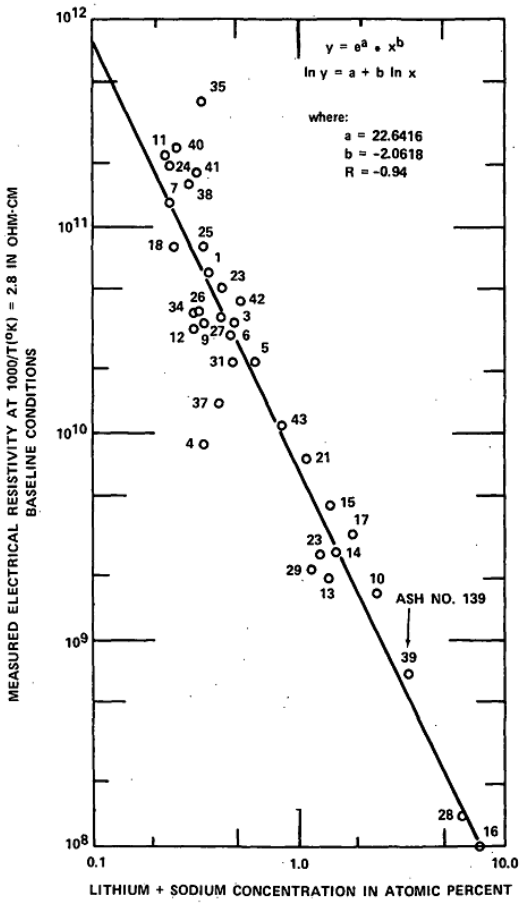


Figure H-1: Resistivity as a function of Li + Na concentration at 84°C (Taken from: Bickelhaupt, 1979)

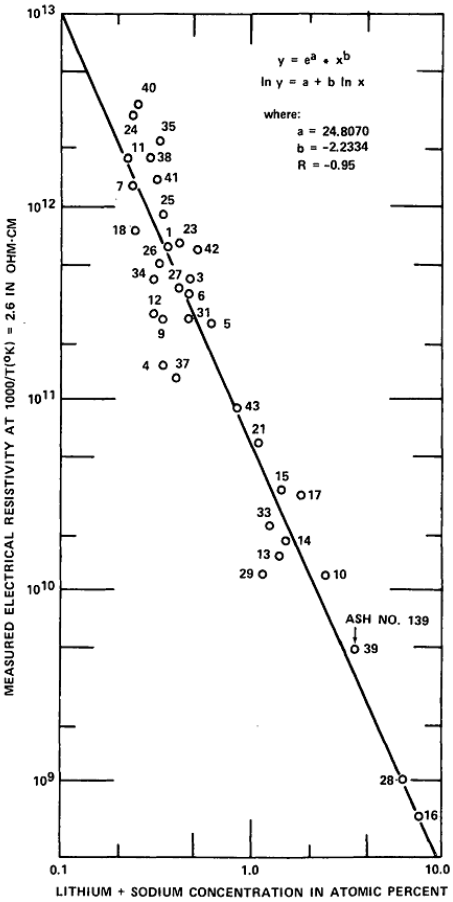


Figure H-2: Resistivity as a function of Li + Na concentration at 112°C (Taken from: Bickelhaupt, 1979)

For sample PS A, $\rho_{s\ 84°C}$ = 1.031 x 10^{11} Ω cm and $\rho_{s\ 112°C}$ = 1.127 x 10^{12} Ω cm at the baseline conditions of 9 vol% ambient moisture and a field strength of 2 kV/cm.

The graphical method shown in Figure H-1 and Figure H-2 was further developed for 144, 182, 227 and 352°C, but proved increasingly ineffective at predicating surface resistivity as the temperature increased. As a results, at higher temperatures Eq. H-3 was used to predict resistivity.

$$\rho_s = \rho_{s0}\, e^{-W\, K_0\, e^{\left(\frac{K_1}{T}\right)}} \qquad \text{(H-3)}$$

Eq. H-3 was subsequently written in logarithmic form.

$$\log \rho_s = \log \rho_{s0} - \left(\log e\ \ K_0\, e^{\left(\frac{K_1}{T}\right)}\right) W \qquad \text{(H-4)}$$

The previously determined resistivity value at 84°C, $\rho_{s\ 84°C}$, can now be used to calculate ρ_{s0} at the baseline condition of 9 vol% ambient moisture.

For sample PS A, ρ_{s0} = 1.358 ×10^{12} Ω cm

With ρ_{s0} know, Eq. H-3 can be used to determine the surface resistivity over the remainder of the temperature range.

As stated in IEEE std. 548 of 1984; all measurement of resistivity as a function of temperature shall be carried out at 4 kV/cm. Eq. H-5 is used to correct previously determined resistivity values from a baseline field strength of 2 kV/cm to the 4 kV/cm used for this study.

$$\log \rho_E = \log \rho_B + (E + E_B) S_e \qquad \text{(H-5)}$$

Similarly, Eq. H-6 can be used to correct the baseline moisture content from 9 vol% to 6 vol% ambient moisture used for this example calculation.

$$\log \rho_s = \log \rho_{sB} + (C_W - C_B)\, S_W \qquad \text{(E-6)}$$

d. Calculate Combined Resistivity, ρ_{vs}

Seeing as though this study does not consider acid resistivity, only surface and volume resistivity was combined. Eq. H-7 is used to sum the surface resistivity and volume resistivity as parallel resistances.

$$\rho_{vs} = \frac{\rho_v \, \rho_s}{\rho_v + \rho_s} \qquad \text{(H-7)}$$

For sample PS A, Table J-10 and Figure J-11 shows the calculated combined resistivity at a field strength of 4 kV/cm and 6 vol% ambient moisture.

Appendix I: Modified Bickelhaupt Model

Modifications were made to both the volume and surface resistivity term. The volume resistivity term was firstly modified to eliminate the large deviation between the standard model and experimental values. The volume resistivity term originally set forth by Bickelhaupt (1979) is shown by Eq. I-1:

$$\log \rho_v = \log \rho_{v\,0} + \left(\left(\frac{\theta}{k}\right) \log e\right) \left(\frac{1}{T}\right) \quad \text{(I-1)}$$

This term describes the log of resistivity as function of temperature and required as input the complex material parameter, log $\rho_{v,\,0}$, and the experimental activation energy, θ, both of which were originally determined from the experimental data of American ashes. Log $\rho_{v,\,0}$, the complex material property, is a function of the ash composition and can be calculated using Eq. I-2.

$$\log \rho_{v,\ 352^{\circ}C} = 8.9434 - (1.8916\,[Na]) - (0.9696 \log\,[Fe]) + \big(1.2370\,(\log\,[Mg + Ca] - \log 2.5)\big) \quad \text{(I-2)}$$

Placing both Eq. I-1 and I-2 in Excel, the weights assigned to Eq. I-2 and the experimental activation energy in Eq. I-1 were changed to minimize the error between predicted and experimental values, using the least square method. Table I-1 shows both the original values determined by Bickelhaupt and the modified values for the three ash samples.

Table I-1: Modified values to improve volume resistivity term of the Bickelhaupt model

Modified Parameter	Bickelhaupt Constants	Modified Values			
		PS A	PS B	PS C	Average
Weight 1	8.9434	8.3306	8.3645	8.4361	8.3771
Weight 2	1.8916	1.5409	0.9450	1.2123	1.2327
Weight 3	0.9696	1.2382	1.1665	1.2432	1.2160
Weight 4	1.2370	0.6501	0.6694	0.7529	0.6908
Weight 5	2.5	2.6051	2.5971	2.5899	2.5974
Activation Energy	0.86	1.1719	1.0875	1.0307	1.0967

Using the average of the values shown in Table I-1, Eq. I-1 and I-2 can be rewritten to better predict the volume resistivity of South African fly ashes.

$$\log \rho_v = \log \rho_{v\,0} + \left(\left(\frac{0.85}{k}\right) \log e\right) \left(\frac{1}{T}\right) \quad \text{(I-3)}$$

$$\log \rho_{v,\ 352^{\circ}C} = 8.3771 - (1.2327\ [Na]) - (\ 1.2160 \log[Fe]) + \left(0.6908\ (\log[Mg + Ca] - \log 2.6)\right) \quad \text{(I-4)}$$

The modifications to the volume resistivity term allowed the Bickelhaupt model to better predict the resistivity values of South African ashes, however the volume corrected model still proved ineffective at predicting the effect moisture has on South African ashes. To address the error between the predicted and experimental data in the surface resistivity region, the surface resistivity term of the Bickelhaupt model was also modified.

Eq. I-5 describes the log of surface resistivity as a function of temperature and requires as input log ρ_{s0}.

$$\log \rho_s = \log \rho_{s0} - \left(\log e\ K_0\ e^{\left(\frac{K_1}{T}\right)}\right) W \quad \text{(I-5)}$$

Log ρ_{s0} is the maximum surface resistivity as the effect of moisture approaches zero at high temperatures and is a function of the sodium concentration. The Bickelhaupt model uses graphs such as those depicted in Figure H-1 to predict resistivity for a certain sodium concentration, x. Figure H-1 can alternatively be represented by Eq. I-6.

$$\log \rho_{s,\ 84^{\circ}C} = e^{22.6416}\ x^{-2.0618} \quad \text{(I-6)}$$

Placing both Eq. I-5 and I-6 in Excel, the constants assigned to Eq. I-6 were changed to minimize the error between predicted and experimental values, using the least square method. Table I-2 shows both the original values determined by Bickelhaupt and the modified values for the three ash samples.

Table I-2: Modified values to improve surface resistivity term of the Bickelhaupt model

Modified Parameter	Bickelhaupt Constants	Modified Values
Constant A	22.6416	25.8948
Constant B	-2.0618	-0.4267

Using the average values shown in Table I-2, Eq. F-6 can be rewritten to better predict the surface resistivity of South African fly ashes.

$$\log \rho_{s,\ 84^{\circ}C} = e^{25.8948}\ x^{-0.4267} \quad \text{(F-7)}$$

When considering the modifications to the Bickelhaupt model, only experimental constant were changed. No changes were made to correction factors, such as those used to correct moisture or electric field stretch, as these correction factors are not dependent on ash

composition. Furthermore, constant such as K_0 and K_1 are also left unchanged as they describe the physical and chemical properties of water vapour and are unlikely to be influenced by ash composition.

Appendix J: Resistivity Curves and Error Ratios

a. Experimental Resistivity Data

In this section, the resistivity as a function of temperature and the experimentally determined resistivity data is presented for dry, 4.6, 6.0 and 9.0 vol% ambient moisture.

i. Resistivity Data at Dry Ambient Conditions

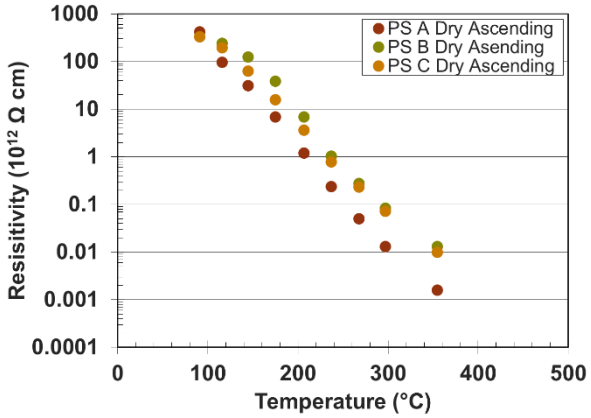


Figure J-1: Ascending resistivity as a function of temperature for PS A, B & C at dry ambient conditions

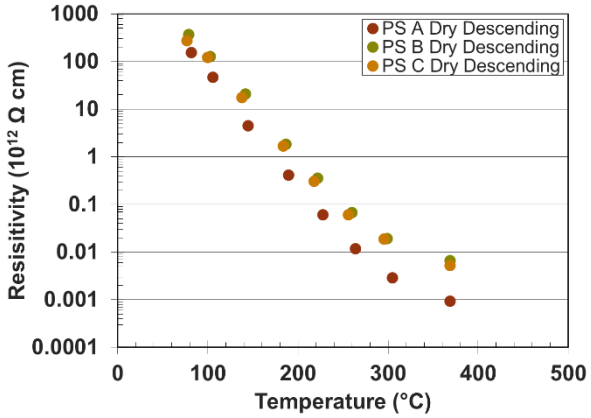


Figure J-2: Descending resistivity as a function of temperature for PS A, B & C at dry ambient conditions

Table J-1: Experimental resistivity data at dry ambient conditions

PS A Ascending Data		PS B Ascending Data		PS C Ascending Data	
Temperature (°C)	**Resistivity (Ω cm)**	**Temperature (°C)**	**Resistivity (Ω cm)**	**Temperature (°C)**	**Resistivity (Ω cm)**
91	4.2E+14	91	3.3E+14	91	3.3E+14
116	9.6E+13	116	2.4E+14	116	1.9E+14
145	3.1E+13	145	1.2E+14	145	6.3E+13
175	6.8E+12	175	3.8E+13	175	1.6E+13
207	1.2E+12	207	6.8E+12	207	3.6E+12
237	2.4E+11	237	1.0E+12	237	7.7E+11
268	5.0E+10	268	2.7E+11	268	2.3E+11
297	1.3E+10	297	8.3E+10	297	7.1E+10
355	1.6E+09	355	1.3E+10	355	9.8E+09
Descending Data		**Descending Data**		**Descending Data**	
Temperature (°C)	**Resistivity (Ω cm)**	**Temperature (°C)**	**Resistivity (Ω cm)**	**Temperature (°C)**	**Resistivity (Ω cm)**
82	1.5E+14	79	3.7E+14	77	2.7E+14
106	4.7E+13	103	1.3E+14	100	1.2E+14
145	4.4E+12	142	2.1E+13	138	1.7E+13
190	4.1E+11	187	1.8E+12	184	1.7E+12
228	6.0E+10	222	3.5E+11	218	3.0E+11
264	1.2E+10	260	6.7E+10	256	6.1E+10
305	2.8E+09	299	1.9E+10	296	1.9E+10
369	9.2E+08	369	6.5E+09	369	5.2E+09

ii. Resistivity Data at 4.6 vol% Ambient Moisture

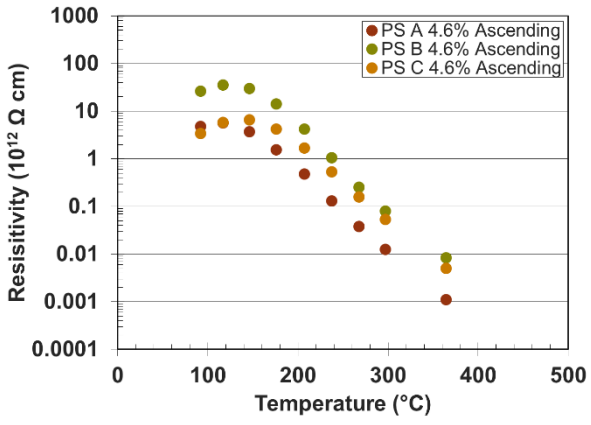


Figure J-3: Ascending resistivity as a function of temperature for PS A, B & C at 4.6 vol% ambient moisture.

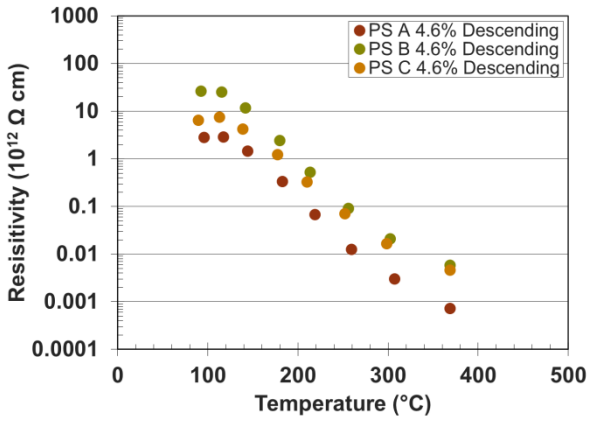


Figure J-4: Descending resistivity as a function of temperature for PS A, B & C at 4.6 vol% ambient moisture.

Table J-2: Experimental resistivity data at 4.6 vol% ambient moisture

PS A		PS B		PS C	
Ascending Data		**Ascending Data**		**Ascending Data**	
Temperature (°C)	**Resistivity (Ω cm)**	**Temperature (°C)**	**Resistivity (Ω cm)**	**Temperature (°C)**	**Resistivity (Ω cm)**
92	4.7E+12	92	2.6E+13	92	3.4E+12
117	5.6E+12	117	3.5E+13	117	5.7E+12
147	3.7E+12	147	3.0E+13	147	6.5E+12
176	1.5E+12	176	1.4E+13	176	4.2E+12
208	4.8E+11	208	4.2E+12	208	1.7E+12
238	1.3E+11	238	1.1E+12	238	5.3E+11
268	3.8E+10	268	2.5E+11	268	1.6E+11
297	1.2E+10	297	7.9E+10	297	5.3E+10
365	1.1E+09	365	8.3E+09	365	5.0E+09
Descending Data		**Descending Data**		**Descending Data**	
Temperature (°C)	**Resistivity (Ω cm)**	**Temperature (°C)**	**Resistivity (Ω cm)**	**Temperature (°C)**	**Resistivity (Ω cm)**
96	2.8E+12	93	2.6E+13	90	6.4E+12
118	2.8E+12	116	2.5E+13	113	7.4E+12
145	1.4E+12	142	1.2E+13	139	4.2E+12
183	3.3E+11	180	2.4E+12	178	1.2E+12
219	6.6E+10	214	5.1E+11	211	3.2E+11
260	1.3E+10	256	9.0E+10	253	6.9E+10
308	3.0E+09	303	2.1E+10	299	1.6E+10
369	7.2E+08	369	5.8E+09	369	4.5E+09

iii. Resistivity Data at 6.0 vol% Ambient Moisture

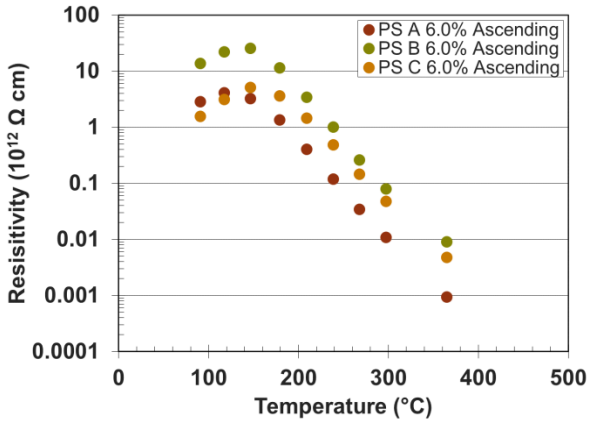


Figure J-5: Ascending resistivity as a function of temperature for PS A, B & C at 6.0 vol% ambient moisture.

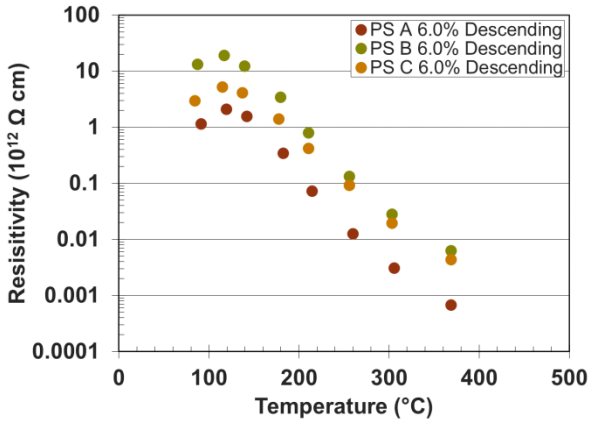


Figure J-6: Descending resistivity as a function of temperature for PS A, B & C at 6.0 vol% ambient moisture.

Table J-3: Experimental resistivity data at 6.0 vol% ambient moisture

PS A		PS B		PS C	
Ascending Data		**Ascending Data**		**Ascending Data**	
Temperature (°C)	**Resistivity (Ω cm)**	**Temperature (°C)**	**Resistivity (Ω cm)**	**Temperature (°C)**	**Resistivity (Ω cm)**
91	2.8E+12	91	1.4E+13	91	1.5E+12
118	4.1E+12	118	2.2E+13	118	3.1E+12
147	3.2E+12	147	2.5E+13	147	5.1E+12
180	1.3E+12	180	1.1E+13	180	3.6E+12
210	4.0E+11	210	3.4E+12	210	1.4E+12
239	1.2E+11	239	1.0E+12	239	4.8E+11
268	3.4E+10	268	2.6E+11	268	1.4E+11
298	1.1E+10	298	7.9E+10	298	4.8E+10
365	9.3E+08	365	9.0E+09	365	4.8E+09
Descending Data		**Descending Data**		**Descending Data**	
Temperature (°C)	**Resistivity (Ω cm)**	**Temperature (°C)**	**Resistivity (Ω cm)**	**Temperature (°C)**	**Resistivity (Ω cm)**
92	1.1E+12	88	1.3E+13	85	2.9E+12
120	2.1E+12	117	1.9E+13	115	5.2E+12
143	1.5E+12	140	1.2E+13	138	4.1E+12
183	3.4E+11	180	3.4E+12	178	1.4E+12
215	7.2E+10	211	7.9E+11	211	4.1E+11
260	1.3E+10	256	1.3E+11	256	9.1E+10
306	3.1E+09	304	2.8E+10	304	1.9E+10
369	6.7E+08	369	6.3E+09	369	4.3E+09

iv. Resistivity Data at 9.0 vol% Ambient Moisture

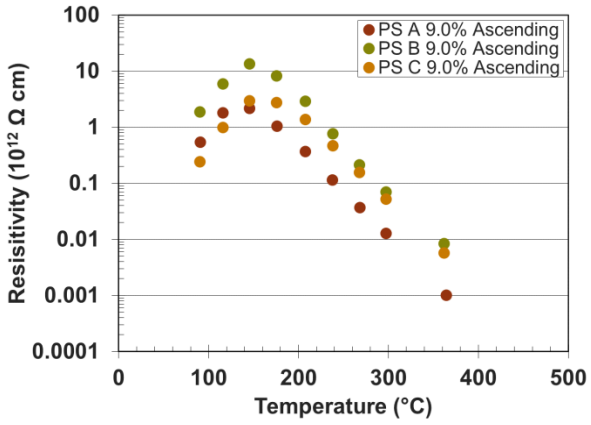


Figure J-7: Ascending resistivity as a function of temperature for PS A, B & C at 9.0 vol% ambient moisture.

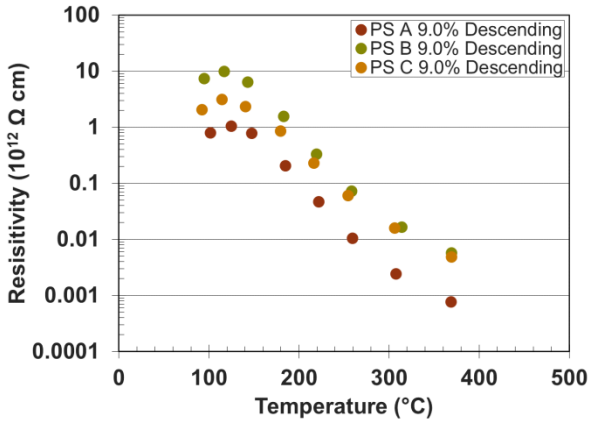


Figure J-8: Descending resistivity as a function of temperature for PS A, B & C at 9.0 vol% ambient moisture.

Table J-4: Experimental resistivity data at 9.0 vol% ambient moisture

PS A		PS B		PS C	
Ascending Data		**Ascending Data**		**Ascending Data**	
Temperature (°C)	**Resistivity (Ω cm)**	**Temperature (°C)**	**Resistivity (Ω cm)**	**Temperature (°C)**	**Resistivity (Ω cm)**
91	4.3E+11	91	1.5E+12	91	1.9E+11
116	1.4E+12	116	4.7E+12	116	7.9E+11
146	1.7E+12	146	1.1E+13	146	2.4E+12
177	8.3E+11	176	6.5E+12	176	2.2E+12
208	3.0E+11	208	2.3E+12	208	1.1E+12
238	9.1E+10	239	6.0E+11	239	3.7E+11
269	2.9E+10	268	1.7E+11	268	1.2E+11
298	1.0E+10	298	5.5E+10	298	4.2E+10
365	8.1E+08	362	6.7E+09	362	4.6E+09
Descending Data		**Descending Data**		**Descending Data**	
Temperature (°C)	**Resistivity (Ω cm)**	**Temperature (°C)**	**Resistivity (Ω cm)**	**Temperature (°C)**	**Resistivity (Ω cm)**
102	6.3E+11	95	5.9E+12	93	1.6E+12
125	8.3E+11	117	7.8E+12	115	2.5E+12
148	6.2E+11	144	5.1E+12	141	1.9E+12
185	1.6E+11	183	1.2E+12	180	6.8E+11
222	3.7E+10	220	2.6E+11	217	1.8E+11
260	8.3E+09	259	5.7E+10	255	4.8E+10
308	1.9E+09	315	1.3E+10	307	1.3E+10
369	6.1E+08	370	4.5E+09	370	3.9E+09

The percentage reduction in resistivity relative to dry ambient conditions is presented in Table J-4 for 4.6, 6.0 and 9.0 vol% ambient moisture.

Table J-5: Percentage reduction relative to dry ambient conditions

90 ºC			
Moisture Content	**PS A**	**PS B**	**PS C**
4.6%	98.9%	92.2%	99.0%
6%	99.3%	95.9%	99.5%
9%	99.9%	99.4%	99.9%
120 ºC			
Moisture Content	**PS A**	**PS B**	**PS C**
4.6%	94.1%	85.1%	97.0%
6%	95.7%	90.8%	98.4%
9%	98.1%	97.5%	99.5%
150 ºC			
Moisture Content	**PS A**	**PS B**	**PS C**
4.6%	88.1%	76.2%	89.5%
6%	89.6%	79.5%	91.9%
9%	93.1%	89.2%	95.3%
180 ºC			
Moisture Content	**PS A**	**PS B**	**PS C**
4.6%	77.2%	62.9%	73.2%
6%	80.2%	70.0%	77.1%
9%	84.7%	78.6%	82.4%
210 ºC			
Moisture Content	**PS A**	**PS B**	**PS C**
4.6%	59.9%	38.0%	54.0%
6%	66.3%	49.5%	59.9%
9%	69.1%	57.6%	62.4%

b. Standard Bickelhaupt Model

In this section the results of the Bickelhaupt model are presented and includes the resistivity as a function of temperature and the determined resistivity data for dry, 4.6, 6.0 and 9.0 vol% ambient moisture. This section also includes the deviations between the standard Bickelhaupt model and the experimentally determined resistivity.

i. Resistivity Data at Dry Ambient Conditions

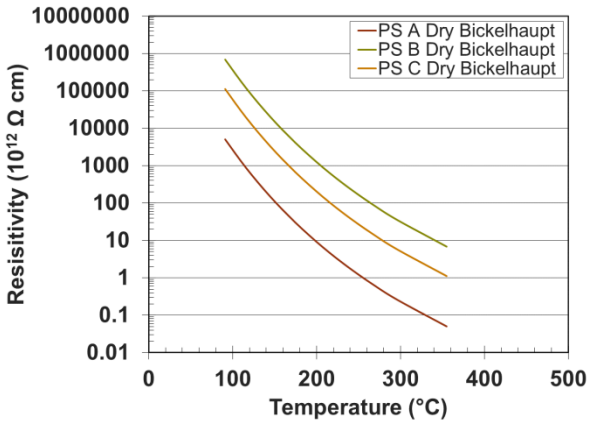


Figure J-9: Standard Bickelhaupt model resistivity as a function of temperature for PS A, B & C at dry ambient conditions

Table J-6: Standard Bickelhaupt resistivity data at dry ambient conditions

PS A		PS B		PS C	
Temperature (°C)	**Resistivity (Ω cm)**	**Temperature (°C)**	**Resistivity (Ω cm)**	**Temperature (°C)**	**Resistivity (Ω cm)**
91	5.1E+15	91	6.9E+17	91	1.1E+17
116	8.7E+14	116	1.2E+17	116	1.9E+16
145	1.5E+14	145	2.0E+16	145	3.3E+15
175	3.0E+13	175	4.1E+15	175	6.6E+14
207	6.7E+12	207	9.2E+14	207	1.5E+14
237	2.0E+12	237	2.7E+14	237	4.4E+13
268	6.5E+11	268	8.8E+13	268	1.4E+13
297	2.5E+11	297	3.5E+13	297	5.6E+12
355	5.0E+10	355	6.9E+12	355	1.1E+12

Table J-7: Resistivity error ratio for standard Bickelhaupt model at dry ambient conditions

PS A		PS B		PS C	
Measurement	**Error Ratio**	**Measurement**	**Error Ratio**	**Measurement**	**Error Ratio**
1	12.0	1	2081.2	1	338.0
2	9.1	2	499.6	2	99.8
3	4.7	3	161.2	3	52.1
4	4.4	4	106.3	4	42.2
5	5.6	5	135.3	5	41.5
6	8.4	6	263.4	6	57.2
7	13.0	7	322.6	7	62.7
8	19.7	8	414.2	8	79.6
9	32.1	9	527.0	9	113.9

ii. Resistivity Data at 4.6 vol% Ambient Moisture

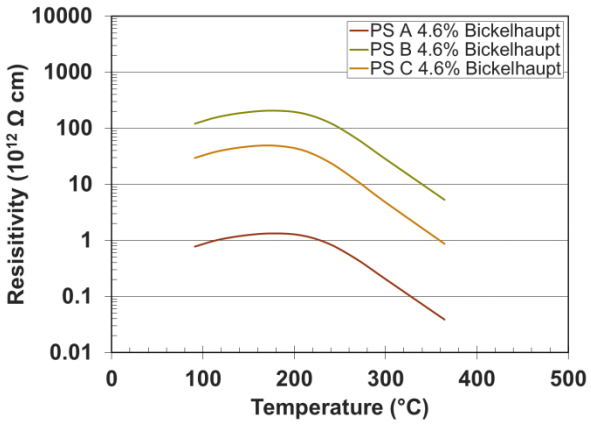


Figure J-10: Standard Bickelhaupt model resistivity as a function of temperature for PS A, B & C at 4.6 vol% ambient moisture

Table J-8: Standard Bickelhaupt resistivity data at 4.6 vol% ambient moisture

PS A		PS B		PS C	
Temperature (°C)	**Resistivity (Ω cm)**	**Temperature (°C)**	**Resistivity (Ω cm)**	**Temperature (°C)**	**Resistivity (Ω cm)**
91	7.8E+11	91	1.2E+14	91	3.0E+13
116	1.0E+12	116	1.6E+14	116	3.9E+13
146	1.2E+12	146	1.9E+14	146	4.7E+13
177	1.3E+12	177	2.1E+14	177	4.9E+13
208	1.2E+12	208	1.9E+14	208	4.1E+13
238	8.7E+11	238	1.3E+14	238	2.5E+13
269	4.6E+11	269	6.5E+13	269	1.2E+13
298	2.2E+11	298	3.0E+13	298	5.1E+12
364.5	3.9E+10	364.5	5.3E+12	364.5	8.7E+11

Table J-9: Resistivity error ratio for standard Bickelhaupt model at 4.6 vol% ambient moisture

PS A		PS B		PS C	
Measurement	**Error Ratio**	**Measurement**	**Error Ratio**	**Measurement**	**Error Ratio**
1	1.5	1	64.7	1	124.0
2	1.8	2	27.0	2	39.3
3	1.7	3	14.3	3	15.9
4	1.3	4	25.4	4	17.9
5	3.3	5	64.8	5	30.5
6	7.7	6	168.6	6	53.8
7	12.6	7	305.2	7	74.4
8	17.2	8	436.1	8	97.8
9	38.4	9	638.2	9	152.1

iii. Resistivity Data at 6.0 vol% Ambient Moisture

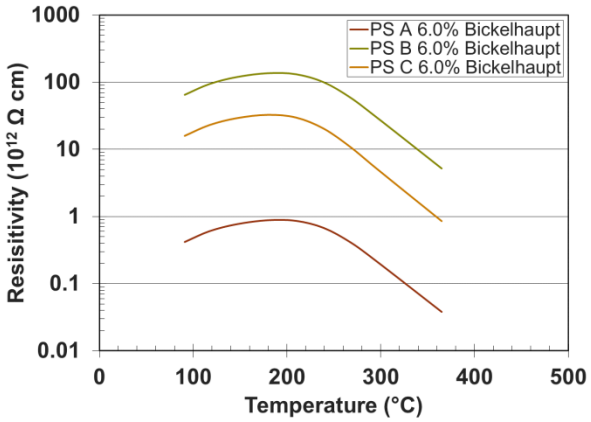


Figure J-11: Standard Bickelhaupt model resistivity as a function of temperature for PS A, B & C at 6.0 vol% ambient moisture

Table J-10: Standard Bickelhaupt resistivity data at 6.0 vol% ambient moisture

PS A		PS B		PS C	
Temperature (°C)	**Resistivity (Ω cm)**	**Temperature (°C)**	**Resistivity (Ω cm)**	**Temperature (°C)**	**Resistivity (Ω cm)**
91	4.2E+11	91	6.5E+13	91	1.6E+13
118	6.1E+11	118	9.4E+13	118	2.3E+13
147	7.7E+11	147	1.2E+14	147	2.9E+13
180	8.8E+11	180	1.4E+14	180	3.3E+13
210	8.6E+11	210	1.3E+14	210	3.0E+13
239	6.8E+11	239	1.0E+14	239	2.0E+13
268	4.1E+11	268	5.9E+13	268	1.1E+13
298	2.1E+11	298	2.9E+13	298	4.9E+12
365	3.8E+10	365	5.2E+12	365	8.5E+11

Table J-11: Resistivity error ratio for standard Bickelhaupt model at 6.0 vol% ambient moisture

PS A		PS B		PS C	
Measurement	**Error Ratio**	**Measurement**	**Error Ratio**	**Measurement**	**Error Ratio**
1	6.7	1	4.7	1	10.3
2	6.8	2	4.3	2	7.4
3	4.2	3	4.7	3	5.8
4	1.5	4	11.9	4	9.1
5	2.1	5	38.4	5	20.6
6	5.7	6	100.3	6	42.2
7	12.1	7	225.2	7	74.9
8	19.1	8	362.4	8	103.1
9	40.8	9	575.4	9	178.9

iv. Resistivity Data at 9.0 vol % Ambient Moisture

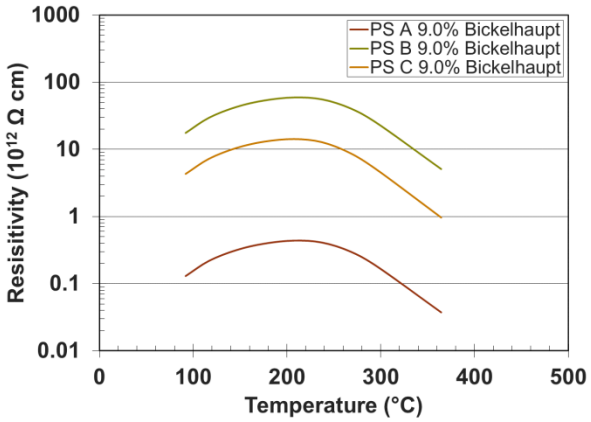


Figure J-12: Standard Bickelhaupt model resistivity as a function of temperature for PS A, B & C at 9.0 vol% ambient moisture

Table J-12: Standard Bickelhaupt resistivity data at 9.0 vol% ambient moisture

PS A		PS B		PS C	
Temperature (°C)	**Resistivity (Ω cm)**	**Temperature (°C)**	**Resistivity (Ω cm)**	**Temperature (°C)**	**Resistivity (Ω cm)**
92	1.3E+11	92	1.8E+13	92	4.3E+12
117	2.2E+11	117	3.0E+13	117	7.3E+12
147	3.2E+11	147	4.3E+13	147	1.1E+13
176	4.0E+11	176	5.4E+13	176	1.3E+13
208	4.4E+11	208	5.9E+13	208	1.4E+13
238	4.1E+11	238	5.6E+13	238	1.3E+13
268	3.0E+11	268	4.1E+13	268	8.7E+12
297	1.8E+11	297	2.4E+13	297	4.8E+12
364.5	3.7E+10	364.5	5.1E+12	364.5	9.7E+11

Table J-13: Resistivity error ratio for standard Bickelhaupt model at 9.0 vol% ambient moisture

PS A		PS B		PS C	
Measurement	**Error Ratio**	**Measurement**	**Error Ratio**	**Measurement**	**Error Ratio**
1	36.2	1	1.5	1	1.3
2	25.6	2	1.2	2	1.3
3	11.7	3	1.5	3	1.6
4	3.9	4	3.8	4	3.1
5	1.1	5	14.1	5	8.6
6	3.1	6	52.8	6	24.0
7	7.9	7	162.0	7	56.1
8	14.3	8	305.6	8	91.1
9	34.4	9	610.5	9	193.5

c. Volume Corrected Bickelhaupt Model

In this section the results of the volume corrected Bickelhaupt model are presented and includes the resistivity as a function of temperature and the determined resistivity data for dry, 4.6, 6.0 and 9.0 vol% ambient moisture. This section also include the deviations between the volume corrected Bickelhaupt model and the experimentally determined resistivity.

i. Resistivity Data at Dry Ambient Conditions

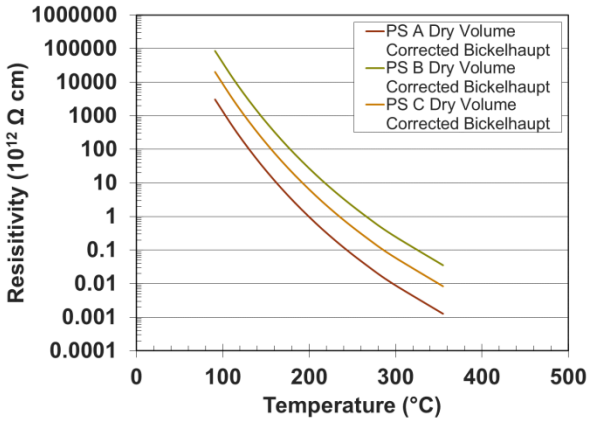


Figure J-13: Volume corrected Bickelhaupt model resistivity as a function of temperature for PS A, B & C at dry ambient conditions

Table J-14: Volume corrected Bickelhaupt resistivity data at dry ambient conditions

PS A		PS B		PS C	
Temperature (°C)	**Resistivity (Ω cm)**	**Temperature (°C)**	**Resistivity (Ω cm)**	**Temperature (°C)**	**Resistivity (Ω cm)**
91	3.1E+15	91	8.6E+16	91	2.0E+16
116	3.2E+14	116	9.1E+15	116	2.1E+15
145	3.4E+13	145	9.4E+14	145	2.2E+14
175	4.4E+12	175	1.2E+14	175	2.9E+13
207	6.6E+11	207	1.8E+13	207	4.3E+12
237	1.4E+11	237	3.9E+12	237	9.1E+11
268	3.3E+10	268	9.2E+11	268	2.2E+11
297	1.0E+10	297	2.8E+11	297	6.6E+10
355	1.3E+09	355	3.5E+10	355	8.4E+09

Table J-15: Resistivity error ratio for volume corrected Bickelhaupt model at dry ambient conditions

PS A		PS B		PS C	
Measurement	**Error Ratio**	**Measurement**	**Error Ratio**	**Measurement**	**Error Ratio**
1	7.3	1	258.4	1	60.9
2	3.4	2	38.1	2	11.0
3		3	7.5	3	3.5
4	1.6	4	3.2	4	1.8
5	1.8	5	2.7	5	1.2
6	1.7	6	3.7	6	1.2
7	1.5	7	3.4	7	1.1
8	1.3	8	3.3	8	1.1
9	1.2	9	2.7	9	1.2

ii. Resistivity Data at 4.6 vol % Ambient Moisture

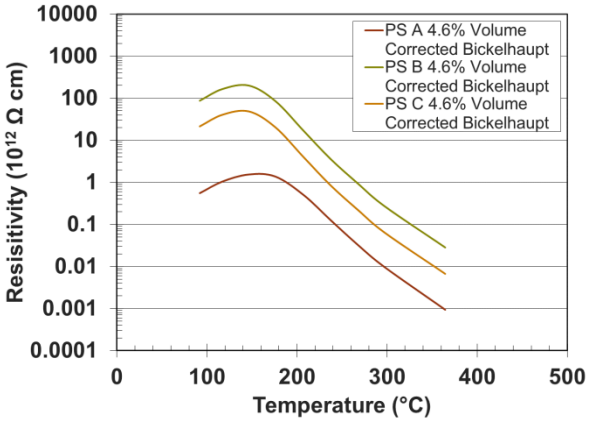


Figure J-14: Volume corrected Bickelhaupt model resistivity as a function of temperature for PS A, B & C at 4.6 vol% ambient moisture

Table J-16: Volume corrected Bickelhaupt resistivity data at 4.6 vol% ambient moisture

PS A		PS B		PS C	
Temperature (°C)	**Resistivity (Ω cm)**	**Temperature (°C)**	**Resistivity (Ω cm)**	**Temperature (°C)**	**Resistivity (Ω cm)**
92	5.5E+11	92	8.7E+13	92	2.1E+13
117	1.0E+12	117	1.7E+14	117	4.0E+13
147	1.5E+12	147	2.0E+14	147	4.9E+13
176	1.4E+12	176	8.5E+13	176	2.0E+13
208	5.0E+11	208	1.7E+13	208	3.9E+12
238	1.3E+11	238	3.6E+12	238	8.4E+11
268	3.2E+10	268	9.2E+11	268	2.2E+11
297	9.8E+09	297	2.7E+11	297	6.4E+10
365	9.4E+08	365	2.8E+10	365	6.7E+09

Table J-17: Resistivity error ratio for volume corrected Bickelhaupt model at 4.6 vol% ambient moisture

PS A		PS B		PS C	
Measurement	**Error Ratio**	**Measurement**	**Error Ratio**	**Measurement**	**Error Ratio**
1	8.5	1	3.4	1	6.3
2	5.4	2	4.7	2	7.1
3	2.4	3	6.8	3	7.4
4	0.9	4	6.0	4	4.8
5	1.0	5	3.9	5	2.4
6	1.0	6	3.4	6	1.6
7	1.2	7	3.7	7	1.4
8	1.3	8	3.5	8	1.2
9	0.9	9	3.4	9	1.3

iii. Resistivity Data at 6.0 vol % Ambient Moisture

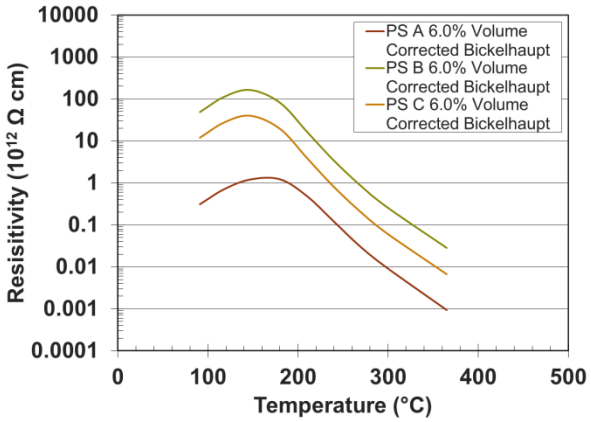


Figure J-15: Volume corrected Bickelhaupt model resistivity as a function of temperature for PS A, B & C at 6.0 vol% ambient moisture

Table J-18: Volume corrected Bickelhaupt resistivity data at 6.0 vol% ambient moisture

PS A		PS B		PS C	
Temperature (°C)	**Resistivity (Ω cm)**	**Temperature (°C)**	**Resistivity (Ω cm)**	**Temperature (°C)**	**Resistivity (Ω cm)**
91	3.1E+11	91	4.9E+13	91	1.2E+13
118	7.1E+11	118	1.1E+14	118	2.8E+13
147	1.2E+12	147	1.6E+14	147	4.0E+13
180	1.2E+12	180	8.1E+13	180	1.9E+13
210	4.8E+11	210	1.7E+13	210	3.9E+12
239	1.2E+11	239	3.5E+12	239	8.4E+11
268	3.2E+10	268	9.2E+11	268	2.2E+11
298	9.8E+09	298	2.7E+11	298	6.4E+10
365	9.4E+08	365	2.8E+10	365	6.7E+09

Table J-19: Resistivity error ratio for volume corrected Bickelhaupt model at 6.0 vol% ambient moisture

PS A		PS B		PS C	
Measurement	**Error Ratio**	**Measurement**	**Error Ratio**	**Measurement**	**Error Ratio**
1	9.1	1	3.6	1	7.7
2	5.8	2	5.1	2	8.9
3	2.7	3	6.5	3	7.9
4	0.9	4	7.1	4	5.4
5	1.2	5	4.8	5	2.7
6	0.9	6	3.6	6	1.7
7	1.1	7	3.5	7	1.5
8	1.1	8	3.5	8	1.4
9	1.0	9	3.1	9	1.4

iv. Resistivity Data at 9.0 vol % Ambient Moisture

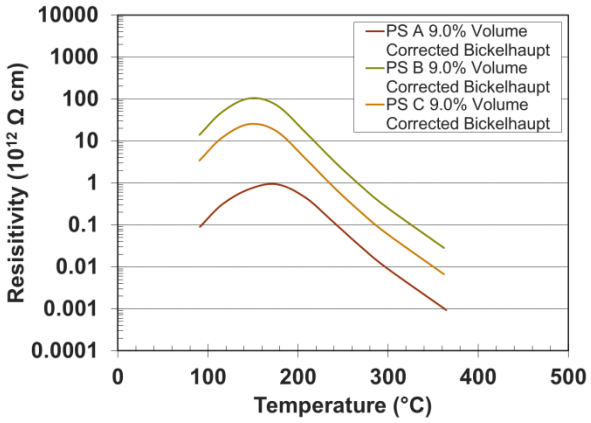


Figure J-16: Volume corrected Bickelhaupt model resistivity as a function of temperature for PS A, B & C at 9.0 vol% ambient moisture

Table J-20: Volume corrected Bickelhaupt resistivity data at 9.0 vol% ambient moisture

PS A		PS B		PS C	
Temperature (°C)	**Resistivity (Ω cm)**	**Temperature (°C)**	**Resistivity (Ω cm)**	**Temperature (°C)**	**Resistivity (Ω cm)**
91	9.0E+10	90.5	1.4E+13	90.5	3.4E+12
116	3.1E+11	116	5.0E+13	116	1.2E+13
146	7.2E+11	146	1.0E+14	146	2.5E+13
176.5	9.3E+11	176	7.2E+13	176	1.7E+13
208	4.5E+11	208	1.6E+13	208	3.9E+12
238	1.2E+11	238.5	3.5E+12	238.5	8.4E+11
268.5	3.2E+10	268	9.2E+11	268	2.2E+11
297.5	9.8E+09	297.5	2.7E+11	297.5	6.4E+10
364.5	9.4E+08	362	2.8E+10	362	6.7E+09

Table J-21: Resistivity error ratio for volume corrected Bickelhaupt model at 9.0 vol% ambient moisture

PS A		PS B		PS C	
Measurement	**Error Ratio**	**Measurement**	**Error Ratio**	**Measurement**	**Error Ratio**
1	5.9	1	7.5	1	14.3
2	5.8	2	8.5	2	12.3
3	3.0	3	7.7	3	8.6
4	1.1	4	8.8	4	6.3
5	1.2	5	5.7	5	2.8
6	1.1	6	4.7	6	1.8
7	1.1	7	4.3	7	1.4
8	1.3	8	4.0	8	1.2
9	1.1	9	3.4	9	1.2

d. Surface and Volume Corrected Bickelhaupt Model

In this section the results of the surface and volume corrected Bickelhaupt model are presented and includes the resistivity as a function of temperature and the determined resistivity data for 4.6, 6.0 and 9.0 vol% ambient moisture. This section also includes the deviations between the corrected Bickelhaupt model and the experimentally determined resistivity.

i. Resistivity Data at 4.6 vol % Ambient Moisture

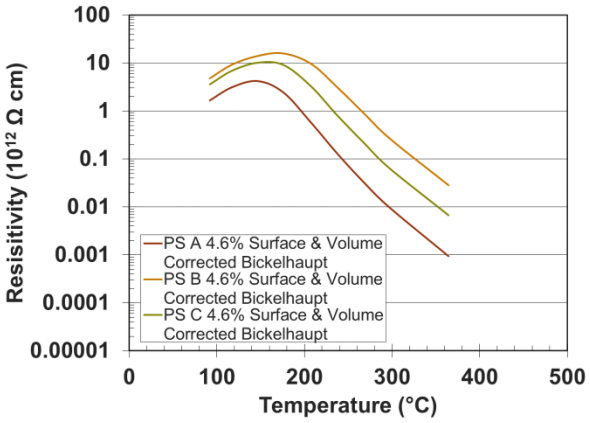


Figure J-17: Surface and volume corrected Bickelhaupt model resistivity as a function of temperature for PS A, B & C at 4.6 vol% ambient moisture

Table J-22: Surface and volume corrected Bickelhaupt resistivity data at 4.6 vol% ambient moisture

PS A		PS B		PS C	
Temperature (°C)	**Resistivity (Ω cm)**	**Temperature (°C)**	**Resistivity (Ω cm)**	**Temperature (°C)**	**Resistivity (Ω cm)**
92	1.7E+12	92	4.8E+12	92	3.6E+12
117	3.1E+12	117	9.2E+12	117	6.9E+12
146.5	4.2E+12	146.5	1.4E+13	146.5	1.0E+13
176	2.4E+12	176	1.6E+13	176	9.1E+12
207.5	5.7E+11	207.5	9.7E+12	207.5	3.3E+12
237.5	1.3E+11	237.5	3.1E+12	237.5	8.1E+11
268	3.2E+10	268	8.9E+11	268	2.2E+11
297	9.8E+09	297	2.7E+11	297	6.4E+10
364.5	9.4E+08	364.5	2.8E+10	364.5	6.7E+09

Table J-23: Resistivity error ratio for surface and volume corrected Bickelhaupt model at 4.6 vol% ambient moisture

PS A		PS B		PS C	
Measurement	**Error Ratio**	**Measurement**	**Error Ratio**	**Measurement**	**Error Ratio**
1	2.8	1	5.4	1	1.1
2	1.8	2	3.8	2	1.2
3	1.1	3	2.1	3	1.5
4	1.6	4	1.1	4	2.2
5	1.2	5	2.3	5	2.0
6	1.0	6	3.0	6	1.5
7	1.2	7	3.5	7	1.4
8	1.3	8	3.4	8	1.2
9	1.2	9	3.4	9	1.3

ii. Resistivity Data at 6.0 vol % Ambient Moisture

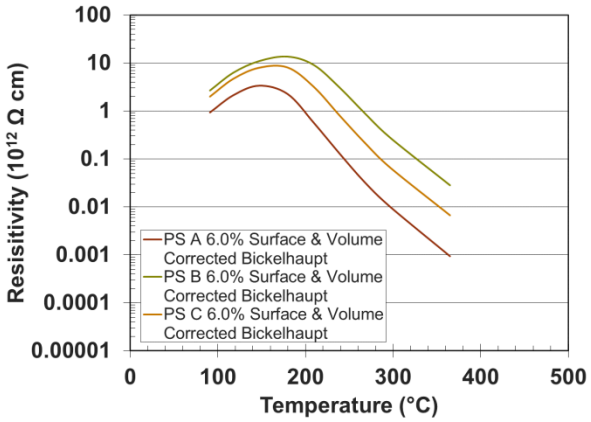


Figure J-18: Surface and volume corrected Bickelhaupt model resistivity as a function of temperature for PS A, B & C at 6.0 vol% ambient moisture

Table J-24: Surface and volume corrected Bickelhaupt resistivity data at 6.0 vol% ambient moisture

PS A		PS B		PS C	
Temperature (°C)	**Resistivity (Ω cm)**	**Temperature (°C)**	**Resistivity (Ω cm)**	**Temperature (°C)**	**Resistivity (Ω cm)**
91	9.3E+11	91	2.7E+12	91	2.0E+12
117.5	2.1E+12	117.5	6.3E+12	117.5	4.7E+12
147	3.4E+12	147	1.1E+13	147	8.0E+12
179.5	2.3E+12	179.5	1.4E+13	179.5	8.1E+12
209.5	5.7E+11	209.5	9.1E+12	209.5	3.2E+12
239	1.3E+11	239	3.1E+12	239	8.0E+11
268	3.2E+10	268	8.9E+11	268	2.2E+11
297.5	9.8E+09	297.5	2.7E+11	297.5	6.4E+10
365	9.4E+08	365	2.8E+10	365	6.7E+09

Table J-25: Resistivity error ratio for surface and volume corrected Bickelhaupt model at 6.0 vol% ambient moisture

PS A		PS B		PS C	
Measurement	**Error Ratio**	**Measurement**	**Error Ratio**	**Measurement**	**Error Ratio**
1	3.0	1	5.1	1	1.3
2	1.9	2	3.5	2	1.5
3	1.0	3	2.3	3	1.6
4	1.7	4	1.2	4	2.3
5	1.4	5	2.7	5	2.2
6	1.1	6	3.1	6	1.7
7	1.1	7	3.4	7	1.5
8	1.1	8	3.4	8	1.3
9	1.0	9	3.1	9	1.4

iii. Resistivity Data at 9.0 vol % Ambient Moisture

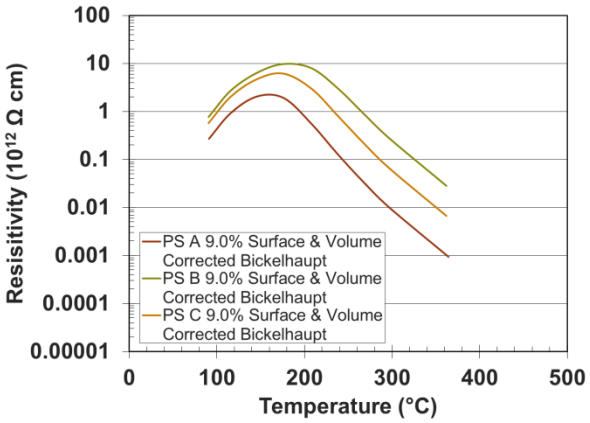


Figure J-19: Surface and volume corrected Bickelhaupt model resistivity as a function of temperature for PS A, B & C at 9.0 vol% ambient moisture

Table J-26: Surface and volume corrected Bickelhaupt resistivity data at 9.0 vol% ambient moisture

PS A		PS B		PS C	
Temperature (°C)	**Resistivity (Ω cm)**	**Temperature (°C)**	**Resistivity (Ω cm)**	**Temperature (°C)**	**Resistivity (Ω cm)**
91	2.7E+11	90.5	7.7E+11	90.5	5.7E+11
116	9.3E+11	116	2.7E+12	116	2.0E+12
146	2.1E+12	146	6.4E+12	146	4.7E+12
176.5	1.9E+12	176	9.7E+12	176	6.1E+12
208	5.5E+11	208	8.0E+12	208	3.0E+12
238	1.3E+11	238.5	3.0E+12	238.5	8.0E+11
268.5	3.2E+10	268	8.8E+11	268	2.1E+11
297.5	9.8E+09	297.5	2.7E+11	297.5	6.4E+10
364.5	9.4E+08	362	2.8E+10	362	6.7E+09

Table J-27: Resistivity error ratio for surface and volume corrected Bickelhaupt model at 9.0 vol% ambient moisture

PS A		PS B		PS C	
Measurement	**Error Ratio**	**Measurement**	**Error Ratio**	**Measurement**	**Error Ratio**
1	2.0	1	2.4	1	2.4
2	1.9	2	2.1	2	2.1
3	1.0	3	2.1	3	1.6
4	1.8	4	1.2	4	2.2
5	1.5	5	2.8	5	2.2
6	1.1	6	4.0	6	1.7
7	1.1	7	4.1	7	1.4
8	1.3	8	3.9	8	1.2
9	1.1	9	3.4	9	1.2

Dedicated to H, who means the world to me.